REVIEW

Check for updates

Transition metal sulfides meet electrospinning: versatile synthesis, distinct properties and prospective applications

Wendong Zhu,[a] Ya Cheng,[a] Ce Wang, [ID][a] Nicola Pinna [ID] *[b] and Xiaofeng Lu [ID] *[a]

One-dimensional (1D) electrospun nanomaterials have attracted significant attention due to their unique structures and outstanding chemical and physical properties such as large specific surface area, distinct electronic and mass transport, and mechanical flexibility. Over the past years, the integration of metal sulfides with electrospun nanomaterials has emerged as an exciting research topic owing to the synergistic effects between the two components, leading to novel and interesting properties in energy, optics and catalysis research fields for example. In this review, we focus on the recent development of the preparation of electrospun nanomaterials integrated with functional metal sulfides with distinct nanostructures. These functional materials have been prepared *via* two efficient strategies, namely direct electrospinning and post-synthesis modification of electrospun nanomaterials. In this review, we systematically present the chemical and physical properties of the electrospun nanomaterials integrated with metal sulfides and their application in electronic and optoelectronic devices, sensing, catalysis, energy conversion and storage, thermal shielding, adsorption and separation, and biomedical technology. Additionally, challenges and further research opportunities in the preparation and application of these novel functional materials are also discussed.

1. Introduction

In recent decades, nanoscience and nanotechnology has become an innovative research field due to the underlying distinct physical and chemical properties of materials at the nanoscale.[1–3] A large variety of nanomaterials with different nanostructures including zero dimensional (0D), one dimensional (1D), two dimensional (2D) and three dimensional (3D) structures have been prepared in the last decades, which was driven by an increasing demand for materials for applications in the fields of optoelectronics, catalysis, energy, environment, and biomedicine.[4–22] Among the typical four types of nanostructure, 1D nanostructured materials exhibit fibrous or tubular morphology with a diameter varying from several nanometers to hundreds of nanometers, possessing a unique electron and mass transport property, which is beneficial for achieving an improved performance in electronic devices, and catalytic and electrochemical reactions.[23–27] Up to now, numerous strategies, such as hard and sacrificial templates, hydrothermal and solvothermal reactions, solution–liquid–solid pro-

cesses, chemical vapor deposition, self-assembly, and electrospinning techniques have been developed to prepare various types of 1D nanomaterial.[28–34] Among these approaches, electrospinning is probably the most facile and versatile way to produce fiber- or tube-like nanomaterials with tailored compositions and architectures.[35–45]

Electrospinning originated from Rayleigh's study of droplets' static electricity in 1882 and did not attract significant research interest in the following century.[46] From the beginning of the 21st century, electrospinning technology has captured extensive attention because of the rapid development of the nanoscience and nanotechnology. In recent years, electrospinning has become a hot research topic and its development has experienced four stages. At first, researchers focused on the fundamentals of electrospinning and the study of the spinnability of various polymers as well as the influences of environmental and technological parameters on the fiber morphology, diameter and physical properties. In a second stage, much work was devoted to synthesizing multicomponent nanofibers. Afterwards, a large range of applications of electrospun nanofibers such as in filtration, sensors, catalysis, energy, environmental science, optoelectronics and biomedicine were broadly studied. Finally, many researchers have striven to explore the possibility of the large-scale industrial production of electrospun fibers. Compared with traditional

[a] Alan G. MacDiarmid Institute, College of Chemistry, Jilin University, Changchun, 130012, P. R. China. E-mail: xflu@jlu.edu.cn
[b] Institut für Chemie and IRIS Adlershof, Humboldt-Universität zu Berlin, Brook-Taylor-Straße 2, 12489 Berlin, Germany. E-mail: nicola.pinna@hu-berlin.de

textile fibers, electrospun nanofibers/membranes show many unique features such as the possibility to control the diameter at the nanoscale, a large specific surface area and a high porosity, which are properties required by a large range of applications.[20] Furthermore, electrospun nanofibers can be easily hybridized with other functional materials through either the direct electrospinning of a composite precursor or the combination with post-treatment routes, largely expanding their applications.[47]

Transition metal sulfides have led strong interests in many researchers around the world due to their excellent electrical conductivity, thermal and mechanical stability as well as the outstanding redox capacity, which contribute to interesting applications in the fields of optoelectronic devices, catalysis, energy conversion and storage.[48–52] By combining electrospun nanofibers and metal sulfides, a large variety of innovative and distinctive nanostructures have been synthesized in the last decade. Especially, hybrid materials with unique interfaces such as core–shell, Janus and hierarchical nanostructures provide efficient electron transfer capability and abundant active sites for multifunctional applications.[53] The strong interactions between different components contribute to the electronic modulation and the reconstruction of the active sites, which are beneficial for improved performance in catalysis and energy devices. Owing to the unique architectures, electrospun nanofibers can also act as a support and provide structural stability to functional nanomaterials, exhibiting in some cases synergistic effects that lead to improved long-term stability of the hybrid material.[36–39]

Although a number of review articles focused on the preparation and application of electrospun nanofibers have been published, few reviews have accounted for a discussion of the integration of electrospun nanofibers with metal sulfides and addressed their structure–property relationships.[35–45] In this review, recent progress in the preparation of electrospun nanofiber–metal sulfide hybrids and their promising applications in the fields of electronic and optoelectronic devices, sensing, catalysis, energy conversion and storage, thermal shielding, adsorption and separation, and biomedical technology have been summarized (Table 1). Specifically, the influence of the composition, nanostructure, electronic structure, and interface modulation on the performance of the hybrids is highlighted. Furthermore, remaining challenges and future perspectives of the field are discussed. We hope that this review article may trigger new developments for the design of more efficient metal-sulfide-based electrospun nanofibers for a large variety of advanced applications.

2. Routes for the integration of metal sulfide with electrospun nanofibers

2.1 Direct fabrication of metal sulfide/electrospun nanofibers during electrospinning processes

Metal sulfide–electrospun nanofibers are usually prepared *via* a facile two-step procedure, including metal sulfide nano-

particle synthesis and direct electrospinning of metal sulfide/polymeric precursors in a suitable solvent. Through the modulation of the polymer–solvent system and the size or surface state of the metal sulfides, the morphology of the prepared electrospun metal sulfide–polymer nanofibers can be optimized. Additionally, closer interface contact between the metal sulfide and the inner surface and outer surface of electrospun fibers can be achieved through this method. Generally, a small size and low concentration of metal sulfides are necessary to ensure a stable colloidal suspension in a typical polymer–solvent system to realize a uniform dispersion. Then uniform metal sulfide–polymer nanofibers can be generated by tailoring the viscosity of the solution, electric field intensity, humidity and even temperature. For example, PVP/CuS hybrid nanofibers have been prepared *via* an electrospinning precursor consisting of PVP and a CuS aqueous suspension with a concentration of 1 wt% (Fig. 1a).[54] TEM images show that the CuS nanoparticles are uniformly distributed within the PVP nanofibers with a low density (Fig. 1b–d). Consistent with the X-ray diffraction (XRD) results, the average size of CuS nanoparticles is around 10 nm. The formed PVP/CuS nanofibrous membranes possess positive charges on their surface, enabling their deposition on the surface of the fluorinated substrate, which shows promising potential for thermal shielding (Fig. 1e). Similarly, PVP/Ag$_2$S hybrid nanofibers have also been prepared *via* a direct electrospinning strategy.[55] First, Ag$_2$S nanoparticles are prepared from the reaction between AgNO$_3$ and CS$_2$ in the presence of PVP (Fig. 1f). Then a direct electrospinning process is performed to prepare PVP/Ag$_2$S hybrid nanofibers (Fig. 1g–i). In this study, the density of the Ag$_2$S nanoparticles in the PVP matrix can be well controlled by tailoring the weight ratio of PVP and Ag$_2$S. This result demonstrates that Ag$_2$S nanoparticles with a high density can be uniformly dispersed in PVP nanofibers without obvious aggregation.

In addition to PVP–water and PVP–ethanol systems, several other polymer–solvent systems have also been utilized for direct electrospinning to produce metal sulfide–polymer hybrid nanofibers, such as polyacrylonitrile (PAN)–N,N-dimethylformamide (DMF), poly(vinyl acetate) (PVAc)–DMF, poly(methyl methacrylate) (PMMA)–THF/DMF and poly(ethylene oxide) (PEO)–chloroform/acetone.[56–59] Metal sulfides can be well dispersed in those systems to form a stable suspension for direct electrospinning to generate metal sulfide–polymer hybrid nanofibers. For example, a fine dispersion of CdS nanoparticles can be prepared in a PVAc–DMF system.[56] After the electrospinning process, CdS nanoparticles can be embedded in the PVAc nanofibers (Fig. 1g). More interestingly, the CdS nanoparticles are assembled into a one-dimensional nematic-like structure, which might result from the stretching under a high voltage during the electrospinning process (Fig. 1k). By embedding CdS quantum wires into a PEO nanofiber, an alignment of the quantum wires along the direction of the long axis of the PEO nanofibers is observed, which should also be ascribed to the stretching under a high voltage.[60] Recently, periodic features have been patterned on a single PMMA nanofiber *via* an electrospinning and electron-beam lithography

Table 1 Typical transition metal sulfides integrated with electrospun materials and their applications and representative references

Material	Application	Performance	Ref.
CuS/TiO$_2$ nanofibers	Optical property	Improved absorption in the UV and visible region compared with pure TiO$_2$ fibers	89
CdSe/ZnS QD–PCL nanofibers	Optical property	The FRET efficiency reaches up to 40% with the donor–acceptor weight ratio of 10 : 5	94
P3HT–PEO–CdS nanofibers	Optical property	With an increase of band intensity and a furthermore red-shift (0.03 eV) for P3HT-PEO after the addition of CdS	95
MoS$_2$/TiO$_2$ nanofibers	Optical property	Nonlinear absorption coefficient β: 23.68 cm GW^{-1} and the OL threshold: 22.3 mJ cm^{-2}	96
GO/Bi$_2$S$_3$–PVDF/TPU nanofibers	Photothermal property	The temperature reaches 81 °C after 300 s irradiation in the wavelength range of 400–2500 nm	98
Co$_x$Zn$_{1-x}$S nanowires	Electronic property	A 5.16% Co doping leads to almost 15 times electrical conductivity	99
CoS, ZnS, CdS/PAN nanofibers	Electronic property	Improved current density and electrical conductivity compared with PAN nanofibers	100
PEDOT:PSS–PbS-NPs–PVP nanofibers	Electronic property	Enhanced electrical conductivity compared with PEDOT:PSS-PVP nanofibers	101
PNG based on PVDF–MoS$_2$ composite nanofibers	Piezoelectric property	Mechanical impact sensitivity of 0.5 and 0.16 V Pa^{-1} with detection pressures of 0.61 and 6.3 Pa	103
ZnS/PVA nanofibers	Piezoelectric property	The sensitivity of 2 V Pa^{-1} to acoustic random vibrations	105
CdS/TiO$_2$ nanofibers	Photoelectrochemical property	Photoconversion of 3.2% at 0.0 V (vs. Ag/AgCl)	106
CdS QD-decorated BaSnO$_3$/CdS nanofibers	Photoelectrochemical property	Maximum photocurrent density of around 4.8 mA cm^{-2} at 0 V versus SCE	107
PMMA–WS$_2$ INT composite nanofibers	Mechanical property	7-Fold and 18-fold increased dynamic mechanical properties compared with PMMA nanofibers	112
CdSe/ZnS QDs–PS hybrid nanofibers	Diode	Luminous flux and luminous efficiency increases by 51.8% and 42.9% at 800 mA	113
WS$_2$ crossed PEDOT–PSS nanoribbons	Diode	A turn-on voltage of 1.4 V and a rectification ratio of 12	117
CuS fibers network	Transparent conducting electrode	Resistance of around 20 Ω sq^{-1} and transmittance up to 80%	119
CdSe/CdS@SiO$_2$ nanorods	Electroswitchable polarized emission device	Polarization ratio of 0.45 at the area of 1.5 cm^2	122
ZnO NWA/PbS QDs film	Photodetector	Rise time of 9 s and decay time of 2 s as well as outstanding flexibility and mechanical stability	125
SmFeO$_3$@MoS$_2$ nanofibers	Humidity sensing	Response and recovery time for 1.5 s and 29.8 s	127
WS$_2$@MTCNFs	Gas sensing	Response of 28% at 4 ppm for NO$_2$ at room temperature	129
PS/QD hybrid nanofibers	Optical sensing	Sensitivity of 1% RH for humidity sensor and response of less than 90 ms for optical sensor	135
Ag/CdSe–CdS/PMMA texture	Optical sensing	Detection limit of 100 ppm with a response time lower than 1 min	136
WS$_2$/CNFs	Electrochemical sensing	Sensitivity of 5.36 μA μM^{-1} cm^{-2} and low detection limit of 0.01 μM for the detection of DA	142
NiCo$_2$S$_4$/EGF	Electrochemical sensing	Sensitivity of 7431.96 μA mM^{-1} cm^{-2} and a low detection limit of 0.167 mM	143
CoS nanoparticles in PAN electrospun nanofibers	Heterogeneous chemical catalysis	Degradation of MB and MR by 15 min and 60 min	59
NiS@CNFs	Heterogeneous chemical catalysis	3.11 mol H$_2$ mol^{-1} ammonia borane for 200 min	150
CuS/PAN nanofibers	Heterogeneous chemical catalysis	94.5% MB is degraded in 40 min	151
Cd$_{1-x}$Zn$_x$S/TiO$_2$ nanofibers	Photocatalysis	Photodegradation efficiency of RhB reaches 91.0% in 60 min	204
TiO$_2$/CdS nanofibers	Photocatalysis	Photocatalytic degradation efficiencies is 96.7% under UV light for 30 min	88
UCNPs/PVP/TBT/CdS nanofibers	Photocatalysis	92.5% of RhB degrades in 25 min	213
Pt-Decorated CdS/TiO$_2$ nanorods	Photocatalysis	H$_2$ production rate of 1063 μm h^{-1} g^{-1}	217
TiO$_2$/NiS nanofibers	Photocatalysis	H$_2$ production rate of 655 μmol h^{-1} g^{-1}	218
TiO$_2$/MoS$_2$ nanofibers	Enzyme-like catalysis	Linear concentration range of 0.05–1 μM with a detection limit of 0.05 μM	229
TiO$_2$@MoS$_2$/CoFe$_2$O$_4$ nanofibers	Enzyme-like catalysis	Linear concentration range of 0–1.0 μM with a detection limit of 0.13 μM	230
CuFe$_2$O$_4$@Cu$_9$S$_8$/PPy nanofibers	Enzyme-like catalysis	Linear concentration range of 2–20 μM with a detection limit of 1.0 μM	233
CNF@CoS$_2$ nanofibers	Water splitting	HER: onset potential of −40 mV and a Tafel slope of 66.8 mV per decade	259
MoS$_x$@NCNFs	Water splitting	HER: 137 mV at 10 mA cm^{-2} and a Tafel slope of 41 mV per decade	260
Co$_9$S$_8$/HWS$_2$/CNFs	Water splitting	HER: 78 mV at 10 mA cm^{-2}	261

Table 1 (Contd.)

Material	Application	Performance	Ref.
Phosphorus-doped $NiCo_2S_4$@CNT/CNF hybrid nanofibers	Water splitting	OER: 290 mV at 10 mA cm^{-2} HER: onset overpotential of 27 mV	262
Co_9S_8/CNFs	Solar cell	PCE of 8.37%	270
Co_3S_4/CNFs	Solar cell	PCE of 9.23%	271
$NiCo_2S_4$ nanorods/CNFs	Solar cell	PCE of 9.47%	275
(CdS:CdSe) quantum dot-sensitized TiO_2 nanofibers	Solar cell	Open-circuit voltage (0.64 V) with 2.69% efficiency	276
Sb_2S_3-Modified TiO_2 nanofibrous networks	Solar cell	PCE of 2.32%	284
Porous carbon nanofiber@MoS_2 core/sheath fibers	LIBs	Specific capacity: 954 mA h g^{-1}, rate capability: 475 mA h g^{-1} at 1 A g^{-1}	307
AGC-CoS_2@NCNFs	SIBs	Specific capacity: 876 mA h g^{-1} at 100 mA g^{-1}	321
In_2S_3/C nanofibers	LIBs and SIBs	Specific capacity of 696.4 mA h g^{-1} at 50 mA g^{-1} for LIBs and 393.7 mA h g^{-1} at 50 mA g^{-1} SIBs	346
Fe_7S_8@S/N–C	SIBs	Specific capacity: 220 mA h g^{-1} at 5 A g^{-1}	347
CNF@WS_2@Co_9S_8 nanofibers	LSBs	Capacity of 1175 mA h g^{-1} at 0.1C	348
S@Ni-NCFs	SSBs	Capacity of 738.7 mA h g^{-1} at 0.2C	352
Co_9S_8@G/NS-PCNFs	Li–O_2 and Al–air batteries	Discharge capacity of 8269 mA h g^{-1} at 100 mA g^{-1} Al–air battery: specific capacity of 2812 mA h g^{-1} at 35 mA cm^{-2}	353
$CuCo_2S_4$ nanosheets@NCNFs	ZABs	Specific capacity: 896 mA h g^{-1}	356
FeS_2–CoS_2/NCFs	Flexible ZABs	Specific capacity: 511 mA h g$^{-1}_{Zn}$ Peak power density: 69 mW cm^{-2}	358
CoS_x/C hybrid nanofibers	Supercapacitor	Specific capacitance: 496.8 F g^{-1} at 0.5 A g^{-1}	365
CNFs/$NiCo_2S_4$@PPy nanofibers	Supercapacitor	Specific capacitance: 2961 F g^{-1} at 1 A g^{-1}	374
Ni/Ni_3S_2/CNFs	Supercapacitor	Specific capacitance: 830.0 F g^{-1} at 0.2 A g^{-1}	382
CuS/PVP hybrid nanofibers	Thermal shielding	Transmittance of 68.8% at 550 nm and a low haze factor of 1.89%	54
CNFs@MoS_2 nanofibers	Adsorption	Overall removal capacity for Hg^{2+}: 6258.7 mg g^{-1}	385
MoS_2@PANI/PAN hybrid nanofibers	Adsorption	Adsorption capacity for $Cr(VI)$: 6.57 mmol g^{-1}	389
MoS_2/PAN hybrid nanofibers	Adsorption	Adsorption capacity for RhB: 77.7 mg g^{-1}	390
Poly(lactic acid) (PLA)/WS_2–MoS_2 hybrid nanofibrous membrane	Separation	A separation efficiency of 94.68% is achieved for the surfactant-stabilized oil/water emulsion	391
Fluorescent zein/CdS hybrid nanofibers	Biomedical application	For migration and proliferation of fibroblasts (L929) and stem cells (KUSA-A1)	395
MoS_2–PAN nanofibers	Biomedical application	Promote the growth of bone marrow mesenchymal stem cells (BMSC). Osteogenic differentiation of the BMSCs is improved with the increasing of MoS_2 content	397
Cu_2S–PLA/PCL nanofibrous membrane	Biomedical application	Promotion of adhesion, proliferation, angiogenesis of endothelium, and accelerating *in vivo* wound healing performance compared with PLA/PCL nanofibrous membrane	398

strategy, enabling a potential utilization of nanostructured light-emitting devices (Fig. 1l).[61] This strategy provides a nano-processing technique for a single nanosystem, extending the applications to future electrical nanodevices.

## 2.2 Indirect preparation of metal sulfide–electrospun nanofibers *via* post-treatment processes

As just mentioned, metal sulfide–polymer hybrid nanofibers can be prepared *via* a direct electrospinning strategy. However, metal sulfide nanoparticles are usually difficult to disperse in the electrospinning precursor or easily aggregated in the polymer nanofibers when their concentrations are large enough. To avoid the aggregation of small-sized metal sulfide nanoparticles in the electrospun polymer nanofibers, several strategies have been developed.[62–67] For example, our group has firstly demonstrated a simple gas–solid reaction to incorporate metal sulfides into polymer nanofibers.[62,63] In a typical fabrication of PbS/PVP nanofibers, the detailed procedure mainly involves three steps (Fig. 2a).[62] First, a metal salt of lead acetate is dissolved in ethanol/water solvent with a suitable concentration of PVP. Then the precursors are electrospun

to produce a PVP/lead acetate hybrid nanofibrous membrane. Finally, the membrane is treated under a H_2S atmosphere to prepare PVP/PbS hybrid nanofibers. After the vulcanization process, a yellow-colored membrane is observed. For a typical gas–solid reaction, the compact polymer networks can prevent further growth of metal sulfide particles after nucleation, leading to small particle sizes. Furthermore, the polymer networks reduce the aggregation of the prepared metal sulfide nanoparticles, resulting in their uniform distribution in the polymer nanofibers. As a result, small PbS nanoparticles with a spherical shape and size of around 5 nm are uniformly distributed within the PVP nanofibers (Fig. 2b and c). The gas–solid reaction provides an efficient and versatile route to prepare uniform and small-sized metal sulfide nanoparticles in electrospun nanofibers.[68–71]

Through a gas–solid reaction on the electrospun polymer–metal salt hybrid nanofibers, the obtained metal sulfide nanoparticles are mainly distributed within the polymer nanofibers. To achieve the formation of metal sulfide nanoparticles on the surface of polymer nanofibers, a facile approach is to decorate metal ions on the surface of electrospun nanofibers followed
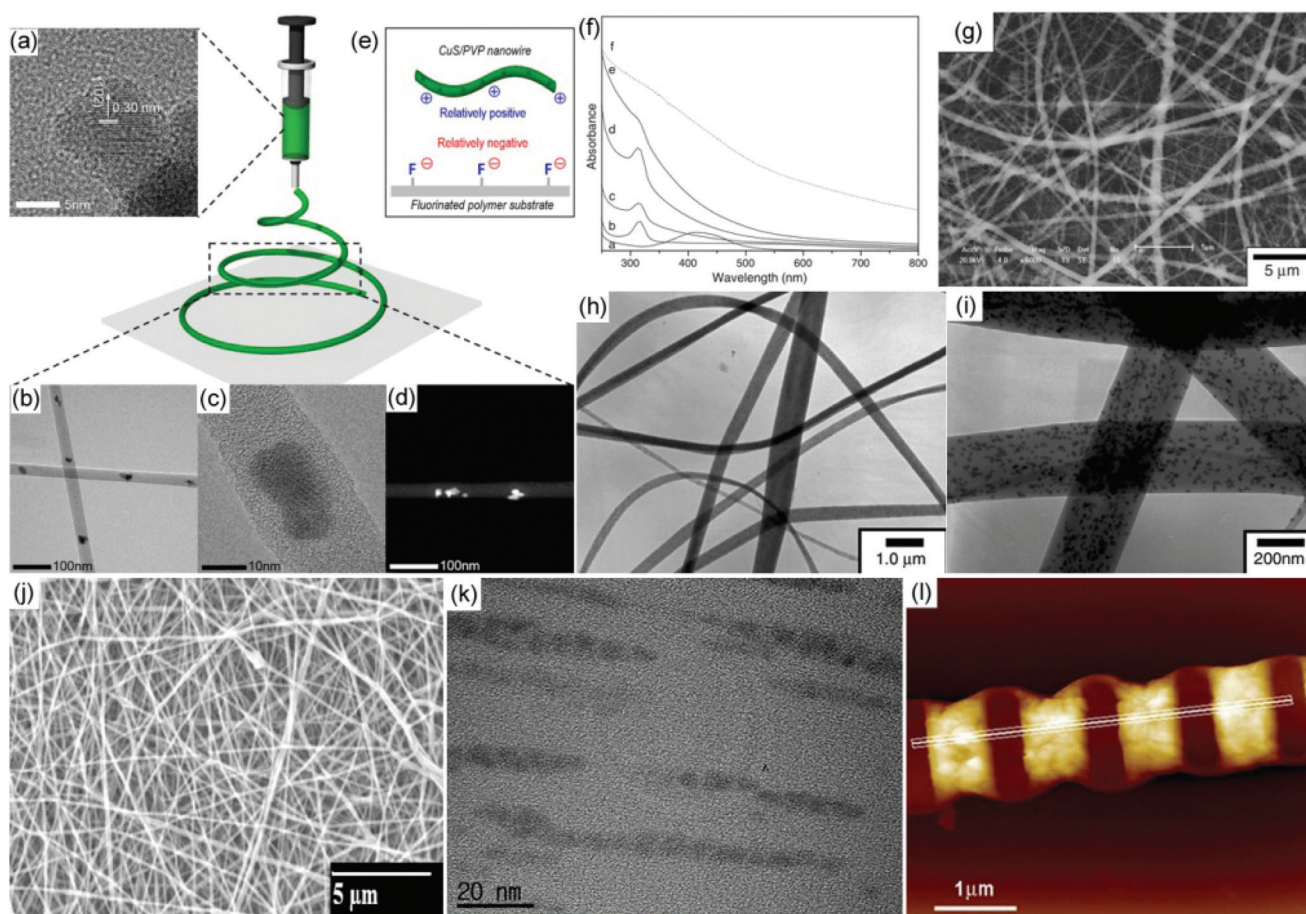
Fig. 1 (a) TEM image of individual CuS nanoparticles dispersed in aqueous solution. (b, c) TEM images of CuS/PVP nanofibers with a low and high resolution. (d) Scanning TEM image of a CuS/PVP nanofiber. (e) Mechanism to deposit CuS/PVP on the surface of fluorinated polymer. Reproduced with permission.[54] Copyright 2019, American Chemical Society. (f) UV–vis spectra of the formation of Ag_2S nanoparticles in a PVP/ethanol system. (g) SEM image of Ag_2S/PVP nanofibers. (h, i) TEM images of Ag_2S/PVP nanofibers with a low and high resolution. Reproduced with permission.[55] Copyright 2005, IOP publishing. (j, k) SEM and TEM images of CdS-doped PVAc hybrid electrospun nanofibers. Reproduced with permission.[56] Copyright 2012, Elsevier. (l) AFM topographic image of a CdS/PMMA hybrid nanofiber patterned by an electron-beam lithography strategy. Reproduced with permission.[61] Copyright 2012, John Wiley and Sons.

by a post-treatment process.[72,73] The strong interaction between the metal ions and the functional groups of the modified electrospun fibers leads to the growth of small-sized metal sulfide nanoparticles on the surface of the electrospun nanofibers. For example, our group has prepared sulfonic group-functionalized polystyrene (PS) nanofibers, which can adsorb Cd^{2+} on their surface.[72] After exposure to H_2S, CdS nanoparticles are uniformly formed on the surface of PS nanofibers. In addition to the gas–solid process, a wet chemical reaction was also developed to prepare metal sulfide–polymer hybrid nanofibers. Zhou and co-workers demonstrate the preparation of carboxylic PVA nanofibers to adsorb Zn^{2+}, which can be used to prepare ZnS nanoparticles by reaction with S^{2-}.[73] Owing to the strong interactions between PVA molecules and Zn^{2+}, the size of the obtained ZnS nanoparticles is only around 5 nm. Owing to the quantum effect of ZnS nanoparticles induced by the nanofibrous support, a blue shift of the photoluminescence of the hybrid nanofibers compared with bulk ZnS nanoparticles is observed.

Through a post-treatment process, metal sulfide nanoparticles can be hybridized with not only electrospun polymer nanofibers, but also carbon and ceramic nanofibers.[74–82] Recently, MnS@carbon nanofibers (CNFs) have been prepared via an electrospinning and subsequent carbonization process (Fig. 2d).[74] First, continuous $MnSO_4$/PAN nanofibers are prepared as a freestanding membrane by electrospinning. Then the as-spun membrane is heated in air at 280 °C and carbonized under a nitrogen atmosphere at 700 °C to produce MnS/CNFs. The SEM image shows a 3D network of interconnected MnS/CNF fibers with diameters of about 500 nm (Fig. 2e). The HRTEM image clearly demonstrates the high crystalline characteristic of the MnS nanocrystals with a size smaller than 10 nm, which are incorporated in the CNFs (Fig. 2f). Additionally, core–shell-structured MoS_2@Fe_xO_y@CNF nanofibers have been prepared via single-nozzle electrospinning and a subsequent carbonization process based on a phase separation of two precursors of PAN and PMMA.[75] It is observed that dense MoS_2 and iron oxide nanoparticles are encapsu-
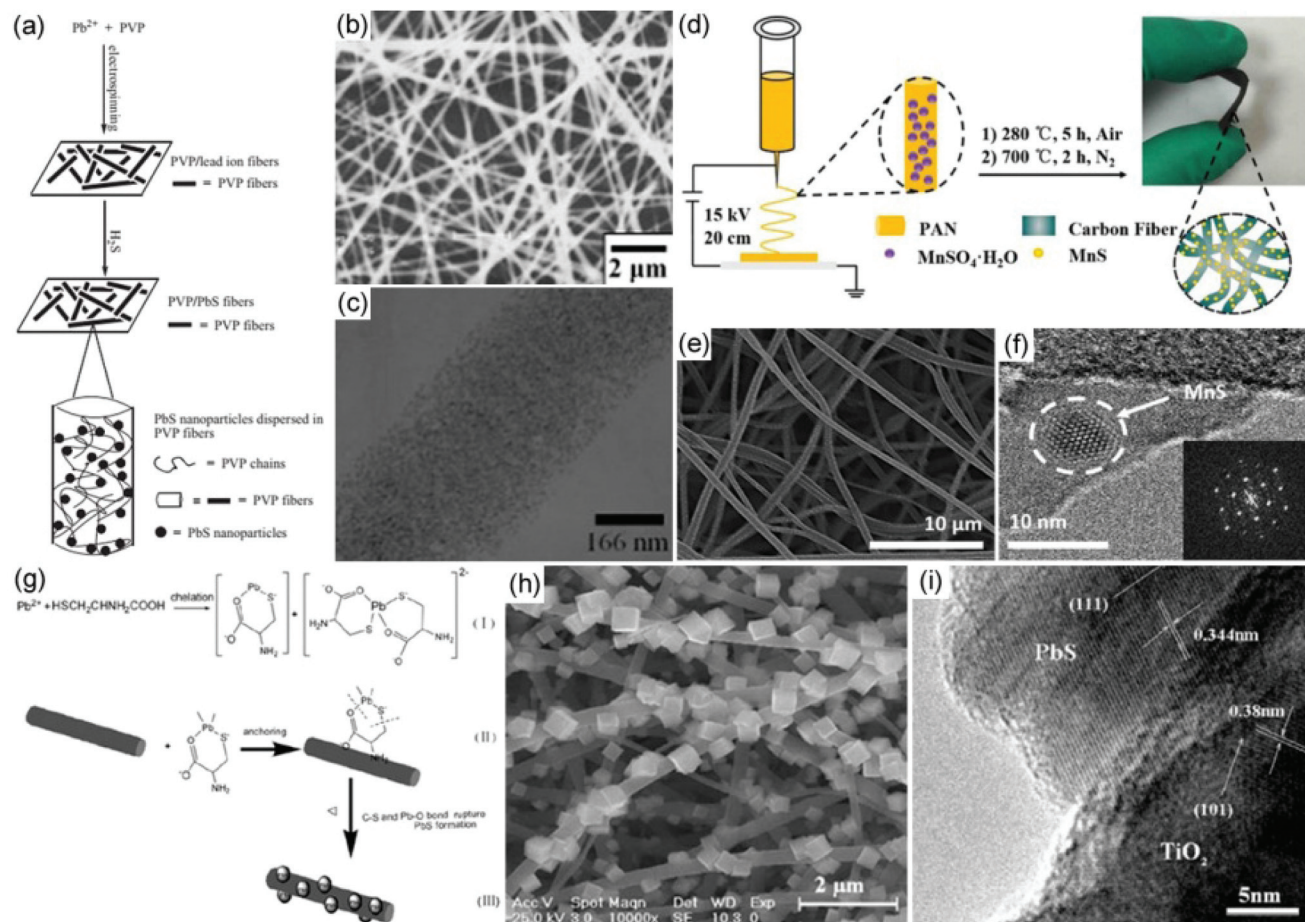
Fig. 2 (a) Schematic drawing of the preparation of PbS/PVP nanofibers from an electrospinning and gas–solid reaction. (b, c) SEM and TEM images of the obtained PbS/PVP nanofibers. Reproduced with permission.[62] Copyright 2005, John Wiley and Sons. (d) Schematic illustration of the preparation of MnS/CNFs. (e, f) SEM and TEM images of the prepared MnS/CNFs; the inset figure in f shows the SAED pattern of the MnS/CNFs. Reproduced with permission.[74] Copyright 2018, John Wiley and Sons. (g) Schematic drawing of the preparation of PbS/TiO$_2$ hybrid nanofibers. (h, i) SEM and TEM images of the obtained PbS/TiO$_2$ heterostructures. Reproduced with permission.[76] Copyright 2010, Elsevier.

lated in the porous outer wall of the CNFs. The unique core–shell MoS$_2$@Fe$_x$O$_y$@CNF nanofibers make them good candidates for energy conversion applications.

Hydro(solvo)thermal reactions are also a versatile way to decorate metal sulfides on the surface of electrospun nanofibers. For example, Shao and co-workers prepared a TiO$_2$/PbS heterostructure with PbS single-cube nanocrystals erected on electrospun TiO$_2$ nanofibers via a hydro(solvo)thermal reaction (Fig. 2g).[76] SEM and HRTEM images show that the PbS nanocubes possess an edge length of around 150–300 nm, dominating a preferential crystal growth direction in the (111) faces (Fig. 2h and i). Recently, Qu and co-workers prepared NiCo$_2$S$_4$ embedded in CNFs (NiCo$_2$S$_4$/CNFs) via an electrospinning, calcination, and hydrothermal vulcanization process.[83] Through such a strategy, NiCo$_2$S$_4$ nanoparticles are uniformly encapsulated in CNFs and a unique 1D hybrid nanostructure is formed. This type of structure can not only effectively reduce the volume expansion of NiCo$_2$S$_4$ nanoparticles, but also provide an improvement of structural stability, promoting their promising applications in supercapacitors.

3. Distinct chemical and physical properties

The chemical and physical properties of metal sulfides are associated with their composition, size and nanostructure. For example, through the manipulation of the composition, CuS possesses a higher electrical conductivity (9.5×10^{-3} S cm^{-1}) than Cu$_2$S (8.3×10^{-4} S cm^{-1}).[84] The luminescence of CdS nanoparticles has also been reported to be strongly dependent on their sizes.[85] Furthermore, the correlation between the nanostructures of metal sulfides and their chemical and physical properties has been broadly investigated. In addition, metal sulfide polymorphs exhibit different properties. For instance, layered MoS$_2$ and WS$_2$ with 1T, 1T', and Td phases are usually metallic, while those with a 2H phase are semiconducting.[86] On the other hand, for the integration of electrospun nanofibers with metal sulfides, hierarchical 1D structures with a unique interface can be achieved, contributing to the improved chemical and physical

properties resulting from both the compositional and structural synergistic effects.

3.1 Optical properties

The optical absorption capability of metal sulfides plays a vital role in their photocatalytic and photoelectric performance, which is directly related to their bandgaps. As the electronegativity of sulfur is lower than that of oxygen, metal sulfides possess narrower bandgaps than the corresponding metal oxides. As such, most metal sulfides exhibit a wide light response within the solar energy spectrum.[87] For example, CdS has a bandgap of ~2.38 eV, and is regarded as a typical visible-light-responding semiconductor. Similarly, CuS is a p-type semiconductor with a narrow bandgap of around 2.2 eV. Because of an additional near-infrared absorption band, CuS is a good visible-light-responding material. Therefore, the modification of metal sulfides with narrow bandgaps onto electrospun semiconducting nanofibers can reduce the reflectivity in the visible light region, which enhances their absorption capability.[88–90] For example, the absorption band of CuS/TiO$_2$ nanofibers shows a significantly improved absorption in the wavelength 600–800 nm with a red shift of 100–105 nm of the absorption edge compared with bare TiO$_2$ nanofibers.[89] This optical characteristic of the metal sulfides is beneficial for the production of more photogenerated electrons and holes for light-to-chemical conversion applications.

Metal sulfide nanocrystals usually display a narrow emission band and large quantum yields, and their photoluminescence (PL) property is significantly correlated with their sizes and compositions.[91–93] More interestingly, the modification of the nanostructure through the spatial confinement of emitting semiconductor nanomaterials with donor and acceptor species in a 1D polymeric matrix enables the manipulation of excitonic interactions to achieve an efficient energy transfer. For example, green- and red-emitting CdSe/ZnS QDs embedded in electrospun polycaprolactone (PCL) nanofibers have been prepared.[94] Time-resolved PL spectroscopy reveals that the lifetime of donor-green-emitting QD decays gets shorter after the introduction of acceptor-red-emitting QDs into the nanofibers, which results from Förster type nonradiative energy transfer. The fluorescence resonance energy transfer (FRET) efficiency can reach 40% with a donor–acceptor weight ratio of 10 : 5. The luminescent CdSe/ZnS QDs/PCL nanofibrous platform shows a promising application for white light generation. The PL properties of the metal sulfides can also be significantly influenced by the passivation and electron transfer effect from the polymer matrix.[57,95] After the addition of PANI, an efficient electrons–holes separation can be obtained, contributing to the enhancement of the PL in the PEO/CdS nanofiber system.[95]

Recently, metal sulfides and their hybrids have been prepared as nonlinear optical (NLO) materials to show an excellent NLO response. For example, MoS$_2$/TiO$_2$ hybrid nanofibers have been prepared by electrospinning and subsequent hydrothermal reactions.[96] The material displays an increased reverse saturable absorption (RSA), demonstrating an optical limiting (OL) effect. The nonlinear absorption coefficient β is estimated to be around 23.68 cm GW^{-1}, which is much higher than that of bare TiO$_2$ nanofibers and pristine MoS$_2$ nanosheets under the same pump power. In addition, the OL threshold of the MoS$_2$/TiO$_2$ hybrid nanofibers is 22.3 mJ cm^{-2}, which is lower than that of pure TiO$_2$ nanofibers and individual MoS$_2$ nanosheets. This result demonstrates that an enhanced NLO property can be achieved through the hybridization of TiO$_2$ and MoS$_2$.

3.2 Photothermal properties

Over the past years, photothermal conversion materials have aroused more and more interest for their unique light-to-heat conversion capability, which has shown broad promising applications in photocatalysis and medical therapy.[97] Several traditional typical materials including metal, metal oxide, metal sulfide, carbon, and conducting polymers have been proved to be efficient photothermal conversion materials. Recently, GO/Bi$_2$S$_3$ NPs were prepared to be incorporated in PVDF/TPU composite nanofibers via an electrospinning route for photothermal conversion application.[98] It is found that the temperature of GO/Bi$_2$S$_3$-PVDF/TPU membrane reaches 81 °C after 300 s irradiation, which is much higher those of PVDF, TPU, PVDF/TPU, and GO-PVDF/TPU membranes. This result confirms that the better photothermal conversion performance could result from the outstanding solar harvesting capability of the Bi$_2$S$_3$ nanoparticles.

3.3 Electronic properties

Most metal sulfides are semiconducting materials, or in some cases, including Co$_9$S$_8$ and Ni$_3$S$_2$, they have been reported to be good metallic conductors, which makes them interesting materials as electrode materials for energy conversion and storage devices.[48] If required, to improve the conductivity of metal sulfides, doping with heteroatoms is an efficient strategy. For example, Co-doped ZnS nanowires have been demonstrated to possess an enhanced conductivity compared with bare ZnS nanowires.[99] With 5.16% Co doping, the conductivity is almost 15 times as high as that of ZnS material. The improved conductivity can be attributed to the excess free carriers from the doping state. Recently, metal sulfides have also been investigated to increase the conductivity of polymers. For instance, it has been reported that the incorporation of CdS nanoparticles in electrospun non-conducting polymer PAN nanofibers can significantly enhance the electrical conductivity of PAN, which is attributed to the charge transfer between PAN and CdS induced by an electric field.[100] In addition to non-conducting polymers, the conductivity of conducting polymers can also be significantly improved by the introduction of semiconducting metal sulfides. For example, core–shell nanofibers with poly(3,4-ethylenedioxythiophene)–poly(styrenesulfonate) (PEDOT:PSS)/PbS as core and PVP as shell were prepared via a coaxial electrospinning technique.[101] It was found that the conductivity of the PEDOT:PSS–PbS-NPs–PVP nanofibers is much higher than that of PEDOT:PSS–PVP

nanofibers, which might result from the increased hole and electron mobilities after the introduction of PbS nanoparticles. The enhancement of the conductivity of the PEDOT:PSS–PbS-NPs–PVP nanofibers can be related to the donor–acceptor mechanism between nanoparticle–polymer and the percolation conduction pathway between PbS NPs.

3.4 Piezoelectric properties

Piezoelectric energy harvesters are among the most popular energy conversion devices, which can be broadly applicable in wearable electronics.[102] Traditional piezoelectric materials include $PbTiO_3$, $BaTiO_3$, ZnO, and GaN, *etc*. Recently, metal sulfides nanomaterials such as MoS_2 and ZnS have also been demonstrated to possess piezoelectric properties.[103–105] In addition, the hybridization of metal sulfides with PVDFs can also enhance the piezoelectric performance of the polymer.

Ray, Mandal and co-workers demonstrated the incorporation of 2D MoS_2 into electrospun PVDF nanofibers by electrospinning.[103] The resulting hybrid nanofibers display a mechanical impact sensitivity of 0.5 and 0.16 V Pa^{-1} to detect pressures of 0.61 and 6.3 Pa, respectively (Fig. 3a and b). The improved crystallinity of the hybrid nanofibers by 2D MoS_2 and the β phase in PVDF nanofibers contribute to a highly efficient piezoelectric performance. Furthermore, the hybrid nanofibers exhibit an ultrafast capacitor charging capability, which enables energy storage in portable electronic devices. In addition to PVDF, the metal sulfides can also be hybridized with other electrospun nanofibers to construct a piezoelectric nanogenerator. For example, ZnS/PVA hybrid nanofibers with the incorporation of oriented ZnS nanorods have been prepared for piezoelectric applications.[105] A favorable acoustic sensitivity of 2 V Pa^{-1} has been achieved.
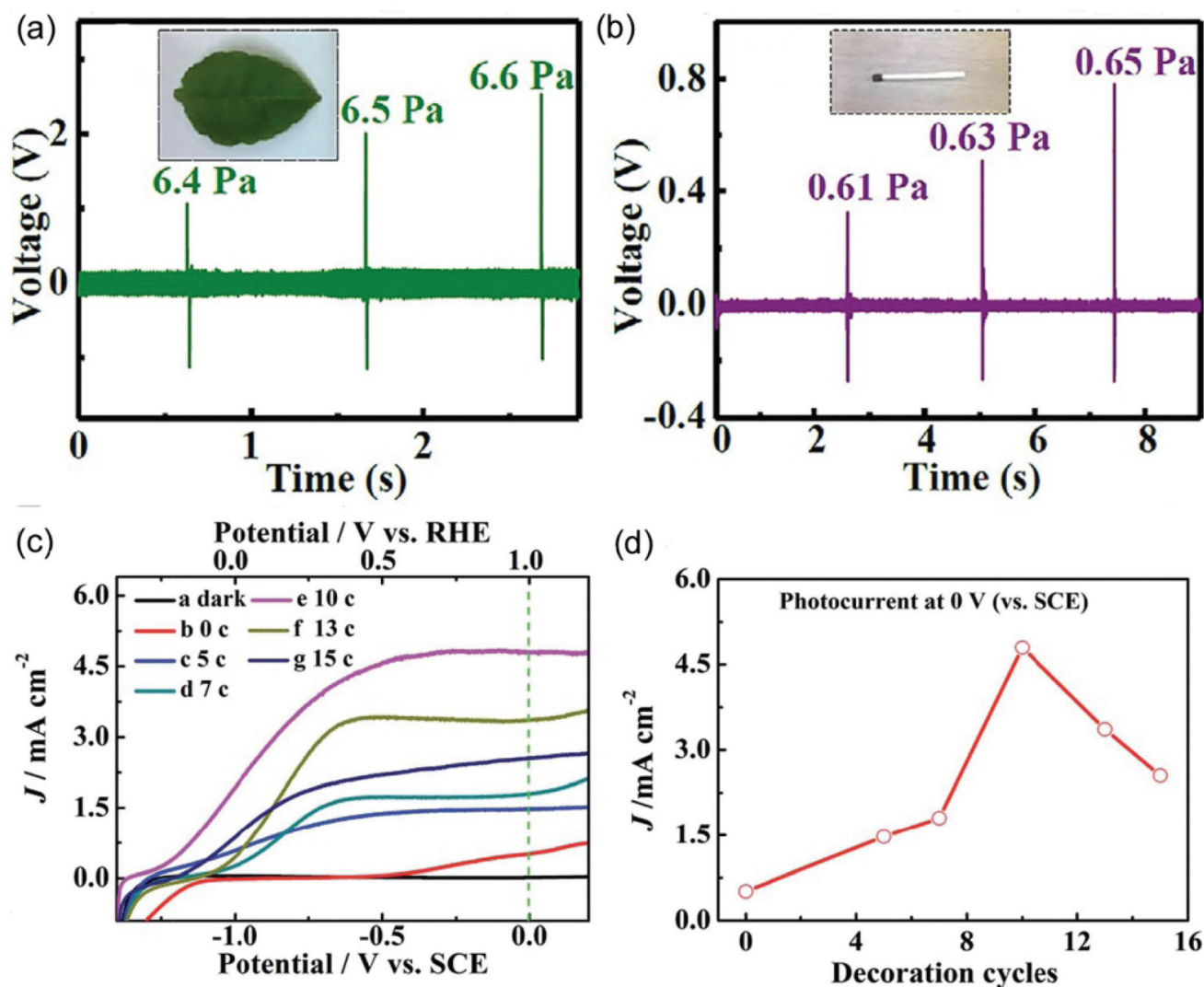

Fig. 3 Output voltage responses of a piezoelectric nanogenerator for different applied stresses from (a) a falling leaf to (b) a matchstick falling from different heights. Reproduced with permission.[103] Copyright 2017, John Wiley and Sons. (c) Linear-sweep voltammograms curves of $BaSnO_3$/CdS hybrid nanowires with varied decoration cycles. (d) The relationship between short-circuit photocurrent and decoration cycles. Reproduced with permission.[107] Copyright 2015, Royal Society of Chemistry.

3.5 Photoelectrochemical properties

Metal sulfide materials are one of the most efficient sensitizers for semiconducting materials to enhance the photoelectrochemical properties.[106–110] For example, a CdS layer has been successfully decorated on the surface of electrospun TiO_2 nanofibers via a dip-coating route.[106] The optimized hybrid nanofibers show a photoconversion efficiency of 3.2% at 0.0 V (vs. Ag/AgCl), which is over 20 times larger than bare TiO_2 nanofibers at the same voltage. The improved photoelectrochemical performance originates from the energy-band alignment at the interface contacts and the enhanced built-in potential, which reduces the photoelectron–hole recombination. Recently, CdS-modified electrospun $BaSnO_3$ nanowires have also been prepared via an ionic layer adsorption and reaction strategy to achieve an improved photoelectrochemical property.[107] It is very interesting that the photoelectrochemical performance is significantly dependent on the density of CdS nanoparticles (Fig. 3c). With 10 decoration cycles to deposit CdS nanoparticles, $BaSnO_3$/CdS hybrid nanowires exhibit a maximum photocurrent density of around 4.8 mA cm^{-2} at 0 V versus SCE, which is 9.6 times as high as that of bare $BaSnO_3$ nanowires (Fig. 3d).

3.6 Mechanical properties

Mechanical properties are very important for the practical applications of electrospun membranes. It is generally considered that 1D nanofillers uniformly distributed in polymers are beneficial for the enhancement of the mechanical properties of the composite.[111] Embedding tungsten disulfide (WS_2) nanotubes in an electrospun PMMA nanofiber will also improve the mechanical performance of the hybrid nanofibers.[112] The stress–strain curves show that bare PMMA nanofibers possess a tensile stress of 1.9 MPa, while the PMMA/WS_2 hybrid nanofibers with 1 wt% and 2 wt% WS_2 nanotubes reach 2.56 and 2.52 MPa, achieving 35% and 32% enhancement. Furthermore, the tensile modulus significantly increases from 10.16 MPa for individual PMMA nanofibers to 102.08 and 221.47 MPa for PMMA/WS_2 hybrid nanofibers with 1 wt% and 2 wt% WS_2 nanotubes. This result demonstrates that the addition of WS_2 nanotubes efficiently enhances the mechanical performance of the PMMA nanofibers due to the high rigidity of WS_2 nanotubes and active load transfer from PMMA nanofibers to WS_2 nanotubes. Dynamic mechanical properties of the prepared PMMA/WS_2 hybrid nanofibers have also been studied. Bare PMMA nanofibers show a storage modulus value of around 20 MPa, while the PMMA/WS_2 hybrid nanofibers with 1 wt% and 2 wt% WS_2 nanotubes exhibit 7-fold and 18-fold increases compared with PMMA nanofibers. The loss factor (tan δ) peak maximum reduces in a temperature interval of 4 °C after the introduction of 1% and 2% WS_2 nanotubes into PMMA nanofibers, which might result from the plasticizing effect caused by the exposed sulfur atoms.

4. Applications

4.1 Electronic and optoelectronic devices

4.1.1 Diodes. White light-emitting diodes (LEDs) have been regarded as the most suitable technology for next-generation solid-state light sources.[113,114] During the last two decades, QDs light-emitting devices (QLEDs) have captured significant attention because of their wide color range, high color-rendering index, and excellent solution-processing performance.[115] To reduce the non-radiative energy loss induced by the agglomeration of QDs, the preparation of QDs–polymer hybrid film is a promising strategy to generate high-performance QLEDs. However, the low thermal conductivities of polymers usually cause difficulty in heat dissipation, which leads to PL quenching. Therefore, it is necessary to increase the thermal conductivities of QD–polymers composites for LED applications. It has been reported that the alignment of polymer chains by electrospinning can achieve a 20-fold enhancement of thermal conductivity.[116] Recently, electrospun CdSe/ZnS QDs–PS hybrid nanofibers have been prepared and packaged on chip-on-board (CoB) LEDs.[113] In comparison with traditional QDs–PS membranes, the CdSe/ZnS QD–PS hybrid nanofiber membrane shows an enhancement of around 55.4% and 481.3% for the through-panel and in-panel thermal diffusivities, respectively. Then an increase of 51.8% and 42.9% is achieved for the luminous flux and luminous efficiency of the hybrid nanofiber-based LEDs when the driving current is 800 mA. Finally, the maximum temperature of the hybrid nanofibers is reduced by ~2% compared with the traditional QD–PS membrane.

A Schottky diode has also been constructed by a crossed WS_2/PEDOT–PSS device, in which the WS_2 flakes are synthesized via a chemical vapor deposition (CVD) method and PEDOT–PSS nanoribbons are prepared by electrospinning.[117] An electron transfer from the conduction band of WS_2 to the LUMO level of PEDOT results in band bending, which forms a potential barrier to restrict further current. From the current–voltage curve, a non-linear and asymmetric diode-like behavior is achieved, displaying a turn-on voltage of 1.4 V and a rectification ratio of 12. Furthermore, the prepared Schottky junction exhibits an ideality parameter of 1.9 and a barrier height of 0.58 eV, respectively.

4.1.2 Transparent conducting electrodes. It is well known that indium tin oxide (ITO) is the most commercially used transparent conducting electrode with broad applications in optoelectronic devices.[118] ITO usually shows the disadvantage of poor mechanical flexibility, restricting its potential usage in stretchable electronics. Thereby, a large number of highly conductive materials such as Ag and Cu nanowires, carbon nanotubes, and conducting polymers have been developed to replace the ITO material. Recently, metal sulfide nanomaterials have also been utilized as efficient conducting electrodes.[119] For example, CuS fiber networks have been deposited on various types of flexible substrates by electrospinning and metal sputtering as well as solvothermal reaction processes.[119] A CuS fiber network electrode shows a low resis-

tance of around 20 Ω sq^{-1} and a high transmittance of up to 80%. Furthermore, the electrode also represents the advantages of excellent mechanical and flexible properties as well as chemical stability, enabling its promising applications in flexible electronics and sensors as well as flat panel displays.

4.1.3 Electroswitchable polarized emission devices. Anisotropic structures generally display polarized emission along a parallel direction, which can be applicable for lighting or display devices.[120] To achieve aligned colloidal objects, electrospinning is an efficient and versatile route. For example, Au nanorods can be easily aligned along the electrospun polymeric nanofiber axis during the electrospinning process.[121] To get a polarized emission, CdSe/CdS@SiO$_2$ nanorods have been prepared and incorporated into electrospun PVP nanofibers.[122] A parallel plate collector has been utilized to collect the hybrid nanofibers, providing nanofibers oriented perpendicularly to the parallel stripes. The prepared flexible membrane with an area of 1.5 cm^2 composed of the hybrid nanofibers represents a polarization ratio of 0.45. Furthermore, an electroswitchable polarized emission device can be constructed via the inte-

gration of the aligned hybrid nanofibers in a liquid crystal cell. As shown in Fig. 4a, there is almost no light appearance with the polarizer oriented parallel to the nanofibers. On the other hand, strong polarized emission is observed with the polarizer rotated perpendicularly to the nanofibers and a polarization ratio of 0.45 is obtained (Fig. 4b). This state can be defined as the "on" position. In Fig. 4c, under an electric field of 50 V, the LC director is not perpendicular to the substrates, inducing a block of the polarization emission of the CdSe/CdS@SiO$_2$ nanorods by the polarizer. This state is defined as the "off" position. In this case, the polarization ratio is calculated to be 0.43. In a word, the integration of anisotropic metal sulfide nanostructures with electrospun nanofibers can achieve a polarized emission, which can be further constructed as an electroswitchable device with a tunable alignment of the nematic liquid crystal to get a switching over 90°.

4.1.4 Photodetectors. Photodetectors have captured significant interest in recent years because of their promising applications in imaging, sensing, and communication.[123] The spectral responses based on photodetectors can cover ultraviolet,
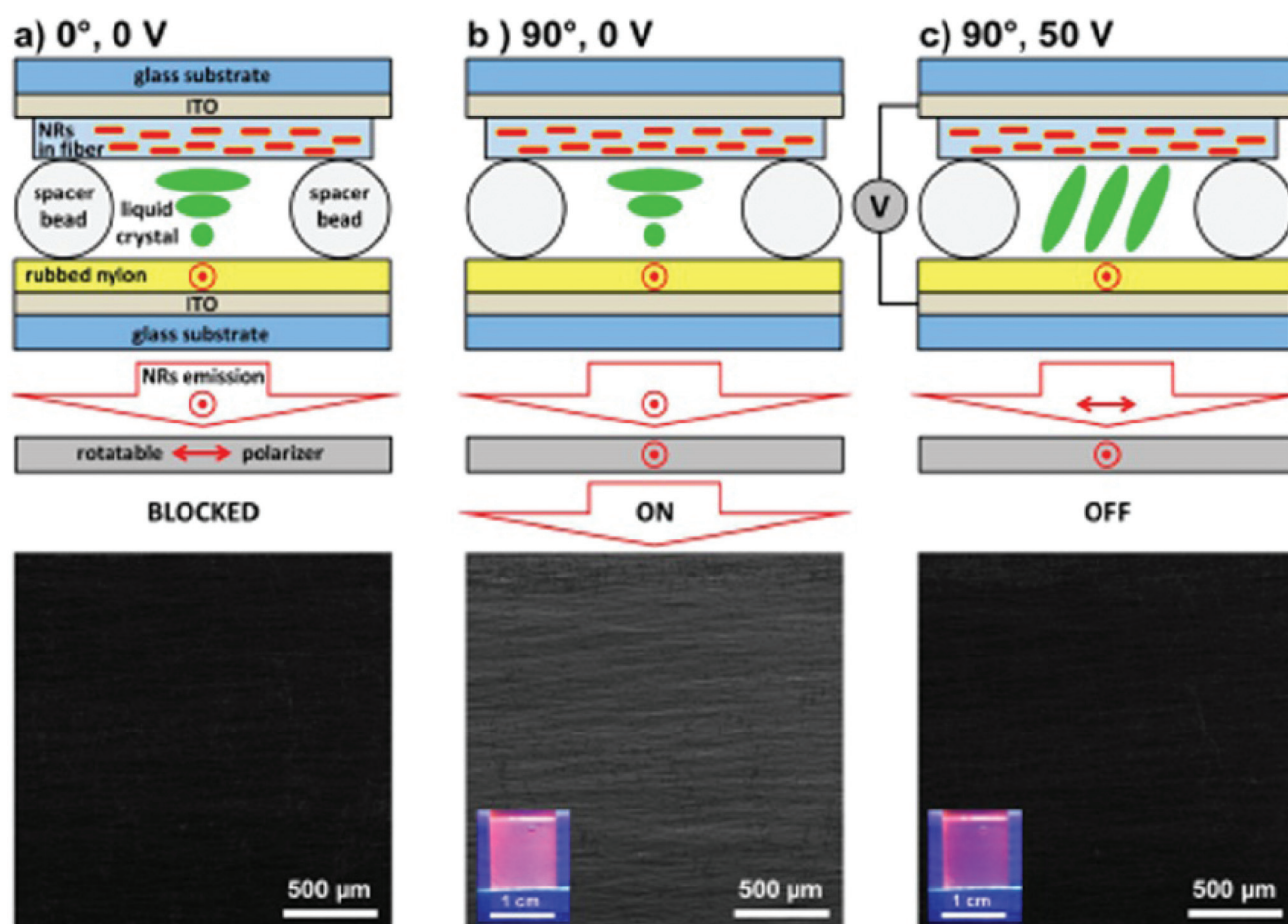
Fig. 4 CdSe/CdS@SiO$_2$@PVP nanofiber-based liquid crystal cell and corresponding fluorescence microscopy images under different conditions: (a) polarizer is parallel to the nanofibers (0°) without an electric field, (b) polarizer is rotated perpendicularly to the nanofibers (90°) without an electric field, (c) polarizer is maintained perpendicular to the nanofibers (90°) with a 50 V electric field. Reproduced with permission.[122] Copyright 2015, American Chemical Society.

visible and even near-infrared light. 1D nanomaterials are excellent candidates for photodetectors due to their distinct geometrical characteristics to provide direct pathways for charge transport.[124] ZnO nanowire array/PbS QD hybrids have been prepared by electropsinning, spin-coating and subsequent exchanging process.[125] It is found that the responsivity and detectivity of the ZnO/PbS-based photodetector is much better than the PbS thin film, but slightly inferior to bare ZnO nanowires in the UV range (Fig. 5a). However, a faster response and recovery speed of the ZnO/PbS-based photodetector with a rise time of 9 s and decay time of 2 s are achieved compared with those of ZnO nanowires with a rise time of 42 s and decay time of 22 s (Fig. 5b). In addition, the ZnO/PbS-based photodetector shows a wider response region in the visible and near-infrared regions compared with the bare ZnO nanowire-based photodetector, which is ascribed to the efficient electrons–holes separation capability from the

photoexcitation of PbS QDs and the electron transfer to the ZnO nanowires (Fig. 5c). Furthermore, the ZnO/PbS-based photodetector shows outstanding flexibility and mechanical stability, demonstrating an almost unchangeable photoresponse after 200 cycles of 180° bending (Fig. 5d–i). This study stimulates the development of flexible and high-performance next-generation photodetectors.

4.2 Sensing

4.2.1 Conductance sensing. Humidity sensing has been widely used to monitor the environmental conditions in our daily life. It has been reported that MoS_2 nanosheets have shown a certain humidity-sensing property, but the sensitivity still needs to be ehanced.[126] However, through the integration of electrospun $SmFeO_3$ nanofibers with MoS_2 nanosheets, an enhanced humidity-sensing performance has been obtained.[127] The results show that the response of the
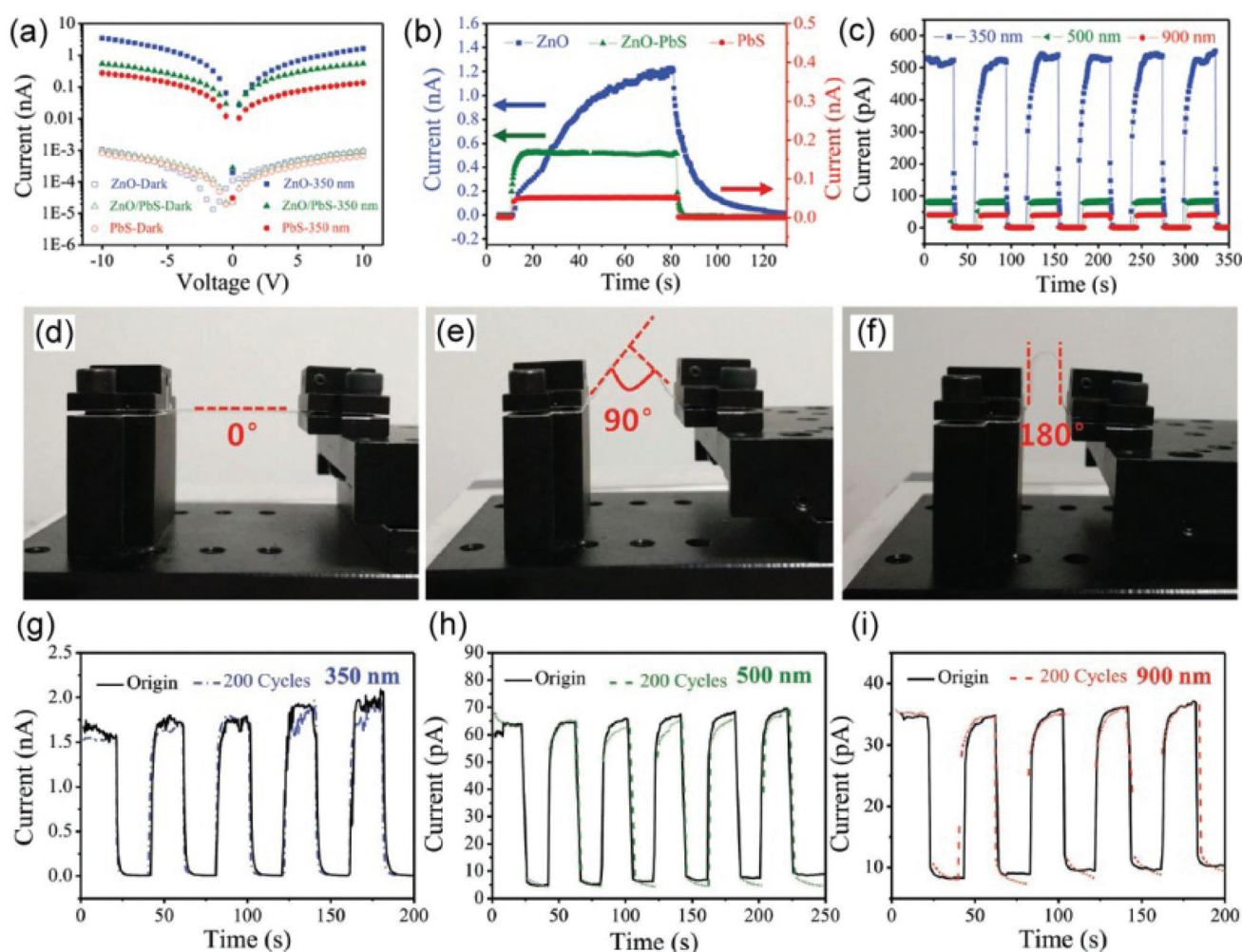
Fig. 5 (a) Current–voltage curves of three types of sample in the dark and with 350 nm illumination. (b) Current–time curve of varied types of device during on–off switching tests under 350 nm illumination with a bias of 10 V. (c) Current–time curve of varied types of device during on–off switching tests under different illumination. (d–f) Optical images of the flexible samples on mica substrate at various bending degrees. (g–i) Current–time curves between the original sample and the sample subjected to 200 bending cycles with a bending degree of 180° under different illumination. Reproduced with permission.[125] Copyright 2017, John Wiley and Sons.

$SmFeO_3@MoS_2$ hybrid-based sensor is much higher than that of sensors based on bare $SmFeO_3$ and MoS_2 materials, which is even 100 times as high as that of a MoS_2 humidity sensor. In addition, the hybrid nanofiber-based humidity sensor shows response and recovery times of only 1.5 s and 29.8 s, which is superior to the sensor based solely on $SmFeO_3$. The enhanced humidity sensing performance of the $SmFeO_3@MoS_2$ hybrid could result from the synergistic effect between the two components. Because of the p–n junctions characteristic of the $SmFeO_3@MoS_2$ heterostructure, a built-in electric field will produce a promotion of the electron and hole separation at the interface, leading to an increase of surface carriers to adsorb oxygen molecules. Thereby, more hydroxyl groups are formed on the $SmFeO_3@MoS_2$ hybrid resulting from the adsorption of water molecules. The resultant efficient protons transport leads to a decrease of the impedance.

During the last several decades, a large number of gas sensors based on electrospun nanofibers integrated with metal sulfides have been developed for the detection of alcohols, nitrogen oxides (NO_2 and NO), methane, and other volatile organic compounds.[128–134] For example, WS_2 edge-functionalized CNFs with multiple tubular pores ($WS_2@MTCNFs$) have been prepared via a copolymer-assisted electrospinning and annealing process.[129] Owing to the usage of sacrificial templates of poly(styrene-acrylonitrile), the $WS_2@MTCNFs$ show a much larger specific surface area of 41.4 m^2 g^{-1} compared with $WS_2@CNFs$ (6.4 m^2 g^{-1}). As the result of the improved surface area and open mesoporous structure to provide abundant channels and reactive surface species, the $WS_2@MTCNFs$ exhibit excellent gas-sensing performance for NO_2. The gas response was 28% at 4 ppm of NO_2 at room temperature, which is superior to $WS_2/CNFs$ and pristine CNFs. An outstanding selectivity for NO_2 based on this sensor is also observed over ammonia (NH_3) and toluene (C_7H_8) gases. Compared with pristine CNFs with a negligible response, $WS_2@MTCNF$ samples show a response of 1.8% with a low NO_2 concentration of 200 ppb. Furthermore, a limit of detection can be estimated to be 10 ppb for NO_2 with a response of 0.29%.

4.2.2 Optical sensing. Owing to the excellent surface-stimulated PL properties of QDs, a large variety of optical sensors have been developed based on PL improvement or quenching towards varied target molecules such as gases, anions, and cations.[135–140] On the other hand, 1D nanomaterials show the advantage of tight optical confinement, which provides optical sensing with a larger sensitivity and higher response speed. Tong and co-workers have demonstrated that CdSe/ZnS QD dopants can be incorporated into PS electrospun nanofibers as an optical sensor for humidity detection (Fig. 6a).[135] The PS–QD hybrid nanofibers show a diameter of several hundreds of nanometers with a density of about 3×10^3 μm^{-3} QDs (Fig. 6b–d). They show excellent PL properties and high photostability (Fig. 6e and f), and have been used in humidity sensors due to their relative humidity (RH)-dependent PL properties. The sensing mechanism is related to the ability of water molecules to passivate the surface trap states of CdSe/ZnS QDs (Fig. 6g).

The humidity sensor shows an estimated sensitivity of 1% RH and outstanding reversibility on alternately cycling from 19% to 54% RH (Fig. 6h). Furthermore, the optical sensor also exhibits a fast response of less than 90 ms (Fig. 6i). Electrospun nanofibers with fluorescent QDs have also been integrated into gas sensors for the detection of volatile organic compounds (VOCs) based on their optical signal of extinction change. For instance, Ag nanoparticles and CdSe–CdS QDs have been embedded together into electrospun PMMA nanofibers to form a freestanding optical sensing material.[136] The detection limit for butanol was estimated to be 100 ppm with a response time lower than 1 min.

4.2.3 Electrochemical sensing. The electrochemical method is one of the most efficient strategies for a large number of target molecule sensings due to its high sensitivity, superior response speed, excellent stability, and low cost.[141] For electrochemical sensing research, it is significantly important to prepare high-performance electrocatalyst-modified working electrodes to enhance the sensing capability. Over the last few decades, metal sulfide nanomaterials have been regarded as efficient sensing candidates resulting from their large catalytic efficiency and brilliant biocompatibility. Through the integration of metal sulfides with 1D electrospun nanomaterials, they have exhibited excellent sensing properties toward dopamine (DA), vanillin, the non-steroidal anti-prostate cancer drug nilutamide, and glucose.[142–145]

An electrochemical DA sensor has been constructed using a WS_2/CNF hybrid modified electrode.[142] CNFs are prepared via an electrospinning and carbonization approach and WS_2 nanospheres are decorated on their surface through a hydrothermal reaction. The synergistic effect between CNFs and WS_2 contributes to the high sensitivity of 5.36 μA μM^{-1} cm^{-2} and low detection limit of 0.01 μM for the detection of DA. In addition, the $WS_2/CNFs$ hybrid-based DA sensor has also shown excellent selectivity toward UA and outstanding reproducibility and long-term stability. These advantages provide the sensor with promising application for real sample analysis. For human urine samples, recoveries range from 99.2% to 102.1% and the relative standard deviation (RSD) ranges from 1.69% to 1.98%.

In addition to the single-component metal sulfides, binary transition metal sulfides have been proved to be efficient sensing materials because of their abundant redox characteristic and high electrochemical properties. For example, a freestanding $NiCo_2S_4$ nanowire array–electrospun graphitic nanofibrous membrane has been prepared via a two-step hydrothermal process as a nonenzymatic glucose sensor.[143] The prepared $NiCo_2S_4$–graphitic nanofibers show a unique core–shell structure and rough surface, providing large active sites for electrochemical sensing. The nanofiber-modified electrode shows an excellent sensing performance to detect glucose, with a high sensitivity of 7431.96 μA mM^{-1} cm^{-2} and a low detection limit of 0.167 mM. Furthermore, the glucose sensor also displays a high selectivity in human serum toward a series of interfering species (UA, DA, AA, lactose, xylose, mannose, urea, KCl) and favorable storage stability, demonstrating promising potential in clinical diagnosis.
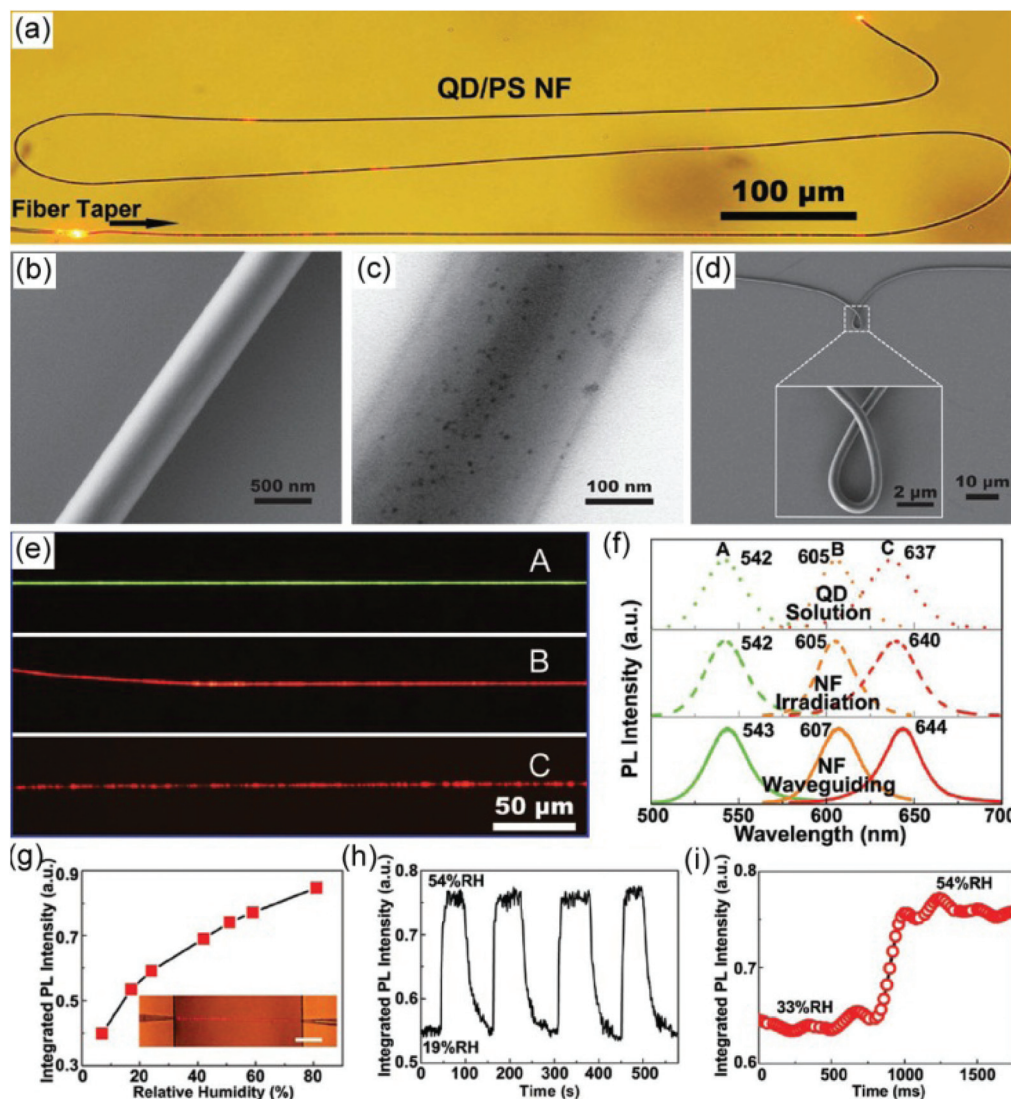
Fig. 6 (a) Optical microscopy image of a single PS/QD hybrid nanofiber under 672 nm light. (b, c) SEM and TEM images of PS/QD hybrid nanofibers. (d) Bending characteristic of a QD/PS nanofiber from an SEM image. (e) PL microscopy images of three PS nanofibers doped with different QDs with emissions of 542 nm, 605 nm, and 637 nm. (f) PL spectra of QDs in chloroform solution (top line); QD/PS nanofibers *via* irradiation excitation (middle line) and waveguiding excitation (bottom line). (g) PL intensity of QD/PS nanofibers exposed to ambient RH ranging from 7% to 81%; the inset shows the optical microscopy image of the nanofiber. (h) Response of the QD/PS nanofiber sensor to alternately cycled 54% and 19% RH air. (i) Time-dependent PL intensity of the QD/PS nanofiber sensor with RH changing from 33% to 54%. Reproduced with permission.[135] Copyright 2011, John Wiley and Sons.

4.3 Catalysis

4.3.1 Heterogeneous chemical catalysis. The integration of nanocatalysts with 1D electrospun nanofibers can restrict their aggregation and leaching during the catalytic process, thus producing large catalytically active sites, which is beneficial for their application in heterogeneous chemical catalytic reactions.[146–149] For example, CoS nanoparticles have been encapsulated into PAN nanofibers *via* a direct electrospinning route, and these show an excellent catalytic performance toward ammonia borane hydrolysis to produce hydrogen.[59] Owing to the unique nanoparticles-in-nanofibers structure, the

hybrid catalyst shows an outstanding reusability. Recently, NiS nanoparticles embedded inside CNFs (NiS@CNFs) have also been prepared *via* a one-step electrospinning and carbonization process.[150] The prepared NiS@CNFs show a large specific surface area (650.9 m^2 g^{-1}), enabling them to be an excellent catalyst for the hydrolysis of ammonia borane. Under a reaction time of 200 min, 3.11 mol H$_2$ mol^{-1} ammonia borane can be achieved from NiS@CNFs, which is better than NiS NPs and Ni@CNFs. Furthermore, a low activation energy (E_a, 25.1 kJ mol^{-1}) is obtained, which is lower than many previous reported Ni-based catalysts, demonstrating the high catalytic activity of the NiS@CNFs. This result indicates that the

integration of metal sulfide with electrospun nanofibers is an efficient candidate toward the catalytic hydrolysis of ammonia borane.

It is well known that metal sulfides have also been used as Fenton-like catalysts. For example, hierarchical 3D CuS structures have been prepared as efficient Fenton-like reagents for dye decolorization.[151,152] Our group has demonstrated that CuS nanoparticles can be decorated on the surface of electrospun PAN nanofibers via a hydrothermal reaction.[151] Owing to the small-sized CuS nanoparticles, a porous and freestanding characteristic of the CuS/PAN nanofibers membrane, they show a good Fenton-like property, which can catalytically degrade methylene blue (MB) in the presence of H_2O_2 efficiently. Within 40 min, about 94.5% MB has been degraded and the reaction rate constant (K_{app}) of the catalytic process is estimated to be 0.0413 L mg^{-1} min^{-1}. Furthermore, the prepared CuS/PAN nanofiber membrane also exhibits a favorable reusability. After five cycles, the degradation efficiency can still reach 80%, demonstrating its potential as a recyclable Fenton-like catalyst.

4.3.2 Photocatalysis. Because of its sustainability and eco-friendly nature, photocatalysis has been broadly connected to address energy crisis and environmental problems.[31,32] For the integration of electrospinning technology with metal sulfides, due to the large surface area and high porosity of electrospun polymeric and carbon nanofibers, they have been proved to be efficient catalyst carriers.[153–183] On the other hand, some ceramic nanofibers from the electrospinning and calcination process can also be directly used as photocatalysts.[89,184–199] Both of the two types of photocatalyst have shown great applications for photodegradation of dyes, photoreduction of heavy metal ions, organic transformation, hydrolysis of ammonia borane, water splitting, and CO_2 reduction, etc.

CdS has been broadly utilized as promising visible-light photocatalyst due to its suitable negative conduction band (CB) edge and ideal band gap energy (2.4 eV). When CdS with a narrow band gap meets the semiconducting TiO_2 under visible light irradiation, electron transfer will occur from the conduction band (CB) of photoexcited CdS to the CB of TiO_2, leading to an efficient electron–hole separation, which is also observed in other hybrid systems.[200–212] Then a high concentration of electrons in the CB of TiO_2 and large amounts of holes in the valence band (VB) of CdS are achieved. The electrons accumulated on TiO_2 can react with the oxygen molecules in the solution to produce $\cdot$OH and superoxide radical anions (O_2^-), which can degrade the organic dyes effectively. To further enhance the photocatalytic performance of CdS-based hybrids, the incorporation of heteroatoms into the CdS structure is a meaningful strategy. In such photocatalysts, more efficient charge transfer can take place in continuous CB and VB, leading to improved photocatalytic activity. For example, hierarchical $Cd_{1-x}Zn_xS/TiO_2$ hybrid nanofibers have been prepared for visible light photocatalysis to degrade RhB molecules.[204] Compared with CdS, the CB bottom potential of $Cd_{1-x}Zn_xS$ will shift to a more positive energy level, resulting in a larger CB difference between TiO_2 and $Cd_{1-x}Zn_xS$. Then

the photoexcited electron–hole separation efficiency is promoted, leading to the improved photocatalytic performance. Moreover, the kind of TiO_2/CdS nanostructure strongly influences their photocatalytic performance. It has been reported that electrospun TiO_2 nanotubes decorated with pine-cone-shaped CdS nanoparticles present a superior photocatalytic activity compared with TiO_2 nanotubes combined with spherical CdS nanoparticles, which can be ascribed to the unique stacking hybrid nanotubular structure for the light and matter transfer capability as well as the realizing of a longer lifetime of charge carriers.[88]

It is well known that infrared light covers 53% of solar energy; therefore, it is a good objective to prepare photocatalysts with upconversion nanoparticles to increase full-spectrum absorption for the improvement of solar light-driven photocatalytic efficiency.[213–215] For example, it has been reported that the incorporation of $NaYF_4$:Yb/Tm@$NaYF_4$ into TiO_2/CdS nanofibers enhances their wide absorption to the near-infrared (NIR) region, which shows a higher photocatalytic activity than the $NaYF_4$:Yb/Tm@$NaYF_4$/TiO_2 hybrid and bare CdS nanospheres.[213] Noble metal modification is another versatile route to enhance the photoexcited charge carrier separation to induce the improved photocatalytic performance.[216] For instance, Pt is usually utilized as an efficient co-catalyst on a CdS/TiO_2 hybrid to achieve a high performance for photocatalytic H_2 production.[217] During the photocatalytic process, Pt can capture the electrons from the CB of TiO_2 originating the transfer from CB of CdS, which will react with water molecules to generate H_2. Meantime, the holes existing in the VB of CdS can react with the sacrificial reagent of SO_3^{2-} and S^{2-} to form SO_4^{2-} and S_2^{2-}. Therefore, the optimized CdS/TiO_2/Pt hybrid nanorods show an excellent photocatalytic activity with a H_2 production rate of 1063 μmol h^{-1} g^{-1}.

Different from the above heterostructured photocatalysts with the electron transfer from the CB of one semiconductor with a narrow band gap to the CB of the other one with a wide band gap, recently, a Z-scheme photocatalytic mechanism has been demonstrated, which involves the migration of electrons and holes to more negative and positive energy levels of photocatalysts, respectively.[90,218–220] Through the integration of metal sulfide with electrospun nanomaterials, several Z-scheme hybrid nanofibers have been prepared for photocatalytic degradation and H_2 production. For example, direct Z-scheme TiO_2/NiS hybrid nanofibers with a core–shell structure have been prepared as a photocatalyst for H_2 generation (Fig. 7a–c).[218] Based on the higher Fermi level of NiS than TiO_2, an internal electric field can be formed at the TiO_2/NiS interface, and then the coulomb repulsion impels the recombination of the electrons in the CB of TiO_2 and holes in the VB of NiS (Fig. 7d–f). The formation of a Z-shape pathway of the charge carriers has been further confirmed by an in situ XPS analysis. It was found that the binding energies of Ti 2p and O 1s of TiO_2/NiS present a positive shift of 0.4 eV, while those of Ni 2p and S 2p show a negative shift of 0.5 eV under UV–vis light irradiation. This result demonstrates an efficient electron transfer from the CB of TiO_2 to NiS, enabling the effective sep-
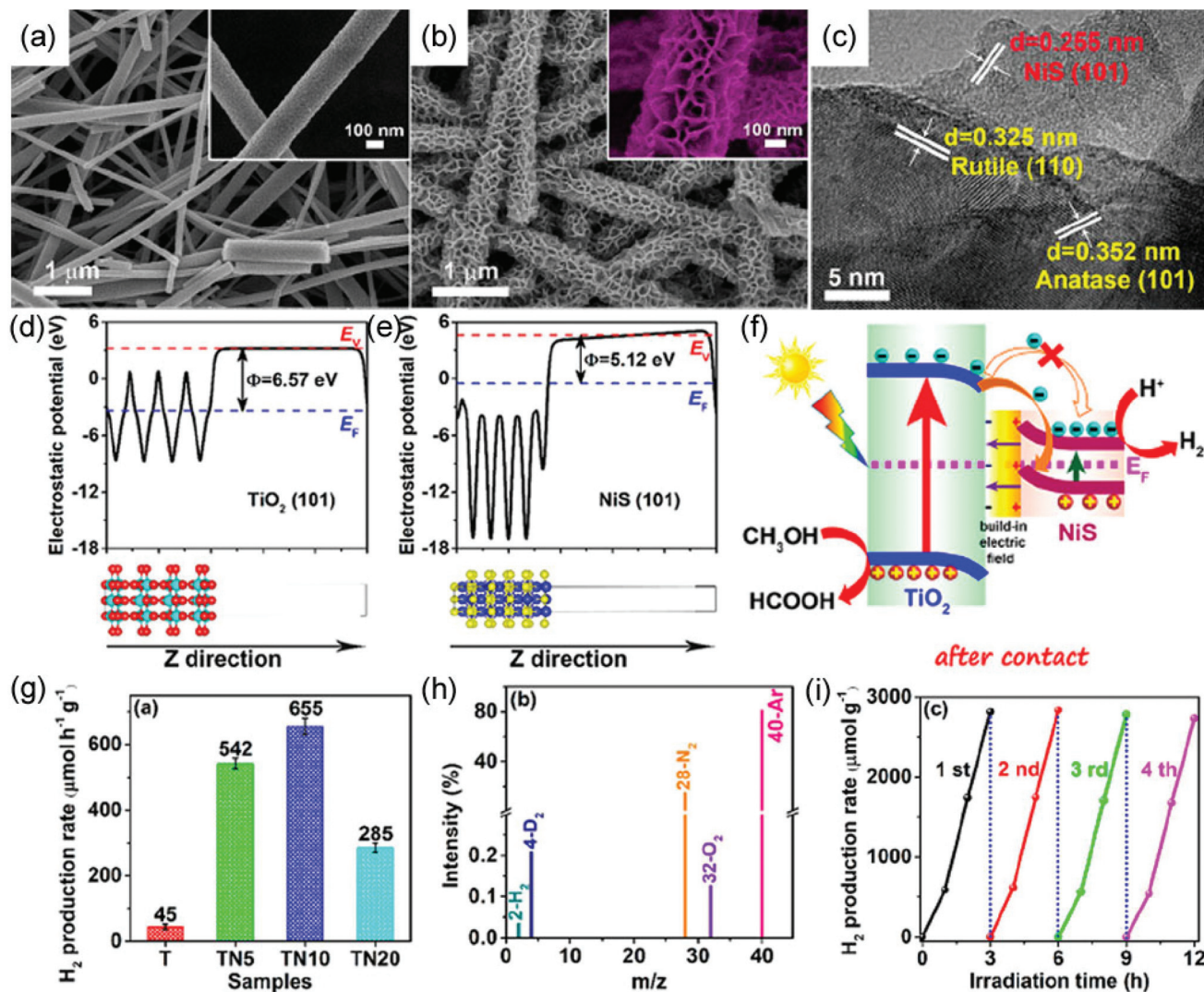
Fig. 7 SEM images of (a) TiO_2 nanofibers and (b) TiO_2/NiS hybrid nanofibers; the insets show the corresponding enlarged SEM images. (c) HRTEM image of TiO_2/NiS hybrid nanofibers. Calculated electrostatic potentials for the (101) face of (d) TiO_2 and (e) NiS. (f) Schematic illustration of TiO_2 and NiS direct Z-scheme heterojunction after contact under UV–visible light irradiation. (g) Comparison of photocatalytic H_2-production activities of different samples. (h) GC-MS spectrum of the photocatalytic system for D_2O splitting. (i) Cyclic performance for H_2 production from the TiO_2/NiS hybrid nanofibers. Reproduced with permission.[218] Copyright 2018, American Chemical Society.

aration of electron–hole pairs and leading to an enhanced photocatalytic activity toward H_2 production. As a result, the optimized TiO_2/NiS hybrid exhibits a H_2 production rate of 655 μmol h^{-1} g^{-1}, which is much higher than that of bare TiO_2 nanofibers (Fig. 7g–i).

4.3.3 Enzyme-like catalysis. The inherent limitations of natural enzymes, such as the high cost of synthesis and purification, low environmental stability and difficulty of storage, stimulate the production and development of varied types of mimic enzymes.[221–223] Compared with natural enzymes, nanozymes are usually low-cost, highly stable and mass-produced.[221–223] Notably, electrospun nanofibers can provide a large surface area and unique charge transfer along one direction, which are favorable for efficient nanozymes or nanozymatic supports.[224–227] In addition, the enzyme-like activity can

be significantly improved by the integration of metal sulfides with other functional nanomaterials through a synergistic catalytic effect.

It has been reported that MoS_2 nanosheets exhibit intrinsic peroxidase-like activity; however, their catalytic performances still need to be enhanced.[228] Recently, TiO_2/MoS_2 hybrid nanofibers with a distinct core–shell nanostructure have been prepared *via* an electrospinning, calcination, and hydrothermal route, which has realized an efficient peroxidase-like activity.[229] Herein, the 2D nanosheet-like MoS_2 provides a large surface area and superior mass transport capability, while the 1D TiO_2 nanofibers offer an excellent electron transfer property. Therefore, with the unique 1D/2D hierarchical structure and the interfacial charge transfer-induced synergistic effect, the obtained TiO_2/MoS_2 core–shell hybrid nanofibers

present a better catalytic activity than the bare TiO_2 nanofibers and individual MoS_2 nanosheets. Furthermore, the thickness of MoS_2 nanosheets on TiO_2 nanofibers has a significant influence on their catalytic property. It was found that only a suitable thickness of the MoS_2 nanosheets is in favor of enhancing the peroxidase-like catalytic activity. In terms of the high peroxidase-like activity of this nanozymatic system, a simple visual route is developed to detect L-glutathione (GSH) with a high sensitivity. To further investigate the interfacial engineering to tailor the enzyme-like activity of MoS_2 materials, ternary $TiO_2@MoS_2/CoFe_2O_4$ nanofibers have been prepared via a similar strategy (Fig. 8a).[230] The ternary nanofibers consist of uniform MoS_2 nanosheets on the surface of TiO_2 nanofibers and the encapsulation of $CoFe_2O_4$ nanoparticles in the MoS_2

nanosheets (Fig. 8b–i). Resulting from the unique 1D structure and strong interfacial interactions, the ternary $TiO_2@MoS_2/CoFe_2O_4$ hybrid nanofibers deliver a superior peroxidase-like property, which is much higher than TiO_2, MoS_2, $CoFe_2O_4$, $TiO_2@MoS_2$, and $TiO_2/CoFe_2O_4$ (Fig. 8j–l). This peroxidase-like property can be utilized to construct a sensing platform to sensitively detect L-cysteine.

Recently, conducting polymers have been proved to significantly enhance the enzyme-like properties of nanozymes.[231–233] The abundant functional groups of conducting polymers offer a better affinity of the hybrid nanozyme, providing an excellent kinetic process. In addition, the outstanding electron transfer capability is beneficial for the generation of $^{\bullet}OH$ radicals to accelerate the peroxidase-like activity. As a
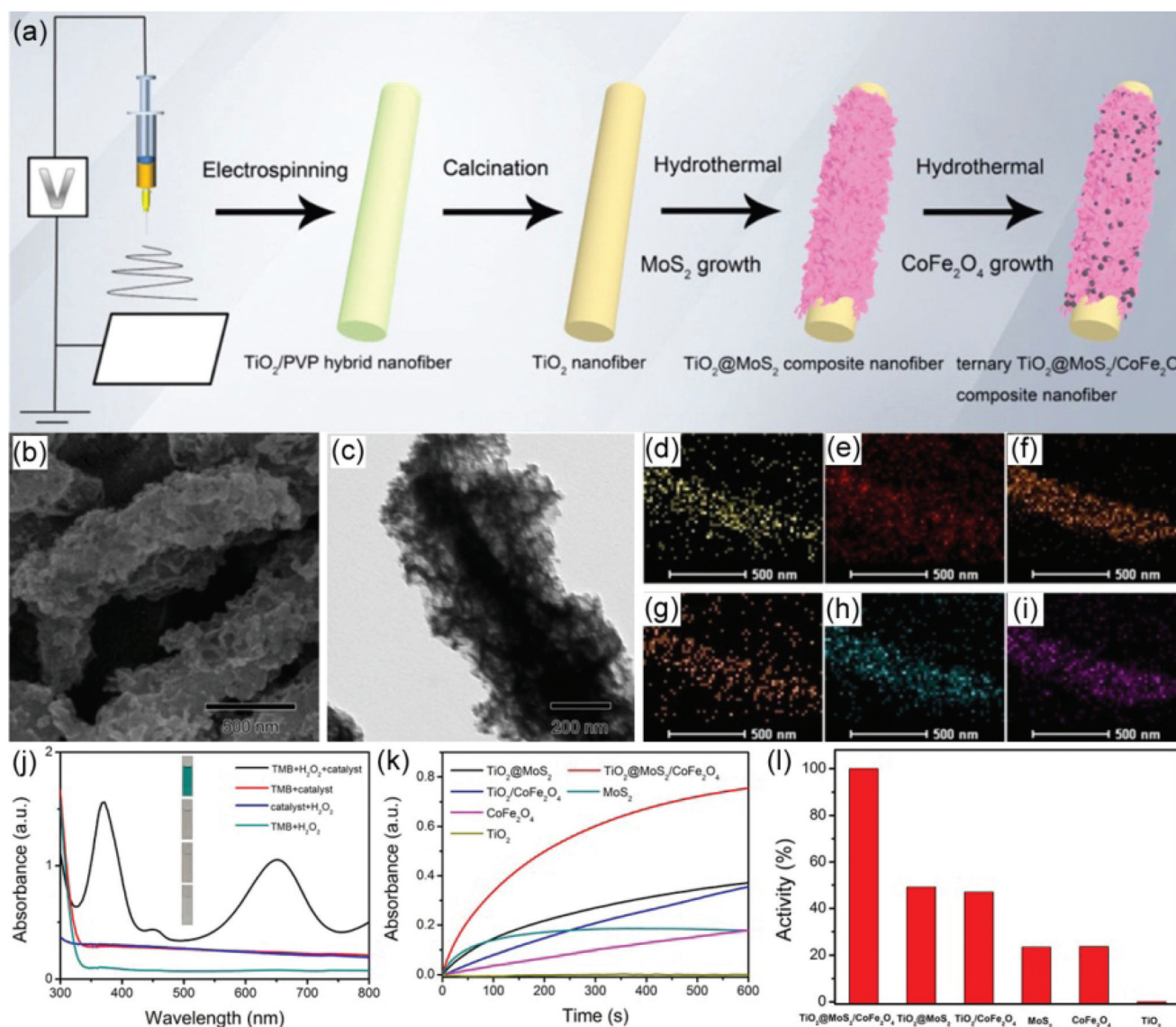
Fig. 8 (a) Schematic illustration of the preparation procedure for $TiO_2@MoS_2/CoFe_2O_4$ hybrid nanofibers. (b–i) SEM, TEM images and EDX mapping of the prepared $TiO_2@MoS_2/CoFe_2O_4$ hybrid nanofibers. (j) UV–visible absorption spectra of different peroxidase-like reaction systems. (k) Time-dependent absorbance change of the peroxidase-like reaction system catalyzed by varied catalysts. (l) Comparison of the peroxidase-like catalytic activities of different catalysts. Reproduced with permission.[230] Copyright 2019, Elsevier.

typical example, ternary $CuFe_2O_4/Cu_9S_8$/polypyrrole (PPy) nanotubes have been prepared via an electrospinning, annealing and hydrothermal reaction, which displays a relatively good distribution of PPy layers on the surface of $CuFe_2O_4$ nanotubes.[234] On utilization as a peroxidase-like catalyst, the obtained ternary $CuFe_2O_4/Cu_9S_8$/PPy nanotubes exhibit superior catalytic efficiency over the individual $CuFe_2O_4$ nanofibers, $CuFe_2O_4$/CuO hybrid nanofibers, $CuFe_2O_4$/CuS hybrid nanofibers, as well as PPy materials alone, demonstrating a synergistic effect among the three components.

4.4 Energy storage and conversion

4.4.1 Water splitting. Electrospun nanofibers possess a large surface area and brilliant conductivity along the long axis, so they can act as good catalysts and catalyst carriers for the electrochemical water-splitting reaction.[42,235,236] The integration of metal sulfides and electrospun nanofibers is a convenient way to prepare electrocatalysts with high efficiencies.[237–258] CNFs derived from electrospun nanofibers show a small diameter, high electrical conductivity, and flexibility, and are ideal supports for metal sulfides for water-splitting applications. The integration of metal sulfides with CNFs can not only provide efficient pathways for electron/ion transport, but also enhance the conductivity and structural integrity of the hybrid during the electrochemical process. For example, $CNF@CoS_2$ hybrid nanofibers with a hierarchical core@sheath structure via electrospinning and hydrothermal reactions have been demonstrated.[259] Resulting from the unique electron and mass transport capability of CNFs and the electrocatalytically active CoS_2 nanoparticles, the obtained electrocatalyst displays a superior hydrogen evolution reaction (HER) performance in a large pH range. Indeed, a low onset potential of −40 mV, a small Tafel slope of 66.8 mV per decade, a large current density of η = 110 mV at a current density of 10.0 mA cm^{-2} in acid media, as well as remarkable activities in alkaline and neutral media have been reported. Heteroatom-doped CNFs have also been applied in electrocatalytic water splitting because of their improved electrical conductivity. Free-standing amorphous flower-like molybdenum sulfides@nitrogen-doped CNFs (MoS_x@NCNFs) membranes have been developed for HER application.[260] Owing to the unique structure of amorphous flower-like MoS_x, exposing abundant active edge sites, and the synergistic effect between NCNFs and amorphous MoS_x, a superior electrocatalytic HER activity has been reported, that is an overpotential of 137 mV at 10 mA cm^{-2} and a Tafel slope of 41 mV per decade. Furthermore, this electrocatalyst shows a favorable long-term stability for HER with only a small change of the cathodic current after 1000 cycles.

The aforementioned results have shown that CoS_2 and MoS_x-based materials are good electrocatalysts for HER. To further enhance the HER performance, it is generally considered that an interfacial engineering modulation of two metal sulfides is an efficient route to tailor the HER performance. Recently, Co_9S_8/WS_2 nanostructures with two different heterointerfaces including a Co_9S_8 core@full WS_2 shell (Co_9S_8/FWS_2) and Co_9S_8 core@half WS_2 shell (Co_9S_8/HWS_2) have been

prepared on the surface of CNFs for electrocatalytic overall water splitting.[261] As the prepared Co_9S_8–HWS_2/CNFs show excellent HER and oxygen evolution reaction (OER) activity in an alkaline solution, an electrolyzer assembled with them as both anode and cathode has been prepared, displaying an operating voltage of 1.60 V, which is superior to the water-splitting device assembled with IrO_2/C and Pt/C catalysts (Fig. 9a). This electrolyzer also shows an outstanding stability with a constant current density of around 100 mA cm^{-2} over 10 h (Fig. 9b and c). The theoretical results reveal that Co_9S_8/HWS_2 offers more exposed Co–S–W interfaces, resulting in abundant lone-pair electrons on the edged S atoms to optimize the kinetic adsorption energy of hydrogen intermediates, which significantly enhances the HER efficiency (Fig. 9d–h). In addition, the distinct Co_9S_8/HWS_2 structure enables the interactions between the two types of sulfide and electrolyte, which promotes the adsorption of both hydrogen and oxygen intermediates, leading to an improved HER and OER performance.

Heteroatom doping is another strategy to modulate the electronic structure of the catalyst to promote water-splitting catalytic reactions. In addition, the introduction of carbon nanotubes (CNTs) is also a versatile way to enhance the electrocatalytic activity due to the improved electrical conductivity. For example, phosphorus (P)-doped $NiCo_2S_4$@CNT/CNF hybrid nanofibers have been prepared via an electrospinning, calcination, hydrothermal and phosphidation process.[262] It was found that $NiCo_2S_4$ is grown on the CNF perpendicularly, which provides more electrocatalytically active sites. Furthermore, the introduction of CNTs into the hybrid improves the electrical conductivity and the doping with P reduces the kinetic energy barrier. Thus, the obtained P-doped $NiCo_2S_4$@CNT/CNF hybrid nanofibers exhibit a superior HER activity with a low overpotential of 74 mV at a current density of 10 mA cm^{-2} in an acidic solution. The prepared P-doped $NiCo_2S_4$@CNT/CNF hybrid nanofibers also display an excellent long-term stability toward HER, offering only a small decrease of the current density over 10 h and almost no obvious change in the polarization curve after cycling. The superior stability of the catalyst was attributed to the unique structure of the 1D CNFs and to the hierarchical morphology of the hybrid material that was retained after the HER process.

4.4.2 Solar cells. Dye-sensitized solar cells (DSSCs), which work on the basis of a photosensitized anode, a counter electrode (CE) and the reversible redox of electrolytes, are widely concerned for their unique performance, environmental friendliness, high extinction coefficient and favorable power conversion efficiency (PCE).[263,264] Resulting from the high conductive transport capability and abundant active sites for catalysis, CNFs are usually supports for cobalt sulfides for DSSCs.[265–269] For instance, Co_9S_8 nanoparticle/CNF hybrid materials have been developed as an efficient and low-cost Pt-free CE for DSSCs.[270] Because of the low charge resistance, large surface area and improved electrical conductivity of the hybrid, DSSCs constructed with the Co_9S_8/CNFs as a CE achieve a PCE of 8.37%, which is comparable to that of the Pt-based CE. Therefore, the Co_9S_8/CNFs show great potential to

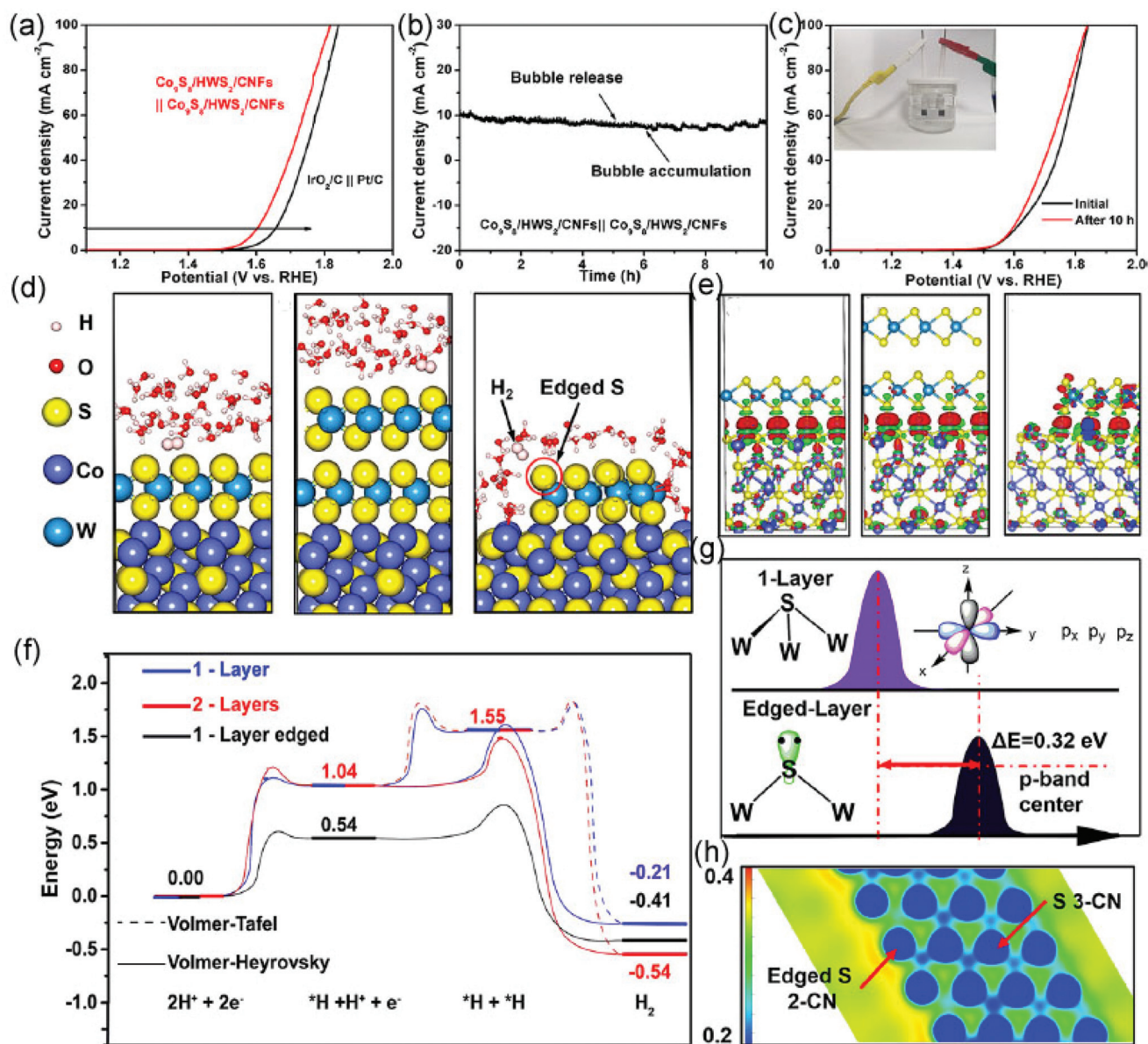**Fig. 9** (a) Linear sweep voltammetry curves of the electrolyzer based on $Co_9S_8/HWS_2/CNFs||Co_9S_8/HWS_2/CNFs$ and $IrO_2/C||Pt/C$ catalysts in an alkaline solution. (b) Chronoamperometric curves of the electrolyzer using $Co_9S_8/HWS_2/CNFs$ as cathode and anode under 1.6 V for 10 h. (c) Linear sweep voltammetry curves of the above electrolyzer before and after 10 h testing. (d) DFT calculations of the final steps of H_2 production on the surface of $Co_9S_8/FWS_2/CNFs$ with one-layer WS_2 (left), $Co_9S_8/FWS_2/CNFs$ with two-layer WS_2 (middle), and $Co_9S_8/HWS_2/CNFs$ with one-layer WS_2 (right). (e) Electron density differences among the catalysts, where red and green represent the increase and depletion of electron density, respectively. (f) Reaction energy diagrams of the different catalysts during the HER process. (g) S 3p band center of 3-CN and 2-CN S atoms. (h) Electrostatic potential of 3-CN and 2-CN S atoms. Reproduced with permission.[261] Copyright 2020, American Chemical Society.

replace traditional Pt CE electrodes in DSSCs. Another example of Co_3S_4/CNFs has also been prepared *via* an electrospinning and hydrothermal process as a CE for DSSCs (Fig. 10a).[271] TEM images clearly show that Co_3S_4 nanoparticles are uniformly distributed on the surface of CNFs (Fig. 10b). The prepared Co_3S_4/CNFs deliver a superior PCE of 9.23% in the assembled DSSC, which is higher than the commercial Pt CE (8.38%), bare Co_3S_4 CE (6.77%) and individual CNFs CE (6.04%) (Fig. 10c). The incident monochromatic photon-to-

current conversion efficiency (IPCE) results show that the short-circuit current density (J_{sc}) value of the DSSC with Co_3S_4/ECs CE is higher than that of the other CEs (Fig. 10d). The superior catalytic activity is attributed to the interfacial charge-transfer process between surface electrons in Co_3S_4/CNFs and Co^{3+} ions in the electrolyte, which has been confirmed by the electrochemical impedance spectroscopy and Tafel polarization measurements. To further demonstrate the redox characteristics of different cations in a crystal structure, binary metal
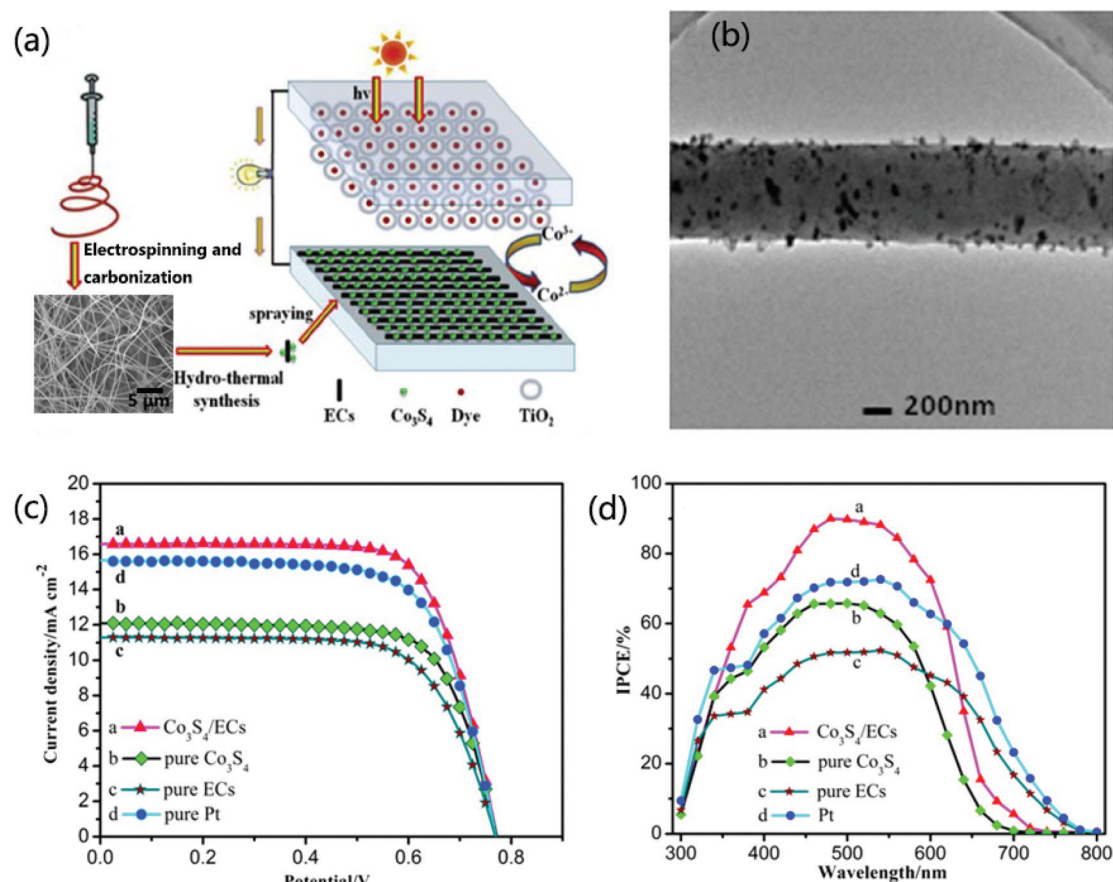
Fig. 10 (a) Schematic drawing of the dye-sensitized solar cells with the Co_3S_4/CNFs as counter electrode. (b) TEM images of Co_3S_4/CNFs. (c) Photocurrent density–photovoltage curves of different counter electrodes. (d) IPCE spectra of different counter electrodes. Reproduced with permission.[271] Copyright 2016, Elsevier.

sulfides have also been utilized as CEs in DSSCs, intrinsically exhibiting an enhanced electrical conductivity and catalytic activity.[272–274] The integration of $NiCo_2S_4$ with CNFs as a CE in DSSCs displays a large PCE (9.0%) and stability, which is better than that of Pt-based CE (7.48%). Recently, CNFs decorated with morphology-controlled $NiCo_2S_4$ nanoparticles and nanorods have been prepared as CEs in DSSCs, showing a better PCE for $NiCo_2S_4$ nanorods/CNFs CE than for $NiCo_2S_4$ nanoparticles/CNFs CE, which was attributed to the larger amount of exposed electrochemically active sites and rapid electron transfer capability of the $NiCo_2S_4$ nanorods/CNFs electrode.[275]

Recently, QD-sensitized solar cells (QDSSCs) have captured more and more interest because of the efficient charge separation capability from the quantum confinement effect of the QDs sensitizers and their tailored spectral characteristic with tunable sizes.[276–283] Two typical QDs including CdS with a size of 18 nm and CdSe with a size of 8 nm have been utilized as sensitizers to electrospun TiO_2 nanofibers.[276] Then the QDs-sensitized TiO_2 nanofibrous electrode was constructed as a sandwich-type solar cell with the electrolyte of polysulfide. The results demonstrate that the QDSSC constructed from the coupling CdS and CdSe QDs with an optimized ratio on TiO_2

nanofibers represents an open-circuit voltage (0.64 V) with 2.69% efficiency, which is better than single QD-sensitized TiO_2 nanofibrous electrode. The high performance of the QD-sensitized electrode can be attributed to the large interfacial area from the coupled QDs, outstanding charge transport from TiO_2 fibers, and excellent electrolyte penetration from the whole porous network.

Recently, hybrid solar cells (HSCs) based on the electrospun TiO_2 nanofibers and poly(3-hexylthiophene) (P3HT) have also been constructed.[284] To increase the light harvesting, Sb_2S_3 is used as a sensitizer to achieve an obvious absorption in a visible range. In addition, a pretreatment by THF vapor is utilized to realize the enhanced contact between inorganic and organic components, which is beneficial for the better charge transport. As a result, the optimized resultant HSCs based on the integration of electrospun TiO_2 nanofibers and P3HT exhibit a PCE of 2.32%, with an enhancement of over 175% compared with the lack of pretreatment by tetrahydrofuran vapor and the absence of Sb_2S_3 sensitizer.

4.4.3 Rechargeable batteries. Lithium ion batteries (LIBs) are widely employed in our daily life, such as in portable electronic equipment and vehicles. The performance of LIBs is strongly correlated with the electrode materials.[285] Metal sul-

fides are considered to be a type of superior electrode materials for LIBs, and they are able to possess sufficient electrochemical performance based on their rich redox reactions and large theoretical capacity, although they suffer from a low electrical conductivity and poor cycle life. Thus, the integration of metal sulfide with high-conductive carbon materials is an efficient route to achieve a high-performance electrode for LIBs.[286–306] MoS_2 is a novel transition metal sulfide with a unique S–Mo–S layered structure, enabling easy lithiation/delithiation of Li^+ during the charge/discharge processes. Through the integration of MoS_2 with electrospun CNFs, a series of high-performance anodes for LIBs has been achieved.[307–320] For instance, a self-standing membrane consisting of porous CNFs (PCNFs) anchored with MoS_2 nanosheets has been constructed.[307] The unique open structure of PCNFs offers the rapid diffusion of both Li^+ and electrons, as well as the restriction of MoS_2 nanoparticle aggregation. As a result, the PCNFs@MoS_2 hybrid nanofibers display an excellent electrochemical performance for lithium storage, including a high specific capacity (954 mA h g^{-1}) in the initial cycle, high-rate capability (475 mA h g^{-1} at 1 A g^{-1}), and excellent cycling stability (almost no capacity loss after 50 cycles).

Similarly, metal sulfides are also proved to be promising anode materials for sodium ion, potassium ion, and aluminum ion batteries (SIBs, PIBs, and AIBs) to show a large theoretical capacity and excellent reversibility. To be integrated with CNFs, the electronic conductivity and cycling stability of the electrodes can be further improved, which is beneficial for the electrochemical performance of the SIBs, PIBs, and AIBs.[75,321–347] For example, recently, amorphous and graphite carbon-encapsulated CoS_2 nanoparticles decorating N-doped porous CNFs (AGC-CoS_2@NCNFs) have been prepared derived from a Zn/Co metal–organic framework (MOF).[321] The reasonable composition and unique structure provide the obtained AGC-CoS_2@NCNFs with favorable conductivity and rapid diffusion of Na^+. Thereby, employing this as an anode for SIBs, the prepared AGC-CoS_2@NCNFs electrode delivers a high initial specific capacity of 876 mA h g^{-1} at 100 mA g^{-1}. In addition, the capacity remains at 148 mA h g^{-1} at 3.2 A g^{-1} after 1000 cycles, displaying a satisfactory stability. It is generally accepted that a 1D nanostructure exhibiting a large specific surface area provides a superior structural stability, presenting a reduced volume change during the cycling process, which contributes to an outstanding stability of the obtained AGC–CoS_2@NCNFs electrode. Similarly, the integration of $NiCo_2S_4$ nanorods with hollow nitrogen-doped CNFs ($NiCo_2S_4$@N–HCNFs) has been used as self-supported anode material for KIBs, presenting a favorable initial capacity and excellent stability after 600 cycles.[336] In recent studies, AIBs have been regarded as forward-looking energy storage devices owing to their large specific capacity, high security and low costs. Self-supported MoS_2/CNF membrane has also been utilized as an electrode material for AIBs; this exhibits a discharge capacity of 293 mA h g^{-1} in the first circle at 100 mA g^{-1} and maintains 126.6 mA h g^{-1} over 200 cycles, representing a great potential for practical applications.[338]

Compared with LIBs, lithium–sulfur batteries (LSBs) have captured more and more attention in terms of their large theoretical specific capacity (1675 mA h g^{-1}) and high energy density (2600 W h kg^{-1}).[348] During the electrochemical reactions in LSBs, a series of lithium polysulfides (Li_2S_x) will be produced in the electrolyte, which has much influence on the cycling performance of LSBs. Recently, metal sulfides have been employed as efficient cathodes for LSBs because they possess not only a large electrochemical activity but also the capability to restrain the shuttle effect of Li_2S_x.[349–351] Integrated with metal sulfides with electrospun nanofibers, a CNF@WS_2@Co_9S_8 hybrid has been prepared with a morphology of hexagonal WS_2-rimmed Co_9S_8 nanoflakes on CNFs (Fig. 11a–h).[348] The prepared CNF@WS_2@Co_9S_8 exhibits the advantages of not only the high adsorption effect of WS_2 but also outstanding electron transport ability from the high-conductive Co_9S_8 and CNFs (Fig. 11i). Therefore, the CNF@WS_2@Co_9S_8 electrode for LSBs shows a large capacity of 1175 mA h g^{-1} at 0.1C, good rate capability to remain at 77.85% at 2.0C, and excellent cycling stability with a high capacity of 572 mA h g^{-1} over 1000 cycles (Fig. 11j–l). The superior stability of the CNF@WS_2@Co_9S_8–S electrode can be ascribed to the outstanding redox behavior and electron transport capability of Co_9S_8 as well as the high polarity of the hexagonal WS_2 edge in the hybrid nanofibers to fix lithium polysulfides (LPSs) via a strong interaction. Additionally, the CNF skeletons also contribute to the whole stabilization of the materials to ensure efficient electron and ion transport during the electrochemical process. Furthermore, the morphology changes are studied in situ by field-emission SEM (FESEM) to explore the relationship between the structure and electrochemical properties, demonstrating the uniform distribution of elemental sulfur (S_8) molecules on the surface of CNF@WS_2@Co_9S_8 nanofibers during the cycling measurement while the length of the nanofibers is reduced with an increasing number of cycles. Similarly to the LSBs, sodium–sulfur batteries (SSBs) have also been widely studied. For example, the SSB assembled with a self-supported S@Ni-NCF electrode shows a large capacity of 738.7 mA h g^{-1} at 0.2C and retains 249.8 mA h g^{-1} at 2.0C, demonstrating a favorable electrochemical performance.[352] Interestingly, an in situ Raman study has been carried out to evaluate the variation of polysulfide during the charging and discharging process. The in situ Raman analysis suggests that the main characteristic peaks of S_8 are at 259 and 456 cm^{-1}, Na_2S_6 and Na_2S_4 at 374 and 473 cm^{-1}, and Na_2S at 428 cm^{-1} when the battery is in static state and discharging to 2.3 V and 1.2 V, respectively. Afterward, the typical peak of Na_2S_6 at 375 cm^{-1} is observed when the cell is charged to 1.8 V, while the peaks of S and Na_2S are observed after being charged back to 2.8 V. This result reveals that the electrochemical process is partially reversible. The initial capacity of the S@Ni-NCF cathode at 1.0C is about 431 mA h g^{-1} and a capacity of 233 mA h g^{-1} is retained after 270 cycles.

Metal–air batteries are another type of rechargeable battery with an ultrahigh energy storage capability.[353–355] For example,
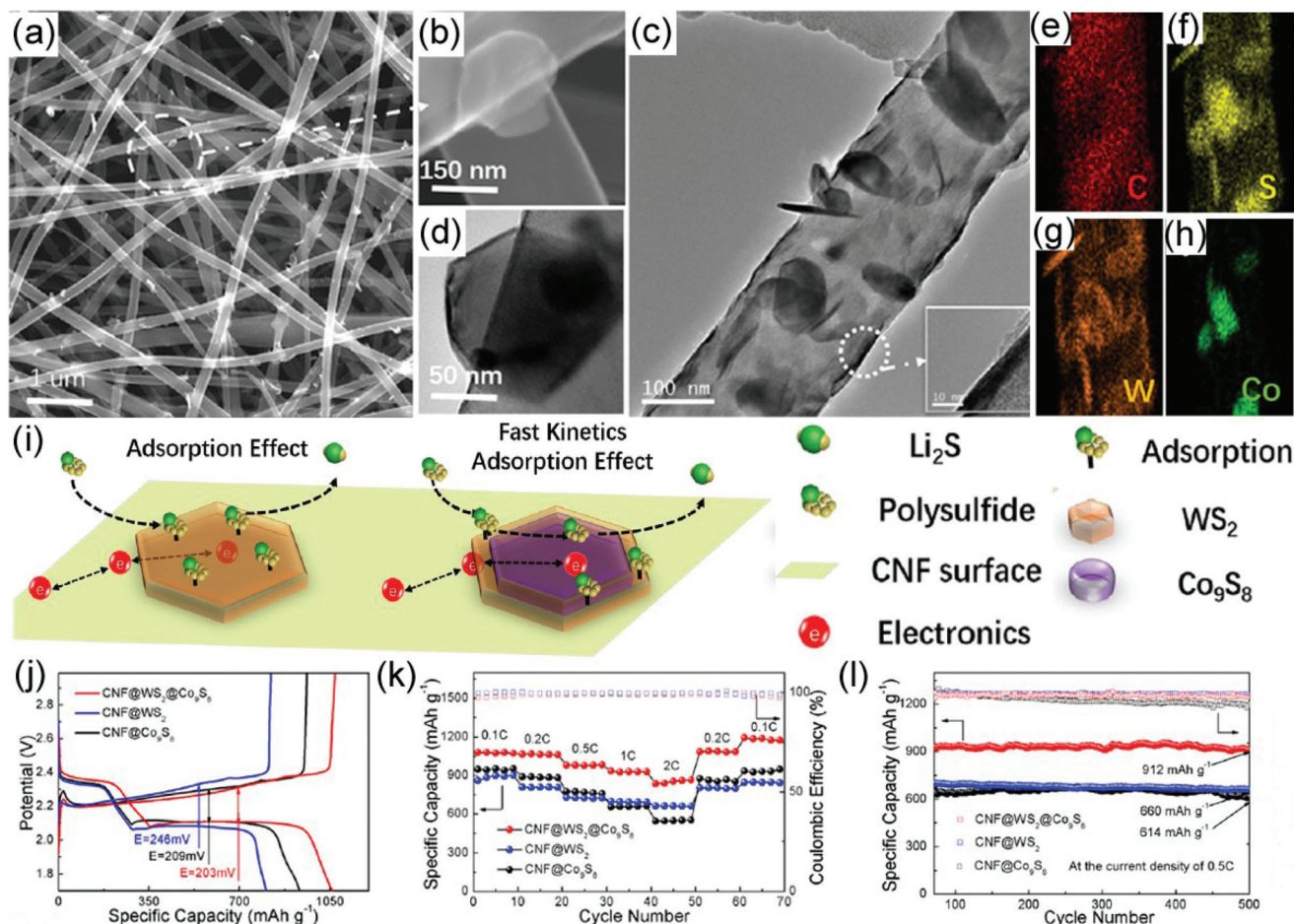
Fig. 11 (a, b) SEM images of the free-standing CNF@WS$_2$@Co$_9$S$_8$ hybrid nanofibers. (c, d) TEM images of the free-standing CNF@WS$_2$@Co$_9$S$_8$ hybrid nanofibers. (e–h) EDS elemental mapping images of C, S, W, and Co in a CNF@WS$_2$@Co$_9$S$_8$ sample. (i) Schematic demonstration of enhanced adsorption and catalysis of soluble lithium polysulfide in a CNF@WS$_2$@Co$_9$S$_8$ sample. (j) Charge/discharge profiles, (k) rate capabilities, and (l) cycling performance of CNF@WS$_2$, CNF@Co$_9$S$_8$, and CNF@WS$_2$@Co$_9$S$_8$ cathodes with sulfur loading of 1.5 mg cm^{-2}. Reproduced with permission.[348] Copyright 2020, Elsevier.

Li–O$_2$ and Al–air batteries possess high theoretical energy densities of 11 140 W h kg^{-1} and 8135 W h kg^{-1}, respectively, which are thirty and twenty times higher than LIBs.[353] In a typical example, Co$_9$S$_8$ nanoparticle-embedded graphitic layers decorated on N,S dual-doped porous CNFs (Co$_9$S$_8$@G/NS-PCNFs) have been prepared as free-standing bifunctional electrodes for both Li–O$_2$ and Al–air batteries.[353] In this hybrid system, the N,S dual-doped porous CNFs offer abundant active sites, enabling excellent electron and mass transport as well as electrolyte immersion. In addition, the stabilization of the graphitic carbon for Co$_9$S$_8$ and its outstanding electrochemical property are beneficial to the superior energy storage performance. As a result, the Li–O$_2$ battery assembled with Co$_9$S$_8$@G/NS-PCNFs shows a high discharge capacity of 8269 mA h g^{-1} at 100 mA g^{-1} and a small polarization gap of 1.52 V. The Al–air battery exhibits a large specific capacity of 2812 mA h g^{-1} at 35 mA cm^{-2} and a peak power density of 79.04 mW cm^{-2}, which can be attributed to the superior electrocatalytic activity of Co$_9$S$_8$ nanoparticles and the distinct 1D nanostructure of

the NS-PCNFs. Furthermore, the catalyst presents a much better cycling stability than a 20 wt% Pt/C cathode, which is due to the free-standing structure that facilitates the O$_2$ and Li$^+$ transfer. In addition to Al–air batteries, zinc–air batteries (ZABs) are one of the most widely studied for practical application due to their low cost and high safety.[356,357] With an outstanding bifunctional OER and ORR performance, together with an excellent mechanical flexibility, CuCo$_2$S$_4$ nanosheets@NCNFs have been proved to be efficient electrodes for ZABs.[356] The ZAB battery assembled with CuCo$_2$S$_4$ nanosheets@NCNFs delivers a superior specific capacity of 896 mA h g^{-1}, a large open-circuit potential of 1.46 V, and excellent bending stability with a 93.62% capacity retention over 1000 cycles. Recently, MOF-derived porous FeS$_2$–CoS$_2$/NCFs have been prepared by combining electrospinning and atomic-layer deposition. They exhibit excellent bifunctional electrocatalytic activities for both ORR and OER in an alkaline electrolyte.[358] Finally, a flexible solid-state Zn–air battery, which has been assembled with porous FeS$_2$–CoS$_2$/NCFs, has

been demonstrated to be able to stably power LED panels at a bending state.

4.4.4 Supercapacitors. With the increasing demand for clean and sustainable energies, the development of supercapacitors has been promoted in terms of their large power energy, rapid recharge capability, long cycling life, and superior safety. Based on the large specific surface area, low density, good directivity and easily tailored composition, electrospun nanomaterials have been considered to be a type of ideal electrode material in supercapacitors.[359] During the last years, a large number of electrospun materials including CNFs, metal oxides, metal sulfides and their hybrids have been employed as efficient electrode materials.[360–364] Among those, the integration of metal sulfides with CNFs provides abundant redox processes and excellent electrical conductivity, representing high electrochemical activity and outstanding long-term stability.[365–373] For instance, CoS_x/C hybrid nanofibers have been prepared *via* an electrospinning, carbonization and hydrothermal reaction.[365] In the CoS_x/C hybrid, the obtained CoS_x nanoparticles are hollow and covered by a layer of onion-like carbon, which promotes their electrical conductivity. In addition, such a structure also reduces the volume change during the charging/discharging process, enabling a good cycling stability. As a result, the obtained CoS_x/C hybrid nanofibers deliver a large specific capacitance of 496.8 F g^{-1} at 0.5 A g^{-1}, a favorable rate capability to maintain the capacitance of 66.1% at 100 A g^{-1}, and outstanding cycling stability with a specific capacitance retention of 89.4% over 2000 cycles. In addition, an asymmetric supercapacitor has been constructed with a CoS_x/C hybrid nanofibers//PCNFs system, displaying a positive energy density of 15.0 W h kg^{-1} at a power density of 413 kW kg^{-1}. In addition to single metal sulfide, binary metal sulfides have also been utilized as supercapacitor electrodes.[374–378] For example, vertically aligned $NiCo_2S_4$ nanosheet arrays supported on CNFs have been prepared.[374] After the modification of PPy, the CNFs/$NiCo_2S_4$@PPy electrode represents an ultrahigh specific capacitance of 2961 F g^{-1} at 1 A g^{-1}. Furthermore, the electrode retains 99.85% of the initial capacitance over 5000 cycles, indicating a superior cycling stability. After the cycling test, the morphology of the catalyst is still intact due to a strong interaction between the $NiCo_2S_4$@PPy and the CNFs.

Recently, MOFs and their derivatives have been demonstrated to be efficient electrode materials for supercapacitors.[379–381] The metal sulfides derived from MOFs show the advantages of a large surface area and abundant pores, benefiting electrolyte transport. Recently, hierarchical Ni/Ni_3S_2-decorated CNFs derived from a pre-oxidized electrospun polyacrylonitrile (PAN)@Ni–MOF hybrid have been prepared for supercapacitor electrodes (Fig. 12a).[382] In such a hybrid system, Ni and CNFs provide high electrical conductivity and Ni_3S_2 offers a superior pseudocapacitance; meanwhile, the hierarchical structure supplies a large number of exposed redox active sites (Fig. 12b–g). Thereby, as electrodes, the hierarchical Ni/Ni_3S_2/CNF electrode represents a high electrochemical performance with a specific capacitance of 830.0 F g^{-1} at 0.2 A g^{-1} and a favorable rate performance with 42.4% of the original capacitance at 5 A g^{-1} (Fig. 12h–j). Assembled with the Ni/Ni_3S_2/CNFs as the positive electrode and active carbon as the negative electrode, an asymmetric supercapacitor device shows a large energy density of 31.6 W h kg^{-1} at a power density of 1800 W kg^{-1} and a superior capacitance retention of 95.7% after 5000 charge–discharge cycles (Fig. 12k–m). This study demonstrates that MOF-derived materials are promising for supercapacitor electrodes exhibiting both high electrochemical activity and excellent cycling stability.

4.5 Thermal shielding

Thermal shielding materials can filter the NIR radiation in the solar spectrum, which effectively isolates the thermal energy. Thermal shielding materials have been broadly applied in the windows around buildings and automobiles. Noble metals such as Au and Ag, and some metal-doped metal oxides such as VO_2 and WO_3, are the traditional thermal shielding materials. Recently, metal sulfides (CuS) have been explored to show a strong absorption in the NIR region in terms of the surface plasmon resonance (SPR) effect, and these have potential for thermal shielding applications.[54] To achieve a perfect dispersion of CuS in a polymer to coat on the surface of a substrate, the integration of CuS nanoparticles with electrospun polymer nanofibers is an efficient strategy. Based on these ideas, CuS/PVP hybrid nanofibers have been prepared *via* a direct electrospinning method as discussed above. Fluorination-treated glass, polyethylene terephthalate (PET), and polyethylene naphthalate (PEN) substrates with negative charges are utilized to deposit CuS/PVP hybrid nanofibers with positive charges through electrostatic interactions to achieve an intact film. It is found that the obtained CuS/PVP fibrous films on varied substrates are highly transparent, and an optimized membrane shows a large transmittance of 68.8% at 550 nm and a low haze factor of 1.89% (Fig. 13a–c). This result demonstrates that the prepared CuS/PVP fibrous films on certain substrates are suitable for window application. In addition, the CuS/PVP fibrous film on PET substrates exhibits an excellent flexibility with almost no changeable NIR shielding efficiency and haze factor as well as superior reliability with high temperature and humidity. For practical application, the thermal shielding film has been attached on the windows of a car. Then the inside temperature has been measured, showing an enhanced shielding efficiency compared with bare and commercial Cs-doped WO_3 film (Fig. 13d). Similar results have also been observed when monitoring the interior air in a simulated building, demonstrating the promising potential in our daily life (Fig. 13e).

4.6 Adsorption and separation

Nowadays, water pollution treatment has stimulated tremendous attention globally. Adsorption techniques are regarded as one of the most simple and effective ways to remove pollutants from water.[383] Over the last years, electrospun nanofibrous membranes have captured increasing attention for adsorption
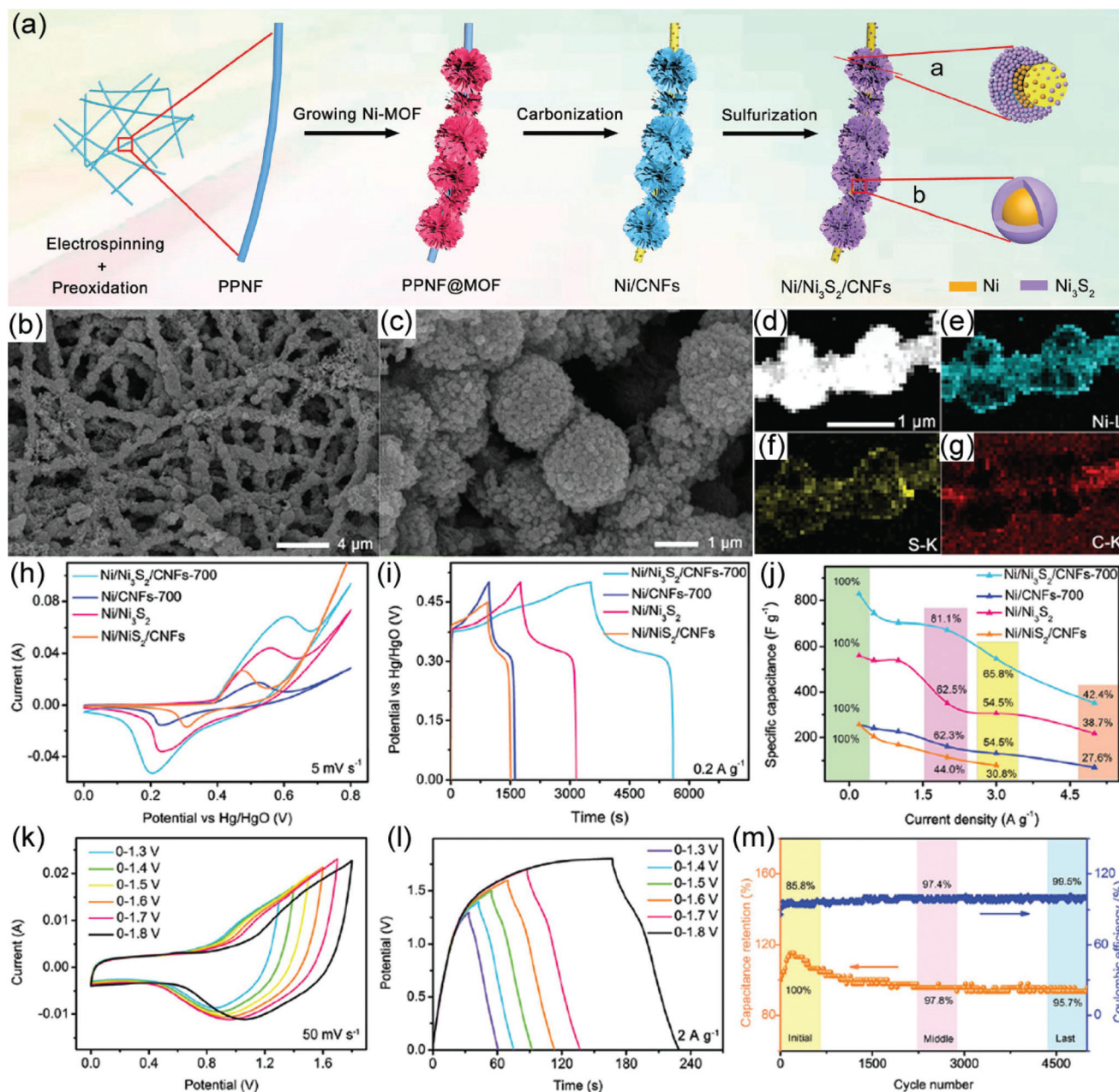
Fig. 12 (a) Schematic illustration for the synthetic procedure of MOF-derived hierarchical Ni/Ni$_3$S$_2$/CNFs. (b, c) SEM images of the obtained Ni/Ni$_3$S$_2$/CNFs with a high and low magnification. (d–g) High-angle annular dark-field scanning TEM image and EDX mapping of Ni/Ni$_3$S$_2$/CNFs. (h) Cyclic voltammetry curves of different electrodes at a scan rate of 5 mV s^{-1}. (i) Galvanostatic charge–discharge curves of different electrodes at a current density of 0.2 A g^{-1}. (j) The relationship between specific capacitance and current density for different electrodes. (k) Cyclic voltammetry curves of a Ni/Ni$_3$S$_2$/CNFs electrode at 50 mV s^{-1} within different potential windows. (l) Galvanostatic charge–discharge curves of Ni/Ni$_3$S$_2$/CNFs electrode at a current density of 2 A g^{-1} within different potential windows. (m) The cycling stability and Coulombic efficiency of the Ni/Ni$_3$S$_2$/CNFs-based asymmetric solid-state supercapacitor device. Reproduced with permission.[382] Copyright 2019, Royal Society of Chemistry.

and separation because of their highly efficient and selective adsorption capability, rapid equilibrium rate, and easy recyclability.[41,42,384] To enhance the adsorption performance, reduction of size, modification of functional groups, and hybridization with inorganic nanomaterials are reasonable approaches. Transition metal sulfides with nanosheet-like structures possess sulfur-rich feature and distinct 2D geome-

try, enabling them to achieve high adsorption of heavy metal ions. The integration of metal sulfides with electrospun nanofibers can not only prevent the aggregation of sulfides but also provide an easily operational recovery from the adsorption system for recyclability.[385,386] Typically, CNFs@MoS$_2$ hybrids with varied morphologies have been prepared for Hg^{2+} adsorption.[385] The CNFs are prepared from electrospun PAN/PS nano-
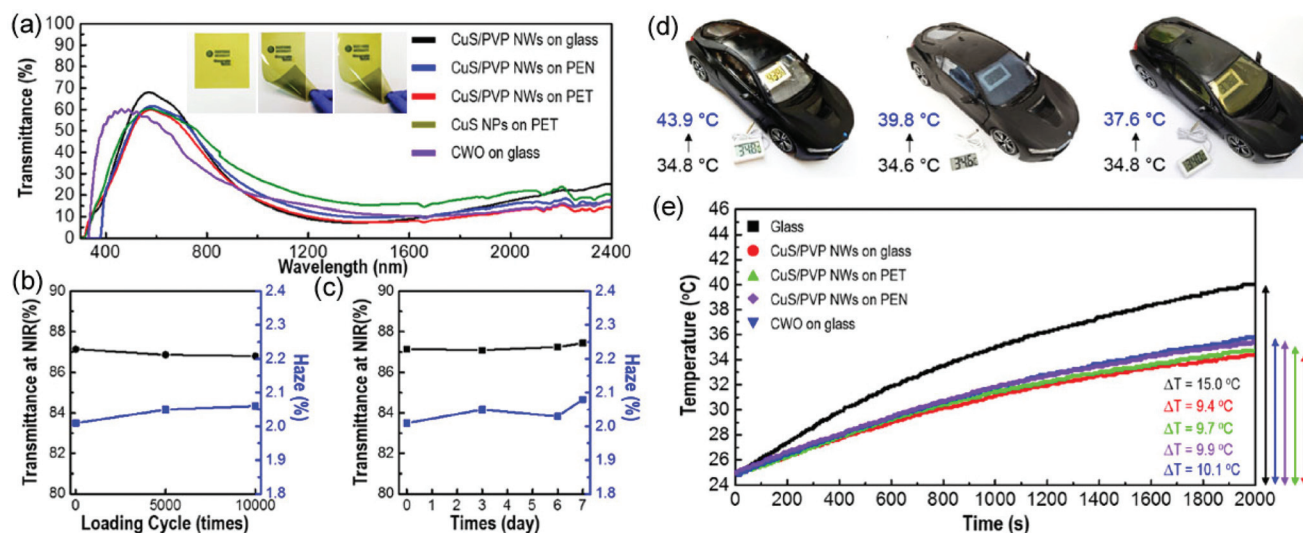
Fig. 13 (a) UV–vis transmittance of CuS NPs on PET, CWO on glass, CuS/PVP NWs on glass, PEN, and PET; the inset shows the optical properties of CuS/PVP NWs on glass, PEN, and PET. (b) Cyclic and (c) NIR shielding efficiency and haze factor of CuS/PVP NWs film testing for 1 week. (d) Monitoring of *in situ* temperature change of the thermal shielding films (from left to right: blank, commercial CWO, CuS/PVP NWs) attached on the windows of a model car. (e) Changes of the interior air temperature in a sealed box with the slide glass and typical thermal shielding films as a function of time under light irradiation of a xenon lamp. Reproduced with permission.[54] Copyright 2019, American Chemical Society.

fibers. Through tailoring the precursors and solvents under hydrothermal/solvothermal reactions, long-aligned, short-aligned, and short non-aligned MoS_2 materials are obtained on the surface of the CNFs. It was found that the CNFs@MoS_2 with a short non-aligned MoS_2 morphology possesses the largest BET surface area, which was beneficial for the adsorption performance. For the adsorption of Hg^{2+}, a largest overall removal capacity of 6258.7 mg g^{-1} MoS_2 is achieved with a kinetic equilibrium time of 24 h for CNFs@MoS_2 with a short non-aligned MoS_2 morphology, representing a huge adsorption performance. The adsorption mechanism for Hg^{2+} is attributed to the redox reactions between Hg^{2+} and MoS_2. It has been reported that the 1 T metallic phase of MoS_2 is favorable for reducing Hg^{2+} to $Hg(0)$, while with the 2H phase of MoS_2 it is difficult to achieve this objective. In this study, the CNFs@MoS_2 hybrid with short non-aligned MoS_2 exhibits a larger content of the 1 T phase of MoS_2 than the other two samples, contributing to the higher removal capacity. On the other hand, the CNFs@MoS_2 hybrid with long aligned MoS_2 enables its vertical orientation which is beneficial for rapidly reaching to interlayer sulfur sites, showing a minimum kinetic equilibrium time. Furthermore, PVP molecules with a suitable molecular weight have been utilized to tune the interlayer spacing of MoS_2, which can increase the adsorption capacity for Hg^{2+}. In addition to Hg^{2+}, MoS_2-based fibrous materials have also been prepared for Cr(VI) removal. It has been reported that conducting polymers are capable of removing Cr (VI) *via* a reduction of it into Cr(III).[387,388] Owing to a synergistic effect from electrostatic interaction, ion exchange, and redox processes, the flowerlike MoS_2@polyaniline (PANI)/PAN hybrid nanfibers display a large adsorption capacity of 6.57 mmol g^{-1} with a rapid equilibrium time of only 30 min.[389]

The integration of MoS_2 with electrospun nanofibers has also been used as efficient adsorbent for organic dyes. The MoS_2/PAN hybrid nanofibers can be prepared *via* a direct eletrospinning strategy with a precursor consisting of PAN and MoS_2 nanopetals in DMF solvent.[390] The MoS_2 nanopetals exhibit a curved thin flaky morphology, and they are most randomly encapsulated in PAN nanofibers but with partly active sites exposed. The structure of the MoS_2/PAN hybrid nanofibers enables them to be good adsorbents for RhB, achieving a maximum adsorption capacity of 77.7 mg g^{-1}, which results from the electrostatic adsorption between MoS_2 and RhB. One of the greatest advantages of MoS_2/PAN hybrid nanofibers for organic pollutant removal is their membrane characteristic with an easy recovery capability. In this study, the regeneration of the MoS_2/PAN hybrid nanofibers can be achieved with treatment with acetone. Then an excellent reutilization has been obtained, showing a removal capacity of 97.7% after thirty adsorption–desorption cycles. The excellent adsorption performance makes the hybrid nanofibers promising materials for environmental remediation.

The membrane produced from the integration of metal sulfides with electrospun nanofibers can not only show a good adsorption capability toward heavy metal ions and organic dyes, but also possesses an oil/water separation property. Generally, the modification of hierarchical metal sulfides within or on electrospun nanofibers may produce hydrophobic and oleophilic properties, which are beneficial for oil/water separation. 2D layered MoS_2 and WS_2 materials are good candidates to achieve this objective because they can promote the oil adsorption capacity and hydrophobicity of the electrospun nanofibers. As an example, poly(lactic acid) (PLA)/WS_2–MoS_2 hybrid nanofibrous membrane shows a water contact angle of
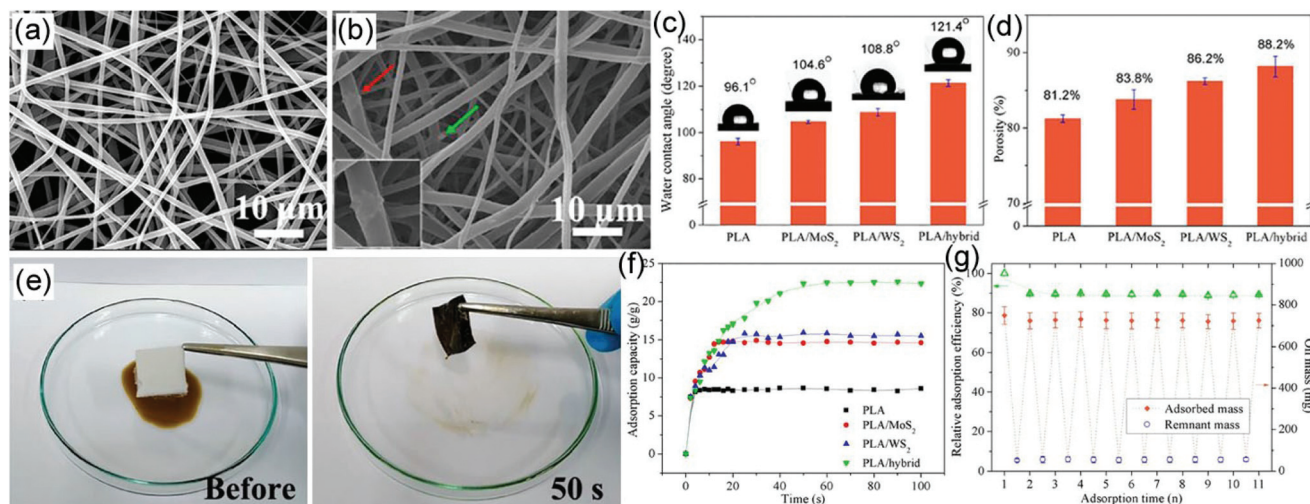
Fig. 14 (a, b) SEM images of PLA and PLA/WS$_2$/MoS$_2$ hybrid nanofibers. (c) Water contact angles and (d) porosities of PLA, PLA/MoS$_2$, PLA/WS$_2$, and PLA/WS$_2$/MoS$_2$ hybrid nanofibers. (e) Adsorption of used motor oil before and after 50 s. (f) Adsorption kinetic curves and (g) linear fitting of pseudo-second-order kinetic model by neat PLA and different hybrid nanofibers. Reproduced with permission.[391] Copyright 2019, Elsevier.

121.4°, which is larger than bare PLA (96.1°), PLA/WS$_2$ (108.8°) and PLA/MoS$_2$ (104.6°) fibrous membranes (Fig. 14a–d).[391] On the other hand, the prepared hybrid nanofibrous membrane also displays a much better oil adsorption capacity of 22.45 g g^{-1} than the other abovementioned controlled samples, which results from its abundant porous structure (Fig. 14e and f). The free-standing characteristic of this membrane provides its excellent reusability (Fig. 14g). Owing to both hydrophobic and oleophilic properties, the hybrid membrane has been utilized for oil–water separation, with a double separated oil amount compared with bare PLA nanofibrous membrane. Furthermore, for the separation of surfactant-stabilized oil/water emulsion, a separation efficiency of 94.68% has been achieved. Integrated with a high strength and Young's modulus, the hybrid nanofibrous membrane is promising for practical oily water treatment.

4.7 Biomedical applications

Electrospun nanofibers possess significant advantages for biomedical applications, including their controllable random and aligned 1D nanostructure for robust scaffolds and tunable composition to tailor their biocompatibility. Some typical metal sulfides such as MoS$_2$ nanosheets usually possess outstanding biocompatibility, benefiting stem cell growth,[392] while Cu$_x$S nanomaterials have superior photothermal capability which can be used for thermal imaging and photothermal therapy.[393,394] In this section, we will illustrate the integration of metal sulfides with electrospun nanofibers as a scaffold for promoting stem cell differentiation and photothermal therapy as well as wound healing.

In general, natural polymers such as protein-based materials manifest significant advantages for cell/tissue culture from their superior biocompatibility, compared with synthetic polymers. As a typical example, zein-based materials

have shown promising applications in biomedicine. With the integration with CdS QDs, fluorescent zein/CdS hybrid nanofibers are achieved, which have been used for the migration and proliferation of fibroblasts (L929) and stem cells (KUSA-A1).[395] Among varied types of metal sulfide, MoS$_2$ has low cytotoxicity and good conductive properties, which makes it a good candidate for neural tissue regeneration.[392] For example, MoS$_2$ nanosheets on glass slides have been prepared to be used for enhancing neural stem cell (NSC) differentiation.[396] Recently, a free-standing membrane consisting of MoS$_2$–PAN nanofibers with a varied content of MoS$_2$ has been prepared via a direct electrospinning strategy, which can promote the growth of bone marrow mesenchymal stem cells (BMSC).[397] Upon the introduction of MoS$_2$ to PAN nanofibers, promoted BMMS contact and cellular activity have been achieved, demonstrating an optimistic enhancement to tailor cellular proliferation. Furthermore, with increasing MoS$_2$ content, osteogenic differentiation of BMSCs is significantly improved. Therefore, the integration of MoS$_2$ with electrospun polymer nanofibers provides an efficient platform for tissue engineering applications.

As we have mentioned, Cu$_x$S nanomaterials possess perfect photothermal properties.[393,394] After the incorporation of Cu$_x$S nanoparticles in a polymer matrix, a tunable photothermal performance can be achieved.[398] For instance, Cu$_2$S nanoparticles have been hybridized with biopolymer fibers via a direct electrospinning route to form a Cu$_2$S–PLA/PCL nanofibrous membrane.[398] During the electrospinning process, a stainless steel mesh is employed as the collector, which produces a patterned nanofibrous membrane with a varied fiber density in different regions (Fig. 15a–e). The existing loose domain with a low density of nanofibers is beneficial for oxygen transport in favor of cell migration and ingrowth. The prepared Cu$_2$S–PLA/PCL nanofibrous membrane represents a
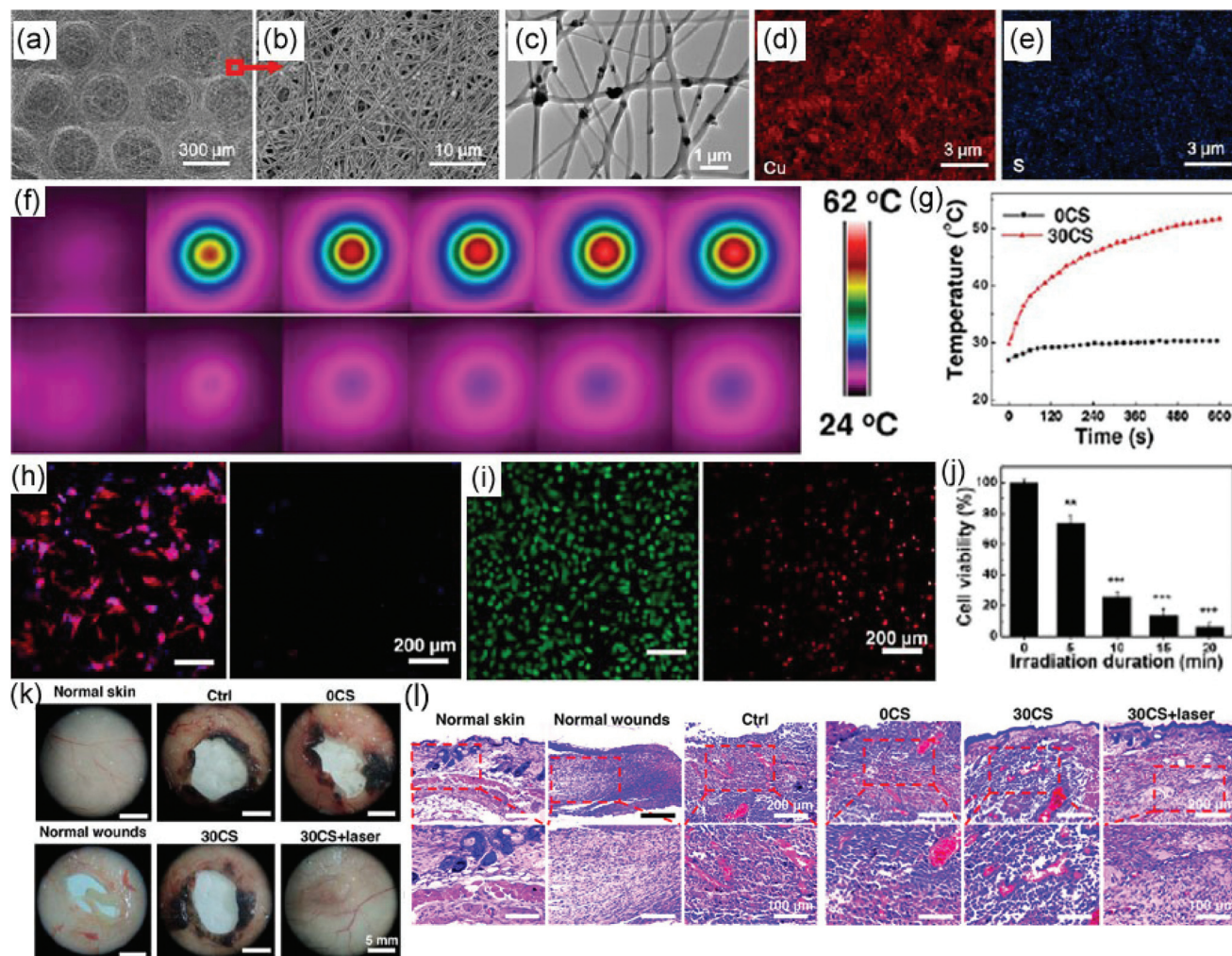
Fig. 15 (a, b) SEM images of as-prepared Cu$_2$S-PLA/PCL nanofibrous membrane with 30 wt% Cu$_2$S. (c) TEM image of Cu$_2$S-PLA/PCL nanofibers with 30 wt% Cu$_2$S. (d, e) EDS elemental mappings of Cu$_2$S-PLA/PCL nanofibers with 30 wt% Cu$_2$S (Cu in red and S in blue). (f) Real-time infrared thermal images of PLA/PCL (bottom) and Cu$_2$S-PLA/PCL nanofibrous membrane (top) in a dry environment under continuous 808 nm laser irradiation with a power density of 0.50 W cm^{-2} for different times. (g) Photothermal heating curves of PLA/PCL and Cu$_2$S–PLA/PCL nanofibrous membrane. (h) Confocal LSM (red: cytoskeleton; blue: cell nuclei) images of murine B16-F10 melanoma cells on PLA/PCL (left) and Cu$_2$S–PLA/PCL nanofibrous membrane (right) under 808 nm laser irradiation (0.50 W cm^{-2}, 15 min). (i) Live/dead staining images (green: live cells; red: dead cells) of B16-F10 melanoma cells on glass slices treated by PLA/PCL and Cu$_2$S–PLA/PCL nanofibrous membrane under 808 nm laser irradiation (0.50 W cm^{-2}, 15 min). (j) The relationship between cell viability and irradiation duration of Cu$_2$S–PLA/PCL nanofibers with 30 wt% Cu$_2$S (808 nm, 0.50 W cm^{-2}). (k) Photographs of the angiogenesis state in tumor-induced wound beds for the control, PLA/PCL, Cu$_2$S–PLA/PCL, and Cu$_2$S–PLA/PCL + laser groups as compared with normal skins and normal diabetic wounds without membranes applied on day 14. (l) H&E staining of sectioned wounds for the control, 0CS–PLA/PCL, 30CS–PLA/PCL, and 30CS–PLA/PCL + laser groups 14 days after treatments. Reproduced with permission.[398] Copyright 2017, American Chemical Society.

favorable photothermal performance under NIR irradiation, which results from collective oscillations of the holes of the Cu$_2$S nanoparticles (Fig. 15f). The fibrous membrane with 30 wt% Cu$_2$S shows an increased surface temperature from about 30 °C to 61 °C in a dry condition within 5 min, while the bare PLA/PCL fibrous membrane exhibits no change of temperature under the same environment (Fig. 15g). With increasing Cu$_2$S content, the surface temperature of the hybrid fibrous membrane increases further higher than 65 °C, which induces the part-melting of the membrane. Owing to the brilliant photothermal property, the Cu$_2$S–PLA/PCL nanofibrous

membrane represents a large anticancer efficiency toward skin tumor cells. Taking B16-F10 cells as targets, around 93.7% cell mortality is achieved from hyperthermia by Cu$_2$S–PLA/PCL nanofibrous membrane under a 808 nm laser irradiation. By contrast, most of the cells are alive on the neat PLA/PCL nanofibrous membrane (Fig. 15h–j). Furthermore, the prepared Cu$_2$S–PLA/PCL nanofibrous membrane is able to realize wound healing and skin tissue regeneration (Fig. 15k and l). With the prepared Cu$_2$S–PLA/PCL nanofibrous membrane, the relative wound area is reduced to 5.1% after 6 h, which is superior to the neat PLA/PCL membrane (18.4%), demonstrat-

ing the vital role of the Cu_2S component. The *in vitro* study demonstrates promoted migration of endothelial cells in comparison with the neat PLA/PCL membrane, confirming the improved vitro regenerative efficiency with the introduction of Cu_2S nanoparticles. The integration of Cu_2S with electrospun nanofibrous membrane provides a promising platform for tumor therapy and tissue regeneration.

5. Conclusions and future perspectives

In the last decade, large research activity has been carried out to prepare integrated metal sulfide–electrospun nanofiber hybrids including the direct encapsulation of metal sulfide nanomaterials into electrospun nanofibers and the hybridization of electrospun nanofibers *via* a post-synthesis treatment. The resultant hybrid nanofibers present fascinating optical, electronic, thermal and mechanical properties, showing a variety of applications in electronic and optoelectronic devices, sensing, catalysis, energy conversion and storage, thermal shielding, adsorption and separation, and biomedical technologies. Although a large number of metal sulfide–electrospun nanofiber hybrids have been developed for the abovementioned promising applications, considering the complexity of their chemical structures as well as the synergistic effects, some challenges still need to be addressed.

(1) The morphology and nanostructure of the functional materials have a great impact on their properties. Most of the previously reported electrospun nanofibrous materials integrated with metal sulfides are solid nanofibers with metal sulfides embedded inside the matrix or core–shell structures with metal sulfides as the shell. To promote a broad application and to enhance the performance, additional structures such as hollow nanotube, nanoparticle-in-nanotube, nanofiber-in-nanotube and multichannel structures should be developed. These nanostructures with extra void space may provide additional electrochemical active surface sites, but also contribute to the enhancement of electron and mass transport. Furthermore, the interior cavities can act as a barrier to prevent active components from aggregation, giving these nanostructured materials a superior cycling performance for applications in energy conversion and storage, for example. However, it is still a challenge to synthesize those types of complex nanostructured material with a well-controlled morphology as well as a controllable inner and outer diameter on a large scale by electrospinning.

(2) To improve the performance of electrospun nanofibers with metal sulfides in sensing, catalysis and energy conversion and storage, the control of their electronic structure and interface is desirable. Generally, doping with heteroatoms and vacancy engineering are versatile routes to modulate the electronic structures of metal sulfides and electrospun nanofibers. To tune the interface properties some distinct architectures such as core–shell, Janus, and hierarchical structures can be generated. Therefore, through the modulation of the electronic

structure and interface engineering it is expected that high-performance electrospun nanofiber–metal sulfide hybrids can be prepared for a large variety of applications.

(3) Most of the metal sulfide/electrospun nanofiber hybrid materials reported for applications in catalysis and energy conversion and storage devices are still in the form of powders. Electrospinning exhibits the distinct advantage of producing self-supporting membrane materials, which is an advantage in several applications. It is desirable to maintain the self-standing characteristic and flexibility of the membrane after post-treatments such as calcination processes and hydrothermal/solvothermal reactions. In addition, electrospun nanomaterials can be assembled into 3D superstructures. Compared with a membrane structure, the spatial effect of a 3D architecture offers an increased concentration of active sites and a superior electrolyte transport, for example.

(4) Theoretical studies should be carried out to complement the experiments, leading to an in-depth interpretation of the electronic structure and interfacial effects between the different components in hybrid nanofibers. Furthermore, advanced *in situ* spectroscopic characterization strategies such as Raman, XRD, X-ray photoelectron spectroscopy (XPS) and X-ray absorption spectroscopy (XAS) should be more routinely applied. Through the unity of theoretical and experimental studies, a deeper insight into the correlation between the structure, composition and performances of the metal sulfide-based hybrid nanofiber materials can be achieved. That would allow researchers to design and synthesize more efficient functional hybrid nanofibers with significantly improved performances.

In conclusion, electrospinning provides a general, versatile and scalable route to synthesize functional metal sulfide nanomaterials integrated with electrospun nanofibers. The principal aim of this review is to stimulate researchers to continue to focus on this research field, which will very probably allow for the production of complex electrospun nanofiber membranes for a broad range of industrial applications.

Conflicts of interest

There are no conflicts to declare.

Acknowledgements

References

1 A. P. Alivisatos, P. F. Barbara, A. W. Castleman, J. Chang, D. A. Dixon, M. L. Klein, G. L. Mclendon, J. S. Miller,

M. A. Ratner, P. J. Rossky, S. I. Stupp and M. E. Thompson, *Adv. Mater.*, 1998, **10**, 1297.

2 G. A. Ozin, *Adv. Mater.*, 1992, **4**, 612.

3 A. Thiaville and J. Miltat, *Science*, 1999, **284**, 1939.

4 C. Burda, X. Chen, R. Narayanan and M. A. El-Sayed, *Chem. Rev.*, 2005, **105**(4), 1025.

5 P. Alivisatos, *Pure Appl. Chem.*, 2000, **72**, 3.

6 A. Smith and S. M. Nie, *Acc. Chem. Res.*, 2010, **43**, 190.

7 J. M. Klostranec and W. C. W. Chan, *Adv. Mater.*, 2006, **18**, 1953.

8 P. Zrazhevskiy, M. Sena and X. Gao, *Chem. Soc. Rev.*, 2010, **39**, 4326.

9 S. Y. Lim, W. Shen and Z. Gao, *Chem. Soc. Rev.*, 2015, **44**, 362.

10 L. Chouhan, S. Ghimire, C. Subrahmanyam, T. Miyasaka and V. Biju, *Chem. Soc. Rev.*, 2020, **49**, 2869.

11 Q. Xiang, J. Yu and M. Jaroniec, *Chem. Soc. Rev.*, 2012, **41**, 782.

12 Z. Hu, Z. Wu, C. Han, J. He, Z. Nie and W. Chen, *Chem. Soc. Rev.*, 2018, **47**, 3100.

13 E. Z. Shi, Y. Gao, B. P. Finkenauer, Akriti, A. H. Coffey and L. T. Dou, *Chem. Soc. Rev.*, 2018, **47**, 6046.

14 X. Gao, H. B. Liu, D. Wang and J. Zhang, *Chem. Soc. Rev.*, 2019, **48**, 908.

15 Z. H. Fu, N. Wang, D. Legut, C. Si, Q. F. Zhang, S. Y. Du, T. C. Germann, J. S. Francisco and R. R. Zhang, *Chem. Rev.*, 2019, **119**, 11980.

16 R. Kempt, A. Kuc and T. Heine, *Angew. Chem., Int. Ed.*, 2020, **59**, 9242.

17 R. R. Liang, S. Y. Jiang, A. Ru-Han and X. Zhao, *Chem. Soc. Rev.*, 2020, **49**, 3920.

18 R. D. Farahani, M. Dube and D. Therriault, *Adv. Mater.*, 2016, **28**, 5794.

19 J. H. Moon and S. Yang, *Chem. Rev.*, 2010, **110**, 547.

20 T. Xu, Y. C. Ding, Z. P. Liang, H. L. Sun, F. Zheng, Z. T. Zhu, Y. Zhao and H. Fong, *Prog. Polym. Sci.*, 2020, **112**, 100656.

21 X. Wang, B. Ding, G. Sun, M. R. Wang and J. Yu, *Prog. Mater. Sci.*, 2013, **58**, 1173.

22 Y. Xia, P. Yang, Y. Sun, Y. Wu, B. Mayers, B. Gates, Y. Yin, F. Kim and H. Yan, *Adv. Mater.*, 2002, **15**, 353.

23 E. Barrigón, M. Heurlin, Z. Bi, B. Monemar and L. Samuelson, *Chem. Rev.*, 2019, **119**, 9170.

24 T. Zhai, L. Li, Y. Ma, M. Liao, X. Wang, X. Fang, J. Yao, Y. Bando and D. Golberg, *Chem. Soc. Rev.*, 2011, **40**, 2986.

25 D. Huo, M. J. Kim, Z. Lyu, Y. Shi, B. J. Wiley and Y. Xia, *Chem. Rev.*, 2019, **119**, 11980.

26 L. Mai, X. Tian, X. Xu, L. Chang and L. Xu, *Chem. Rev.*, 2014, **114**, 11828.

27 X. Lu, W. Zhang, C. Wang, T. C. Wen and Y. Wei, *Prog. Polym. Sci.*, 2011, **36**, 671.

28 H. W. Liang, S. Liu and S. H. Yu, *Adv. Mater.*, 2010, **22**, 3925.

29 J. Ye and L. Qi, *J. Mater. Sci. Technol.*, 2008, **24**, 529.

30 F. Wang, A. Dong and W. E. Buhro, *Chem. Rev.*, 2016, **116**, 10888.

31 Y. Zhang, L. Heng and L. Jiang, *J. Nanosci. Nanotechnol.*, 2014, **14**, 5597.

32 L. Chen and B. Su, *Chem. Soc. Rev.*, 2019, **48**, 8.

33 Z. Huang, Y. Zhang, M. Kotaki and S. Ramakrishna, *Compos. Sci. Technol.*, 2003, **63**, 2223.

34 D. Li and Y. Xia, *Adv. Mater.*, 2004, **16**, 1151.

35 A. Greiner and J. H. Wendorff, *Angew. Chem., Int. Ed.*, 2007, **46**, 5670.

36 H. Wang, S. Yuan, D. Ma, X. Zhang and J. Yan, *Energy Environ. Sci.*, 2015, **8**, 1660.

37 J. Xue, T. Wu, Y. Dai and Y. Xia, *Chem. Rev.*, 2019, **119**, 5298.

38 C. L. Zhang and S. H. Yu, *Chem. Soc. Rev.*, 2014, **43**, 4423.

39 S. Peng, G. Jin, L. Li, K. Li, M. Srinivasan, S. Ramakrishna and J. Chen, *Chem. Soc. Rev.*, 2016, **45**, 1225.

40 L. Hou, N. Wang, J. Wu, Z. Cui, L. Jiang and Y. Zhao, *Adv. Funct. Mater.*, 2018, **28**, 1.

41 J. Zhang, L. Liu, Y. Si, J. Yu and B. Ding, *Adv. Funct. Mater.*, 2020, **30**, 2002192.

42 X. Lu, M. Li, H. Wang and C. Wang, *Inorg. Chem. Front.*, 2019, **6**, 3012.

43 X. He, J. Zheng, G. Yu, M. You, M. Yu, X. Ning and Y. Long, *J. Phys. Chem. C*, 2017, **121**, 8663.

44 Y. Sun, S. Cheng, W. Lu, Y. Wang, P. Zhang and Q. Yao, *RSC Adv.*, 2019, **9**, 25712.

45 D. Lv, M. Zhu, Z. Jiang, S. Jiang, Q. Zhang, R. Xiong and C. Huang, *Macromol. Mater. Eng.*, 2018, **303**, 1.

46 L. Rayleigh, *Philos. Mag.*, 1882, **14**, 184.

47 X. Lu, C. Wang and Y. Wei, *Small*, 2009, **5**, 2349.

48 C. H. Lai, M. Y. Lu and L. J. Chen, *J. Mater. Chem.*, 2012, **22**, 19.

49 X. Rui, H. Tan and Q. Yan, *Nanoscale*, 2014, **6**, 9889.

50 M. R. Harrison and M. G. Francesconi, *Coord. Chem. Rev.*, 2011, **255**, 451.

51 F. Zhang and S. S. Wong, *Chem. Mater.*, 2009, **94**, 2251.

52 P. Kulkarni, S. K. Nataraj, R. G. Balakrishna, D. H. Nagaraju and M. V. Reddy, *J. Mater. Chem. A*, 2017, **5**, 22040.

53 W. Song, M. X. Li, C. Wang and X. F. Lu, *Carbon Energy*, 2021, **3**, 101.

54 Y. T. Kwon, S. H. Ryu, J. W. Shin, W. H. Yeo and Y. H. Choa, *ACS Appl. Mater. Interfaces*, 2019, **11**, 6575.

55 X. Lu, L. Li, W. Zhang and C. Wang, *Nanotechnology*, 2005, **16**, 2233.

56 R. Afeesh, N. A. M. Barakat, S. S. Al-deyab, A. Yousef and H. Yong, *Colloids Surf., A*, 2012, **409**, 21.

57 G. Yu, X. Li, X. Cai, W. Cui, S. Zhou and J. Weng, *Acta Mater.*, 2008, **56**, 5775.

58 T. P. Mthethwa, M. J. Moloto, A. De Vries and K. P. Matabola, *Mater. Res. Bull.*, 2011, **46**, 569.

59 G. Panthi, N. A. M. Barakat, K. Abdelrazek, A. Yousef, K. Jeon and H. Yong, *Ceram. Int.*, 2013, **39**, 1469.

60 M. Bashouti, W. Salalha and M. Brumer, *ChemPhysChem*, 2006, **7**, 102.

61 L. Persano, A. Camposeo, F. Di Benedetto, R. Stabile, A. M. Laera, E. Piscopiello, L. Tapfer and D. Pisignano, *Adv. Mater.*, 2012, **24**, 5320.

62 X. Lu, Y. Zhao and C. Wang, *Adv. Mater.*, 2005, **17**, 2485.

63 X. Lu, Y. Zhao, C. Wang and Y. Wei, *Macromol. Rapid Commun.*, 2005, **26**, 1325.

64 J. Xu, X. Cui, J. Zhang, H. Liang, H. Wang and J. Li, *Bull. Mater. Sci.*, 2008, **31**, 189.

65 H. Wang, Y. Yang, X. Lu and C. Wang, *Chem. J. Chin. Univ.*, 2006, **27**, 1785.

66 C. Su, J. Liu, C. Shao and Y. Liu, *J. Non-Cryst. Solids*, 2011, **357**, 1488.

67 F. Di Benedetto, A. Camposeo, L. Persano, A. M. Laera, E. Piscopiello, R. Cingolani, L. Tapfer and D. Pisignano, *Nanoscale*, 2011, **3**, 4234.

68 C. Wang, E. Yan, Z. Sun, Z. Jiang, Y. Tong, Y. Xin and Z. Huang, *Macromol. Mater. Eng.*, 2007, **292**, 949.

69 C. Wang, E. Yan, G. Li, Z. Sun, S. Wang, Y. Tong, W. Li, Y. Xin, Z. Huang and P. Yan, *Synth. Met.*, 2010, **160**, 1382.

70 J. Ye, Y. Chen, W. Zhou, X. Wang, Z. Guo and Y. Hu, *Mater. Lett.*, 2009, **63**, 1425.

71 C. Q. Zhang, J. Sun, W. Wang, Q. B. Yang, Y. X. Li and J. S. Du, *Chem. Res. Chin. Univ.*, 2012, **28**, 534.

72 X. Lu, H. Mao, W. Zhang and C. Wang, *Mater. Lett.*, 2007, **61**, 2288.

73 Z. Zhou, D. He, W. Xu, F. Ren and Y. Qian, *Mater. Lett.*, 2007, **61**, 4500.

74 S. Gao, G. Chen, Y. Dall'Agnese, Y. Wei, Z. Gao and Y. Gao, *Chem. – Eur. J.*, 2018, **24**, 13535.

75 S. Zaidi, C. Wang, Y. Jin, S. Zhu, H. Yuan, Y. Yang and J. Chen, *J. Alloys Compd.*, 2020, **848**, 156531.

76 C. Su, C. Shao and Y. Liu, *J. Colloid Interface Sci.*, 2010, **346**, 324.

77 Y. Yang, H. Wang, X. Lu, Y. Zhao and X. Li, *Mater. Sci. Eng., B*, 2007, **140**, 48.

78 H. Cao, Y. Zhu, X. Tan, H. Kang, X. Yang and C. Li, *New J. Chem.*, 2010, **34**, 1116.

79 D. Li and C. Pan, *Prog. Nat. Sci.: Mater. Int.*, 2012, **22**, 59.

80 Z. Li, Z. Ma, X. Zhang, Q. Du, Y. Fu, L. Shuang, K. Yang, L. Li, W. Lai and W. Zhang, *J. Alloys Compd.*, 2021, **850**, 156807.

81 Z. Zhang, K. Tan, Y. Gong, H. Wang, R. Wang, L. Zhao and B. He, *J. Power Sources*, 2019, **437**, 226908.

82 S. Yao, C. Zhang, R. Guo, A. Majeed, Y. He, Y. Wang, X. Shen, T. Li and S. Qin, *ACS Sustainable Chem. Eng.*, 2020, **8**, 13600.

83 Z. Ma, Z. Sun, H. Jiang, F. Li, Q. Wang and F. Qu, *Appl. Surf. Sci.*, 2020, **533**, 147521.

84 I. Grozdanov and M. Najdoski, *J. Solid State Chem.*, 1995, **114**, 469.

85 A. Chatterjee, A. Priyam, S. K. Das and A. Saha, *J. Colloid Interface Sci.*, 2006, **294**, 334.

86 H. Tang, L. N. Sacco, S. Vollebregt, H. Ye, X. Fan and G. Zhang, *J. Mater. Chem. A*, 2020, **8**, 24943.

87 G. M. Tomboc, B. T. Gadisa, J. Joo, H. Kim and K. Lee, *ChemNanoMat*, 2020, **6**, 850.

88 Z. Cheng, S. Zhao, L. Kang, M. Li and Z. Gao, *Mater. Lett.*, 2018, **214**, 80.

89 G. Hou, Z. Cheng, L. Kang, X. Xu, F. Zhang and H. Yang, *CrystEngComm*, 2015, **17**, 5496.

90 Y. Ma, P. Lv, F. Duan, J. Sheng, S. Lu, H. Zhu, M. Du and M. Chen, *J. Alloys Compd.*, 2020, **834**, 155158.

91 T. Abitbol, J. T. Wilson and D. G. Gray, *J. Appl. Polym. Sci.*, 2010, **119**, 803.

92 L. Chen, C. Lee, Y. Chuang, Z. Wu and C. Chen, *CrystEngComm*, 2015, **17**, 4434.

93 A. Alam, Z. Khan, N. A. M. Barakat, P. Singh, M. Park and H. Yong, *Polymer*, 2016, **85**, 89.

94 Y. Alt, N. B. Kiremitler, S. Genç and M. S. Onses, *J. Phys. D: Appl. Phys.*, 2018, **51**, 065111.

95 D. Hernández-martínez, M. E. Nicho, H. Hu, U. León-silva and M. C. Arenas-arrocena, *Mater. Sci. Semicond. Process.*, 2017, **61**, 50.

96 R. Wei, X. Tian, Z. Hu, H. Zhang, T. Qiao, X. He, Q. Chen, Z. Chen and J. Qiu, *Opt. Express*, 2016, **24**, 25337.

97 L. Zhu, M. Gao, C. K. N. Peh and G. W. Ho, *Mater. Horiz.*, 2018, **5**, 323.

98 W. Yang, Y. Li, L. Feng, Y. Hou, S. Wang, B. Yang, X. Hu, W. Zhang and S. Ramakrishna, *Int. J. Mol. Sci.*, 2020, **21**, 4224.

99 M. Lu, L. Chen, W. Mai and Z. L. Wang, *Appl. Phys. Lett.*, 2008, **93**, 242503.

100 R. Nirmala, K. Jeon, R. Navamathavan, B. Kim, M. Khil and H. Yong, *J. Colloid Interface Sci.*, 2013, **397**, 65.

101 I. E. Moreno-cortez, A. Alvarado-castañeda and D. F. Garcia-gutierrez, *Synth. Met.*, 2016, **220**, 255.

102 Z. L. Wang, G. Zhu, Y. Yang, S. Wang and C. Pan, *Mater. Today*, 2012, **15**, 532.

103 K. Maity, B. Mahanty, T. K. Sinha, S. Garain, A. Biswas, S. K. Ghosh, S. Manna, S. K. Ray and D. Mandal, *Energy Technol.*, 2017, **5**, 234.

104 P. Sahatiya, S. Kannan and S. Badhulika, *Appl. Mater. Today*, 2018, **13**, 91.

105 A. Sultana, M. M. Alam, A. Biswas, T. R. Middya and D. Mandal, *Transl. Mater. Res.*, 2016, **3**, 045001.

106 V. N. Nguyen, M. T. Doan and M. V. Nguyen, *J. Mater. Sci.: Mater. Electron.*, 2019, **30**, 926.

107 Z. Zhang, X. Li, C. Gao, F. Teng, Y. Wang, L. Chen, W. Han, Z. Zhang and E. Xie, *J. Mater. Chem. A*, 2015, **3**, 12769.

108 W. Fan, M. Li, H. Bai, D. Xu, C. Chen, C. Li, Y. Ge and W. Shi, *Langmuir*, 2016, **32**, 1629.

109 W. Fei, H. Li, N. Li, D. Chen, Q. Xu, H. Li, J. He and J. Lu, *Sol. Energy*, 2020, **199**, 164.

110 H. N. Hieu, N. V. Nghia, N. M. Vuong and H. Van Bui, *Chem. Commun.*, 2020, **56**, 3975.

111 M. Shneider, H. Dodiuk, S. Kenig and R. Tenne, *J. Adhes. Sci. Technol.*, 2010, **24**, 1083.

112 C. S. Reddy, A. Zak and E. Zussman, *J. Mater. Chem.*, 2011, **21**, 16086.

113 H. Zheng, X. Lei, T. Cheng, S. Liu, X. Zeng and R. Sun, *Nanotechnology*, 2017, **28**, 265204.

114 N. Kim, W. Na, W. Yin, H. Jin, T. K. Ahn, S. M. Cho and H. Chae, *J. Mater. Chem. C*, 2016, **4**, 2457.

115 G. J. Supran, Y. Shirasaki, K. W. Song, J. M. Caruge, P. T. Kazlas, S. Coe-Sullivan, T. L. Andrew, M. G. Bawendi and V. Bulović, *MRS Bull.*, 2013, **38**, 703.

116 C. Canetta, S. Guo and A. Narayanaswamy, *Rev. Sci. Instrum.*, 2014, **85**, 104901.

117 D. N. Ortiz, J. Vedrine, N. J. Pinto, C. H. Naylor and A. T. Charlie Johnson, *Mater. Sci. Eng., B*, 2016, **214**, 68.

118 B. G. Lewis and D. C. Paine, *MRS Bull.*, 2000, **25**, 22.

119 X. Zhang, W. Guo, G. Gao, M. Que, C. Pan and Z. L. Wang, *J. Mater. Chem. C*, 2016, **4**, 4733.

120 J. Hu, L. S. Li, W. Yang, L. Manna, L. W. Wang and A. P. Alivisatos, *Science*, 2001, **292**, 2060.

121 K. E. Roskov, K. A. Kozek, W. C. Wu, R. K. Chhetri, A. L. Oldenburg, R. J. Spontak and J. B. Tracy, *Langmuir*, 2011, **27**, 13965.

122 T. Aubert, L. Palangetic, M. Mohammadimasoudi, K. Neyts, J. Beeckman, C. Clasen and Z. Hens, *ACS Photonics*, 2015, **2**, 583.

123 S. Chen, C. Teng, M. Zhang, Y. Li, D. Xie and G. Shi, *Adv. Mater.*, 2016, **28**, 5969.

124 G. Konstantatos and E. H. Sargent, *Nat. Nanotechnol.*, 2010, **5**, 391.

125 Z. Zheng, L. Gan, J. B. Zhang, F. Zhuge and T. Y. Zhai, *Adv. Sci.*, 2017, **4**, 1600316.

126 M. N. Tahir, N. Zink, M. Eberhardt, H. A. Therese, U. Kolb, P. Theato and W. Tremel, *Angew. Chem., Int. Ed.*, 2006, **45**, 4809.

127 Y. Zhang, H. Zou, J. Peng, Z. Duan, M. Ma, X. Xin, W. Li and X. Zheng, *Sens. Actuators, B*, 2018, **272**, 459.

128 X. Y. Huang, Z. T. Chi, J. Liu, D. H. Li, X. J. Sun, C. Yan, Y. C. Wang, H. Li, X. D. Wang and W. F. Xie, *Sens. Actuators, B*, 2020, **304**, 127305.

129 J. Cha, S. Choi and I. Kim, *J. Mater. Chem. A*, 2017, **5**, 8725.

130 D. Youn, B. Kim and S. J. Yun, *Nanotechnology*, 2020, **31**, 105602.

131 S. Hou, R. Pang, S. Chang, L. Ye, J. Xu, X. Wang, Y. Zhang, Y. Shang and A. Cao, *ACS Appl. Mater. Interfaces*, 2020, **12**, 29778.

132 F. Wang, H. Liu, K. Hu, Y. Li, W. Zeng and L. Zeng, *Ceram. Int.*, 2019, **45**, 22981.

133 A. D. S. Luis, Z. Aguirreurreta, L. M. Pardo, A. Perez-marquez and J. Maudes, *Isr. J. Chem.*, 2018, **58**, 1347.

134 R. Tatavarty, E. Taek, J. Park, J. Kwak, J. Lee and M. Bock, *React. Funct. Polym.*, 2011, **71**, 104.

135 C. Meng, Y. Xiao, P. Wang, L. Zhang, Y. Liu and L. Tong, *Adv. Mater.*, 2011, **23**, 3770.

136 M. Wu, C. Lin, T. Lin, S. Chan, Y. Chang, T. Lin, Z. Zhou, K. Wang and C. Lai, *ACS Appl. Mater. Interfaces*, 2019, **11**, 34454.

137 M. Wu, C. Kao, T. Lin, S. Chan, S. Chen, C. Lin, Y. Huang, Z. Zhou, K. Wang and C. Lai, *Sens. Actuators, B*, 2020, **309**, 127760.

138 Z. Wu, H. Duan, Z. Li, J. Guo, F. Zhong and Y. Cao, *Sensors*, 2017, **17**, 2676.

139 J. Guo, Y. Wu, P. Wei, Y. Huang and J. Chen, *Dyes Pigm.*, 2018, **159**, 198.

140 A. Baranowska-korczyc, K. Sobczak, P. Dłuz and A. Reszka, *Phys. Chem. Chem. Phys.*, 2015, **17**, 24029.

141 J. Wang, *Chem. Rev.*, 2008, **108**, 814.

142 H. Y. Yue, P. F. Wu, S. Huang, X. Gao, S. S. Song, W. Q. Wang, H. J. Zhang and X. R. Guo, *J. Electroanal. Chem.*, 2019, **833**, 427.

143 Q. Guo, T. Wu, L. Liu, Y. He, D. Liu and T. You, *J. Alloys Compd.*, 2020, **819**, 153376.

144 K. Rajendran, T. Kokulnathan, S. M. Chen, J. A. Allen, C. Viswanathan and H. A. Therese, *Microchim. Acta*, 2019, **186**, 141.

145 Q. Mei, Y. Ding, L. Li, A. Wang, D. Duan and Y. Zhao, *J. Electroanal. Chem.*, 2019, **833**, 297.

146 X. Lu, X. Bian, G. Nie, C. Zhang, C. Wang and Y. Wei, *J. Mater. Chem.*, 2012, **22**, 12723.

147 W. Sun, X. Lu, Y. Tong, J. Lei, G. Nie and C. Wang, *J. Mater. Chem. A*, 2014, **2**, 6740.

148 Y. Tong, X. Lu, W. Sun, G. Nie, L. Yang and C. Wang, *J. Power Sources*, 2014, **261**, 221.

149 S. Chen, S. Qiu, M. Zhong, D. Tian, C. Wang and X. Lu, *Appl. Organomet. Chem.*, 2019, **33**, e5253.

150 A. M. Al-Enizi, A. Nafady, M. M. El-Halwany, R. M. Brooks, A. Abutaleb and A. Yousef, *Int. J. Hydrogen Energy*, 2019, **44**, 21716.

151 G. Nie, Z. Li, X. Lu, J. Lei, C. Zhang and C. Wang, *Appl. Surf. Sci.*, 2013, **284**, 595.

152 Y. Lu, Y. Wang, S. Cui, W. Chen and L. Mi, *RSC Adv.*, 2018, **8**, 40589.

153 X. Zhang, J. Mei, S. Wang, Y. Zheng, C. Cui, J. Pan and C. Li, *J. Mater. Sci.: Mater. Electron.*, 2017, **28**, 4669.

154 Y. Li, Z. Wang, H. Zhao, X. Huang and M. Yang, *J. Colloid Interface Sci.*, 2019, **557**, 709.

155 Q. Wang, Y. Chen, R. Liu, H. Liu and Z. Li, *Composites, Part A*, 2012, **43**, 1869.

156 Z. G. Zhang, H. Liu, Y. Q. Cui, M. Dong, Q. H. Li, X. X. Wang, S. Ramakrishna and Y. Z. Long, *Nanoscale Res. Lett.*, 2019, **14**, 215.

157 U. T. D. Thuy, I. Borisova, O. Stoilova, I. Rashkov and N. Q. Liem, *Catal. Lett.*, 2018, **148**, 2756.

158 G. Panthi, N. A. M. Barakat, M. Park, H. Y. Kim and S. J. Park, *J. Ind. Eng. Chem.*, 2015, **21**, 298.

159 W. J. Fan, Z. F. Zhou, W. B. Xu, Z. F. Shi, F. M. Ren, H. H. Ma and S. W. Huang, *Int. J. Hydrogen Energy*, 2010, **35**, 6525.

160 S. Peng, P. Zhu, S. G. Mhaisalkar and S. Ramakrishna, *J. Phys. Chem. C*, 2012, **116**, 13849.

161 T. He, H. Ma, Z. Zhou, W. Xu, F. Ren, Z. Shi and J. Wang, *Polym. Degrad. Stab.*, 2009, **94**, 2251.

162 T. He, Z. Zhou, W. Xu, Y. Cao, Z. Shi and W. P. Pan, *Compos. Sci. Technol.*, 2010, **70**, 1469.

163 Q. Zhang, G. Li, J. Bai, R. He and C. Li, *Mater. Res. Bull.*, 2019, **117**, 9.

164 F. Zhou, Z. Zhang, J. Wang, S. Huang, J. Liu, Y. Li, Q. Wang and W. Liu, *Nanotechnology*, 2020, **31**, 375606.

165 Q. Liu, J. Li, Y. Zhao, Y. Zhou and C. Li, *Mater. Lett.*, 2015, **138**, 89.

166 C. S. Ho, N. H. Z. Abidin, M. W. Nugraha, N. S. Sambudi, F. Ali, M. D. H. Wirzal, L. D. Kasmiarno and S. A. Adli, *Fibers Polym.*, 2020, **21**, 1212.

167 A. R. Unnithan, N. A. M. Barakat, M. F. Abadir, A. Yousef and H. Y. Kim, *J. Mol. Catal. A: Chem.*, 2012, **186**, 363–364.

168 H. M. Zhengfa Zhou, Y. Feng, W. Xu and F. Ren, *J. Appl. Polym. Sci.*, 2009, **113**, 1264.

169 H. A. M. Ardoña, F. U. Paredes, I. H. J. Arellano and S. D. Arco, *Mater. Lett.*, 2013, **91**, 96.

170 J. Li, J. Cao, X. Zhang, S. Wang, Y. Zheng, J. Pan and C. Li, *J. Mater. Sci.: Mater. Electron.*, 2016, **27**, 1479.

171 P. Y. Lin, Z. S. Wu, Y. Der Juang, Y. S. Fu and T. F. Guo, *Microelectron. Eng.*, 2016, **149**, 73.

172 F. Ren, H. Ma, W. Hu, Z. Zhou and W. Xu, *J. Appl. Polym. Sci.*, 2015, **132**, 2.

173 Y. Luo, Y. Jia, D. Zhang and X. Cheng, *Photochem. Photobiol.*, 2016, **92**, 515.

174 H. Wang, L. Liang, X. Cheng, Y. Luo and S. Sun, *Photochem. Photobiol.*, 2018, **94**, 17.

175 J. Pan, J. Li, X. Zhang, Y. Zheng, C. Cui, Z. Zhu and C. Li, *J. Phys. D: Appl. Phys.*, 2016, **49**, 285105.

176 H. Chen, G. Jiang, W. Yu, D. Liu, Y. Liu, L. Li, Q. Huang, Z. Tong and W. Chen, *Powder Technol.*, 2016, **298**, 1.

177 X. Xu, W. Liu, Y. Kim and J. Cho, *Nano Today*, 2014, **9**, 604.

178 H. Deng, F. Xu, B. Cheng, J. Yu and W. Ho, *Nanoscale*, 2020, **12**, 7206.

179 H. Liang, J. Bai, T. Xu and C. Li, *Vacuum*, 2020, **172**, 109059.

180 Y. Wang, J. Sunarso, F. Wang, B. Zhao, X. Liu and G. Chen, *Ceram. Int.*, 2017, **43**, 11028.

181 J. Guo, M. Guo, D. Jia, X. Song and F. Tong, *Chem. Phys. Lett.*, 2016, **659**, 66.

182 B. Pant, N. A. M. Barakat, H. R. Pant, M. Park, P. S. Saud, J. W. Kim and H. Y. Kim, *J. Colloid Interface Sci.*, 2014, **434**, 159.

183 Z. Wei, Y. Li, S. Luo, C. Liu, D. Meng, M. Ding and G. Zeng, *Sep. Purif. Technol.*, 2014, **122**, 60.

184 Y. Liu, M. Zhang, L. Li and X. Zhang, *Catal. Commun.*, 2015, **60**, 23.

185 M. M. Sabzehmeidani, H. Karimi and M. Ghaedi, *Polyhedron*, 2019, **170**, 160.

186 Z. Zhang, C. Shao, X. Li, Y. Sun, M. Zhang, J. Mu, P. Zhang, Z. Guo and Y. Liu, *Nanoscale*, 2013, **5**, 606.

187 S. Ghafoor, S. Ata, N. Mahmood and S. N. Arshad, *Sci. Rep.*, 2017, **7**, 1.

188 Z. Shami and N. Sharifi-Sanjani, *CrystEngComm*, 2014, **16**, 910.

189 D. Lin, H. Wu, R. Zhang, W. Zhang and W. Panw, *J. Am. Ceram. Soc.*, 2010, **93**, 3384.

190 K. S. Ranjith, A. Senthamizhan, B. Balusamy and T. Uyar, *Catal. Sci. Technol.*, 2017, **7**, 1167.

191 S. Pu, D. Long, M. Q. Wang, S. J. Bao, Z. Liu, F. Yang, H. Wang and Y. Zeng, *Mater. Lett.*, 2017, **209**, 56.

192 B. Ren, W. Shen, L. Li, S. Wu and W. Wang, *Appl. Surf. Sci.*, 2018, **447**, 711.

193 M. J. Chang, W. N. Cui, J. Liu, K. Wang, H. L. Du, L. Qiu, S. M. Fan and Z. M. Luo, *J. Mater. Sci. Technol.*, 2020, **36**, 97.

194 B. Pant, M. Park and S. J. Park, *Inorg. Chem. Commun.*, 2019, **102**, 113.

195 N. Qin, J. Xiong, R. Liang, Y. Liu, S. Zhang, Y. Li, Z. Li and L. Wu, *Appl. Catal., B*, 2017, **202**, 374.

196 Y. Li, P. Zhang, D. Wan, C. Xue, J. Zhao and G. Shao, *Appl. Surf. Sci.*, 2020, **504**, 144361.

197 C. Liu, L. Wang, Y. Tang, S. Luo, Y. Liu, S. Zhang, Y. Zeng and Y. Xu, *Appl. Catal., B*, 2015, **164**, 1.

198 W. Ou, J. Pan, Y. Liu, S. Li, H. Li, W. Zhao, J. Wang, C. Song, Y. Zheng and C. Li, *J. Energy Chem.*, 2020, **43**, 188.

199 B. Pant, H. R. Pant, M. Park, Y. Liu, J. W. Choi, N. A. M. Barakat and H. Y. Kim, *Catal. Commun.*, 2014, **50**, 63.

200 C. Su, C. Shao and Y. Liu, *J. Colloid Interface Sci.*, 2011, **359**, 220.

201 N. Qin, Y. Liu, W. Wu, L. Shen, X. Chen, Z. Li and L. Wu, *Langmuir*, 2015, **31**, 1203.

202 Y. Liu, F. Gao, L. Wang, W. Yang, X. He and H. Hou, *J. Mater. Sci.: Mater. Electron.*, 2019, **30**, 1487.

203 X. Li, D. Baiyila, X. Wang, X. Li, B. Sharileaodu, L. Xu, Z. Liu, L. Duan and J. Liu, *J. Mater. Chem. A*, 2014, **2**, 12304.

204 G. Yang, Q. Zhang, W. Chang and W. Yan, *J. Alloys Compd.*, 2013, **580**, 29.

205 X. Li, X. Chen, H. Niu, X. Han, T. Zhang, J. Liu, H. Lin and F. Qu, *J. Colloid Interface Sci.*, 2015, **452**, 89.

206 C. Feng, L. Zhang and Z. Cheng, *ChemistrySelect*, 2020, **5**, 2142.

207 F. Tian, D. Hou, F. Hu, K. Xie, X. Qiao and D. Li, *Appl. Surf. Sci.*, 2017, **391**, 295.

208 N. Singh, K. Mondal, M. Misra, A. Sharma and R. K. Gupta, *RSC Adv.*, 2016, **6**, 48109.

209 G. Yang, W. Yan, Q. Zhang, S. Shen and S. Ding, *Nanoscale*, 2013, **5**, 12432.

210 A. M. Al-enizi, M. M. El-Halwany, M. A. Al-abdrabalnabi, M. Baker, M. Ubaidullah and A. Yousef, *Catalysts*, 2020, **10**, 417.

211 J. Liu, L. Qiu, M. J. Chang, B. Yuan, M. Sun, S. M. Fan, W. N. Cui, Q. Hui, F. R. Ni, M. Y. Li, Y. Q. Li and Z. M. Luo, *Mater. Chem. Phys.*, 2020, **247**, 122858.

212 B. Pant, H. R. Pant, N. A. M. Barakat, M. Park, T. H. Han, B. H. Lim and H. Y. Kim, *Ceram. Int.*, 2014, **40**, 1553.

213 F. Zhang, C. L. Zhang, W. N. Wang, H. P. Cong and H. S. Qian, *ChemSusChem*, 2016, **9**, 1449.

214 W. Wang, F. Zhang, C. Zhang, Y. Wang, W. Tao, S. Cheng and H. Qian, *Chin. J. Catal.*, 2017, **38**, 1851.

215 F. Zhang, L. N. Hao, Y. Wang, S. Cheng, W. N. Wang, C. L. Zhang, F. Xu and H. S. Qian, *CrystEngComm*, 2016, **18**, 6013.

216 X. Zhang, C. Shao, X. Li, N. Lu, K. Wang, F. Miao and Y. Liu, *J. Hazard. Mater.*, 2015, **283**, 599.

217 Q. Yu, J. Xu, W. Wang and C. Lu, *Mater. Res. Bull.*, 2014, **51**, 40.

218 F. Xu, L. Zhang, B. Cheng and J. Yu, *ACS Sustainable Chem. Eng.*, 2018, **6**, 12291.

219 J. Pan, C. Chi, M. You, Z. Jiang, W. Zhao, M. Zhu, C. Song, Y. Zheng and C. Li, *Mater. Lett.*, 2018, **227**, 205.

220 J. Zhao, P. Zhang, J. Fan, J. Hu and G. Shao, *Appl. Surf. Sci.*, 2018, **430**, 466.

221 J. Wu, X. Wang, Q. Wang, Z. Lou, S. Li, Y. Zhu, L. Qin and H. Wei, *Chem. Soc. Rev.*, 2019, **48**, 1004.

222 W. Song, B. Zhao, C. Wang, Y. Ozaki and X. Lu, *J. Mater. Chem. B*, 2019, **7**, 850.

223 L. Gao, J. Zhuang, L. Nie, J. Zhang, Y. Zhang, N. Gu, T. Wang, J. Feng, D. Yang, S. Perrett and X. Yan, *Nat. Nanotechnol.*, 2007, **2**, 577–583.

224 Y. Jiang, N. Song, C. Wang, N. Pinna and X. Lu, *J. Mater. Chem. B*, 2017, **5**, 5499.

225 M. Chi, S. Chen, M. Zhong, C. Wang and X. Lu, *Chem. Commun.*, 2018, **54**, 5827.

226 Y. Zhu, Z. Yang, M. Chi, M. Li, C. Wang and X. Lu, *Talanta*, 2018, **181**, 431.

227 N. Song, Y. Zhu, S. Chen, C. Wang and X. Lu, *ACS Sustainable Chem. Eng.*, 2018, **6**, 16766.

228 T. Lin, L. Zhong, L. Guo, F. Fu and G. Chen, *Nanoscale*, 2014, **6**, 11856.

229 W. Zhu, M. Chi, M. Gao, C. Wang and X. Lu, *J. Colloid Interface Sci.*, 2018, **528**, 410.

230 W. Zhu, M. Li, S. Chen, C. Wang and X. Lu, *Appl. Surf. Sci.*, 2019, **491**, 138.

231 W. Song, M. Chi, M. Gao, B. Zhao, C. Wang and X. Lu, *J. Mater. Chem. C*, 2017, **5**, 7465.

232 Z. Yang, C. Wang and X. Lu, *Sci. China Mater.*, 2018, **61**, 653.

233 N. Song, C. Wang and X. Lu, *ACS Sustainable Chem. Eng.*, 2020, **8**, 11069.

234 Z. Yang, F. Ma, Y. Zhu, S. Chen, C. Wang and X. Lu, *Dalton Trans.*, 2017, **46**, 11171.

235 M. Li, Y. Zhu, H. Wang, C. Wang, N. Pinna and X. Lu, *Adv. Energy Mater.*, 2019, **9**, 1803185.

236 M. Li, H. Wang, W. Zhu, W. Li, C. Wang and X. Lu, *Adv. Sci.*, 2020, **7**, 1901833.

237 S. Wan, Y. Liu, G. D. Li, X. Li, D. Wang and X. Zou, *Catal. Sci. Technol.*, 2016, **6**, 4545.

238 S. Kang, J. Jang, S. H. Ahn and C. S. Lee, *Dalton Trans.*, 2019, **48**, 2170.

239 Y. Wen, H. Zhu, L. Zhang, S. Zhang, M. Zhang and M. Du, *Mater. Res. Bull.*, 2019, **112**, 46.

240 S. Yu, J. Kim, K. R. Yoon, J. W. Jung, J. Oh and I. D. Kim, *ACS Appl. Mater. Interfaces*, 2015, **7**, 28116.

241 D. Ji, S. Peng, L. Fan, L. Li, X. Qin and S. Ramakrishna, *J. Mater. Chem. A*, 2017, **5**, 23898.

242 Y. Huang, Y. E. Miao, L. Zhang, W. W. Tjiu, J. Pan and T. Liu, *Nanoscale*, 2014, **6**, 10673.

243 W. Wu, Y. Zhao, S. Li, B. He, H. Liu, X. Zeng, J. Zhang and G. Wang, *J. Colloid Interface Sci.*, 2019, **547**, 291.

244 Y. Rheem, S. H. Park, Y. Han, K.-H. Lee, S.-M. Choi and N. V. Myung, *J. Electrochem. Soc.*, 2020, **167**, 066522.

245 X. Zhu, L. Mo, Y. Wu, F. Lai, X. Han, X. Y. Ling, T. Liu and Y. E. Miao, *Compos. Commun.*, 2018, **9**, 86.

246 M. L. Zou, J. D. Chen, L. F. Xiao, H. Zhu, T. T. Yang, M. Zhang and M. L. Du, *J. Mater. Chem. A*, 2015, **3**, 18090.

247 K. S. Ranjith, C. H. Kwak, S. M. Ghoreishian, Ji S. Im, Y. S. Huh and Y. K. Han, *Nanotechnology*, 2020, **31**, 275402.

248 F.-F. Wang, L. Xu, P. Wang and Y. Zhang, *Electrochim. Acta*, 2019, **306**, 437.

249 L. Gu, H. Zhu, D. N. Yu, S. G. Zhang, J. Chen, J. Wang, M. Wan, M. Zhang and M. L. Du, *Part. Part. Syst. Charact.*, 2017, **34**, 1700185.

250 H. Zhu, J. Zhang, R. Yanzhang, M. Du, Q. Wang, G. Gao, J. Wu, G. Wu, M. Zhang, B. Liu, J. Yao and X. Zhang, *Adv. Mater.*, 2015, **27**, 4752.

251 M. Wan, J. Li, T. Li, H. Zhu, W. Wu and M. Du, *Nanotechnology*, 2018, **29**, 385602.

252 Z. Zhang, Y. Wang, X. Leng, V. H. Crespi, F. Kang and R. Lv, *ACS Appl. Energy Mater.*, 2018, **1**, 1268.

253 L. Zhang, J. Yin, K. Wei, B. Li, T. Jiao, Y. Chen, J. Zhou and Q. Peng, *Nanotechnology*, 2020, **31**, 205604.

254 Y. Rheem, S. H. Park, S. Yu, K.-H. Lee and N. V. Myung, *J. Electrochem. Soc.*, 2020, **167**, 066522.

255 H. Zhu, M. Du, M. Zhang, M. Zou, T. Yang, Y. Fu and J. Yao, *J. Mater. Chem. A*, 2014, **2**, 7680.

256 M. Du, M. Wan, D. Yu, H. Zhu and M. Zhang, *Chin. J. Inorg. Chem.*, 2017, **33**, 595.

257 J. Li, W. W. Wu, M. Wan, L. Gu, J. Wang, T. Li, H. Zhu, M. Zhang and M. L. Du, *Int. J. Electrochem. Sci.*, 2017, **12**, 4563.

258 Y. Zhu, L. Song, N. Song, M. Li, C. Wang and X. Lu, *ACS Sustainable Chem. Eng.*, 2019, **7**, 2899.

259 H. Gu, Y. Huang, L. Zuo, W. Fan and T. Liu, *Inorg. Chem. Front.*, 2016, **3**, 1280.

260 X. Zhang, L. Li, Y. Guo, D. Liu and T. You, *J. Colloid Interface Sci.*, 2016, **472**, 69.

261 S. Zhang, Y. Li, H. Zhu, S. Lu, P. Ma, W. Dong, F. Duan, M. Chen and M. Du, *ACS Appl. Mater. Interfaces*, 2020, **12**, 6250.

262 H. Gu, W. Fan and T. Liu, *Nanoscale Horiz.*, 2017, **2**, 277.

263 A. Yella, H. W. Lee, H. N. Tsao, C. Yi, A. K. Chandiran, M. K. Nazeeruddin, E. W. G. Diau, C. Y. Yeh, S. M. Zakeeruddin and M. Grätzel, *Science*, 2011, **334**, 629.

264 J. Halme, P. Vahermaa, K. Miettunen and P. Lund, *Adv. Mater.*, 2010, **22**, E210.

265 X. Liang, H. W. Zheng, X. J. Li, Y. H. Yu, G. T. Yue, W. Zhang, J. J. Tian and T. F. Li, *Ceram. Int.*, 2016, **42**, 12888.

266 X. Zhang, X. Liu, Y. Zhang, R. Bao, D. Peng, T. Li, G. Gao, W. Guo and C. Pan, *J. Mater. Chem. C*, 2016, **4**, 8130.

267 L. Li, X. Zhang, D. Wang, W. Zhang, X. Li, X. Zhao, Q. Zhang, L. Gu, Z. Yu and M. Wu, *Electrochim. Acta*, 2018, **280**, 94.

268 L. Li, P. Zhu, S. Peng, M. Srinivasan, Q. Yan, A. S. Nair, B. Liu and S. Samakrishna, *J. Phys. Chem. C*, 2014, **118**, 16526.

269 X. Zhao, D. Wang, S. Liu, Z. Li, J. Meng, Y. Ran, Y. Zhang and L. Li, *Mater. Res. Bull.*, 2020, **125**, 110800.

270 J. Qiu, D. He, R. Zhao, B. Sun, H. Ji, N. Zhang, Y. Li, X. Lu and C. Wang, *J. Colloid Interface Sci.*, 2018, **522**, 95.

271 L. Li, J. Xiao, H. Sui, X. Yang, W. Zhang, X. Li, A. Hagfeldt and M. Wu, *J. Power Sources*, 2016, **326**, 6.

272 J. Xiao, X. Zeng, W. Chen, F. Xiao and S. Wang, *Chem. Commun.*, 2013, **49**, 11734.

273 J. Y. Lin and S. W. Chou, *Electrochem. Commun.*, 2013, **37**, 11.

274 A. Banerjee, K. K. Upadhyay, S. Bhatnagar, M. Tathavadekar, U. Bansode, S. Agarkar and S. B. Ogale, *RSC Adv.*, 2014, **4**, 8289.

275 J. Qiu, D. He, H. Wang, W. Li, B. Sun, Y. Ma, X. Lu and C. Wang, *Electrochim. Acta*, 2021, **367**, 137451.

276 P. Sudhagar, J. H. Jung, S. Park, Y. G. Lee, R. Sathyamoorthy, Y. S. Kang and H. Ahn, *Electrochem. Commun.*, 2009, **11**, 2220.

277 Y. Shengyuan, A. S. Nair, R. Jose and S. Ramakrishna, *Energy Environ. Sci.*, 2010, **3**, 2010.

278 Y. Shengyuan, A. S. Nair, Z. Peining and S. Ramakrishna, *Mater. Lett.*, 2012, **76**, 43.

279 M. J. Jin, T. Ma, T. Ling, S. Z. Qiao and X. W. Du, *J. Mater. Chem.*, 2012, **22**, 13057.

280 J. Yang, L. Pan, G. Zhu, X. Liu, H. Sun and Z. Sun, *J. Electroanal. Chem.*, 2012, **677–680**, 101.

281 G. E. Unni, T. G. Deepak and A. Sreekumaran Nair, *Mater. Sci. Semicond. Process.*, 2016, **41**, 370.

282 S. Yang, A. S. Nair and S. Ramakrishna, *Mater. Lett.*, 2014, **116**, 345.

283 Y. Cao, Y. J. Dong, H. Y. Chen, D. Bin Kuang and C. Y. Su, *RSC Adv.*, 2016, **6**, 78202.

284 J. Zhong, X. Zhang, Y. Zheng, M. Zheng, M. Wen, S. Wu, J. Gao, X. Gao, J. Liu and H. Zhao, *ACS Appl. Mater. Interfaces*, 2013, **5**, 8345.

285 J. Liu, J. Liang, C. Wang and J. Ma, *J. Energy Chem.*, 2019, **33**, 160.

286 F. Luo, D. Ma, Y. Li, H. Mi, P. Zhang and S. Luo, *Electrochim. Acta*, 2019, **299**, 173.

287 X. Xie, Y. Hu, G. Fang, X. Cao, B. Yin, Y. Wang, S. Liang, G. Cao and A. Pan, *J. Mater. Chem. A*, 2019, **7**, 16541.

288 C. Zhu, Y. Wen, P. A. Van Aken, J. Maier and Y. Yu, *Adv. Funct. Mater.*, 2015, **25**, 2335.

289 S. Husmann, Ö. Budak, A. Quade, A. Frank, A. Kruth, C. Scheu, A. Tolosa and V. Presser, *J. Power Sources*, 2020, **450**, 227674.

290 L. Zhang, Y. Huang, Y. Zhang, H. Gu and W. Fan, *Adv. Mater. Interfaces*, 2016, **3**, 1500467.

291 A. Wang, S. Xie, R. Zhang, Y. She and C. Chen, *Nanoscale Adv.*, 2019, **1**, 656.

292 X. Yin, W. Sun, L. Lv and Y. Wang, *Chem. Eng. J.*, 2018, **346**, 376.

293 A. K. Haridas, J. Heo, Y. Liu, H. Ahn, X. Zhao, Z. Deng, M. Agostini, A. Matic, K. Cho and J. Ahn, *ACS Appl. Mater. Interfaces*, 2019, **11**, 29924.

294 X. Yu, C. Pei, W. Chen and L. Feng, *Electrochim. Acta*, 2018, **272**, 119.

295 X. Zhang, Y. Deng, Y. W. L. Zhan, S. Yang and Y. Song, *New Res. Carbon Mater.*, 2018, **33**, 554.

296 L. Fei, B. P. Williams, S. H. Yoo, J. M. Carlin and Y. L. Joo, *Chem. Commun.*, 2016, **52**, 1501.

297 R. Hongtong, P. Thanwisai, R. Yensano, J. Nash, S. Srilomsak and N. Meethong, *J. Alloys Compd.*, 2019, **804**, 339.

298 H. Wu, C. Hou, G. Shen, T. Liu, Y. Shao, R. Xiao and H. Wang, *Nano Res.*, 2018, **11**, 5866.

299 Y. Zhu, X. Fan, L. Suo, C. Luo, T. Gao and C. Wang, *ACS Nano*, 2016, **10**, 1529.

300 L. Zhang, W. Fan and T. Liu, *Nanoscale*, 2016, **8**, 16387.

301 S. Zhou, J. Chen and L. Gan, *Sci. Bull.*, 2016, **61**, 227.

302 S. Yu, J. Jung and I. Kim, *Nanoscale*, 2015, **7**, 11945.

303 X. Li, N. Fu, J. Zou, X. Zeng, Y. Chen, L. Zhou, W. Lu and H. Huang, *Electrochim. Acta*, 2017, **225**, 137.

304 C. Chen, G. Li, J. Zhu, Y. Lu, M. Jiang, Y. Hu, Z. Shen and X. Zhang, *Carbon*, 2017, **120**, 380.

305 W. Jiang, Q. Liu, J. Peng, Y. Jiang, Y. Ding and Q. Wei, *Nanotechnology*, 2020, **31**, 235713.

306 Y. Qi, J. Liu, J. Dai, X. Shi, X. Zhu, B. Fu, H. Dong and W. Zhao, *ChemistrySelect*, 2020, **5**, 1792.

307 Y. Miao, Y. Huang, L. Zhang, W. Fan, F. Lai and T. Liu, *Nanoscale*, 2015, **7**, 11093.

308 C. Zhao, J. Kong, X. Yao, X. Tang, Y. Dong, S. L. Phua and X. Lu, *ACS Appl. Mater. Interfaces*, 2014, **6**, 6392.

309 X. Ni, H. Chen, C. Liu, F. Zeng, H. Yu and A. Ju, *J. Alloys Compd.*, 2020, **818**, 152835.

310 C. Zhang, Z. Jiang, B. Lu, J. Liu, F. Cao, H. Li, Z. Yu and S. Yu, *Nano Energy*, 2019, **61**, 104.

311 A. Liu, Y. Guan, Z. Guo, H. Che, L. Wang, H. Li, Z. Feng, Z. Zhang, X. Zhang, G. Wang and J. Mu, *Solid State Ionics*, 2019, **340**, 115021.

312 J. H. Choi, J. Yun, A. S. Bandarenka, J. Kim, P. V. Braun, S. Y. Jeong and C. R. Cho, *ACS Nano*, 2017, **11**, 1026.

313 J. Kong, C. Zhao, Y. Wei and X. Lu, *ACS Appl. Mater. Interfaces*, 2015, **7**, 24279.

314 S. Hu, W. Chen, E. Uchaker, J. Zhou and G. Cao, *Chem. – Eur. J.*, 2015, **21**, 18248.

315 L. Fei, B. P. Williams, S. H. Yoo, J. M. Carlin and Y. L. Joo, *Chem. Commun.*, 2016, **52**, 1501.

316 Q. Qu, F. Qian, S. Yang, T. Gao, W. Liu, J. Shao and H. Zheng, *ACS Appl. Mater. Interfaces*, 2016, **8**, 1398.

317 X. Chen, L. Li, S. Wang, C. Feng and Z. Guo, *Mater. Lett.*, 2016, **164**, 595.

318 H. Chen, J. He, G. Ke, L. Sun, J. Chen, Y. Li, X. Ren, L. Deng and P. Zhang, *Nanoscale*, 2019, **11**, 16253.

319 X. Zheng, Y. Zheng, H. Zhang, Q. Yang and C. Xiong, *Chem. Eng. J.*, 2019, **370**, 547.

320 T. Xing, Y. Ouyang, L. Zheng, X. Wang, H. Liu, M. Chen, R. Yu, X. Wang and C. Wu, *J. Energy Chem.*, 2020, **42**, 108.

321 W. Zhang, Z. Yue, Q. Wang, X. Zeng, C. Fu, Q. Li, X. Li, L. Fang and L. Li, *Chem. Eng. J.*, 2020, **380**, 122548.

322 J. S. Cho, J. S. Park and Y. C. Kang, *Nano Res.*, 2017, **10**, 897.

323 W. Li, R. Bi, G. Liu, Y. Tian and L. Zhang, *ACS Appl. Mater. Interfaces*, 2018, **10**, 26982.

324 T. Du, H. Zhu, B. Bin Xu, C. Liang, M. Yan and Y. Jiang, *ACS Appl. Energy Mater.*, 2019, **2**, 4421.

325 L. Wang, G. Yang, J. Wang, S. Peng and W. Yan, *Small*, 2020, **16**, 1904589.

326 A. Cheng, H. Zhang, W. Zhong, Z. Li, Y. Tang and Z. Li, *J. Electroanal. Chem.*, 2019, **843**, 31.

327 G. Chen, X. Yao, Q. Cao, S. Ding, J. He and S. Wang, *Mater. Lett.*, 2019, **234**, 121.

328 Q. Ni, Y. Bai, S. Guo, H. Ren, G. Chen, Z. Wang, F. Wu and C. Wu, *ACS Appl. Mater. Interfaces*, 2019, **11**, 5183.

329 H. Zhai, H. Jiang, Y. Qian, X. Cai, H. Liu, Y. Qiu, M. Jin, F. Xiu, X. Liu and L. Lai, *Mater. Chem. Phys.*, 2020, **240**, 122139.

330 D. Kong, X. Qiu, B. Wang, Z. Xiao, X. Zhang and R. Guo, *Sci. China Mater.*, 2018, **61**, 671.

331 C. Zhu, X. Mu, P. A. Van Aken, Y. Yu and J. Maier, *Angew. Chem., Int. Ed.*, 2014, **53**, 2152.

332 W. H. Ryu, H. Wilson, S. Sohn, J. Li, X. Tong, E. Shaulsky, J. Schroers, M. Elimelech and A. D. Taylor, *ACS Nano*, 2016, **10**, 3257.

333 Z. Yang, J. Huang, Y. Zhang, B. Ye, S. Lin, J. Liu, Y. Ye, K. Zheng, G. Lu, T. Guo and X. Yu, *Energy Technol.*, 2020, **8**, 1901356.

334 C. Cui, Z. Wei, J. Xu, Y. Zhang, S. Liu and H. Liu, *Energy Storage Mater.*, 2018, **15**, 22.

335 Y. Wang, Y. Zhang, J. Shi, X. Kong and X. Cao, *Energy Storage Mater.*, 2019, **18**, 366.

336 W. Zhang, J. Chen, Y. Liu, S. Liu, X. Li and K. Yang, *J. Alloys Compd.*, 2020, **823**, 153631.

337 W. Yang, H. Lu, Y. Cao and P. Jing, *J. Power Sources*, 2019, **441**, 227173.

338 W. Yang, H. Lu, Y. Cao, B. Xu, Y. Deng and W. Cai, *ACS Sustainable Chem. Eng.*, 2019, **7**, 4861.

339 C. Wu, X. Zeng, P. He, L. Chen and W. Wei, *Adv. Mater. Interfaces*, 2018, **5**, 1701080.

340 X. Xu, X. Li, J. Zhang, K. Qiao, D. Han, S. Wei, W. Xing and Z. Yan, *Electrochim. Acta*, 2019, **302**, 259.

341 S. Zhang, H. Zhao, M. Wang, Z. Li and J. Mi, *Electrochim. Acta*, 2018, **279**, 186.

342 J. Xie, J. Xia, Y. Yuan, L. Liu, Y. Zhang, S. Nie, H. Yan and X. Wang, *J. Power Sources*, 2019, **435**, 226762.

343 X. Li, T. Liu, Y. X. Wang, S. L. Chou, X. Xu, A. Cao and L. Chen, *J. Power Sources*, 2020, **451**, 227790.

344 W. Zhao, S. Ci, X. Hu, J. Chen and Z. Wen, *Nanoscale*, 2019, **11**, 4688.

345 J. Xia, L. Liu, S. Jamil, J. Xie, H. Yan, Y. Yuan, Y. Zhang, S. Nie, J. Pan, X. Wang and G. Cao, *Energy Storage Mater.*, 2019, **17**, 1.

346 Y. Yuan, M. Yang, L. Liu, J. Xia, H. Yan, J. Liu, J. Wen, Y. Zhang and X. Wang, *Nanoscale*, 2020, **12**, 20337.

347 X. Li, T. Liu, Y. Wang, S. Chou, X. Xu, A. Cao and L. Chen, *J. Power Sources*, 2020, **451**, 227790.

348 C. Y. Zhang, Z. W. Lu, Y. H. Wang, Z. Dai, H. Zhao, G. Z. Sun, W. Lan, X. J. Pan, J. Y. Zhou and E. Q. Xie, *Chem. Eng. J.*, 2020, **392**, 123734.

349 X. Wang, X. Zhao, C. H. Ma, Z. Z. Yang, G. Chen, L. Wang, H. J. Yue, D. Zhang and Z. H. Sun, *J. Mater. Chem. A*, 2020, **8**, 1212.

350 M. Yu, Z. Wang, Y. Wang, Y. Dong and J. Qiu, *Adv. Energy Mater.*, 2017, **7**, 1700018.

351 S. Xue, S. Yao, M. Jing, L. Zhu, X. Shen, T. Li and Z. YiLiu, *Electrochim. Acta*, 2019, **299**, 549.

352 B. Guo, W. Du, T. Yang, J. Deng, D. Liu and Y. Qi, *Adv. Sci.*, 2020, **7**, 1902617.

353 Y. Cao, H. Lu, B. Xu, W. Yang and Q. Hong, *Chem. Eng. J.*, 2019, **378**, 122247.

354 Z. Zhang, K. Tan, Y. Gong, H. Wang, R. Wang, L. Zhao and B. He, *J. Power Sources*, 2019, **437**, 226908.

355 Y. Lei, Q. Wang, S. Peng, S. Ramakrishna, D. Zhang and K. Zhou, *Adv. Energy Mater.*, 2020, **10**, 1902115.

356 Z. Pan, H. Chen, J. Yang, Y. Ma, Q. Zhang, Z. Kou, X. Ding, Y. Pang, L. Zhang, Q. Gu, C. Yan and J. Wang, *Adv. Sci.*, 2019, **6**, 1900628.

357 Y. Wang, J. Fu, Y. Zhang, M. Li, F. M. Hassan, G. Li and Z. Chen, *Nanoscale*, 2017, **9**, 15865.

358 X. Shi, B. He, L. Zhao, Y. Gong, R. Wang and H. Wang, *J. Power Sources*, 2021, **482**, 228955.

359 X. Lu, C. Wang, F. Favier and N. Pinna, *Adv. Energy Mater.*, 2017, **7**, 1601301.

360 C. Ma, Y. Li, J. Shi, Y. Song and L. Liu, *Chem. Eng. J.*, 2014, **249**, 216.

361 G. Nie, X. Lu, J. Lei, Z. Jiang and C. Wang, *J. Mater. Chem. A*, 2014, **2**, 15495.

362 G. Nie, X. Lu, M. Chi, Y. Zhu, Z. Yang, N. Song and C. Wang, *Electrochim. Acta*, 2017, **231**, 36.

363 Y. M. Chen, Z. Li, X. Wen and D. Lou, *Angew. Chem., Int. Ed.*, 2015, **54**, 10521.

364 G. Nie, X. Lu, M. Chi, M. Gao and C. Wang, *J. Colloid Interface Sci.*, 2018, **509**, 235.

365 Y. Liu, J. Zhou, W. Fu, P. Zhang, X. Pan and E. Xie, *Carbon*, 2017, **114**, 187.

366 F. Lu, J. Wang, X. Sun and Z. Chang, *Mater. Des.*, 2020, **189**, 108503.

367 X. Qiu, L. Wang and L. Fan, *J. Mater. Chem. A*, 2018, **17**, 7835.

368 J. Xu, L. Zhang, G. Xu, Z. Sun, C. Zhang, X. Ma, C. Qi, L. Zhang and D. Jia, *Appl. Surf. Sci.*, 2018, **434**, 112.

369 F. Tong, X. Wu, W. Jia, J. Guo, Y. Pan, Y. Lv, D. Jia and X. Zhao, *CrystEngComm*, 2020, **22**, 1625.

370 B. Gill, D. Kyu and H. Jeon, *Microelectron. Eng.*, 2020, **222**, 111205.

371 H. Fu, X. Zhang, J. Fu, G. Shen and Y. Ding, *J. Alloys Compd.*, 2020, **829**, 154557.

372 R. Kumuthini, R. Ramachandran, H. A. Therese and F. Wang, *J. Alloys Compd.*, 2017, **705**, 624.

373 Z. Wang, C. Liu, G. Shi, G. Wang, H. Zhang, Q. Zhang, X. Jiang and X. Li, *Ionics*, 2020, **26**, 3051.

374 J. Huang, J. Wei, Y. Xu, Y. Xiao and Y. Chen, *J. Mater. Chem. A*, 2017, **5**, 23349.

375 A. Jagadale, X. Zhou, D. Blaisdell and S. Yang, *Sci. Rep.*, 2018, **8**, 1602.

376 Y. Liu, G. Jiang, S. Sun, B. Xu, J. Zhou, Y. Zhang and J. Yao, *J. Electroanal. Chem.*, 2017, **804**, 212.

377 Y. Huang, Y. Zhao, J. Bao, J. Lian, M. Cheng and H. Li, *J. Alloys Compd.*, 2019, **772**, 337.

378 S. K. Sami, S. Siddiqui, M. T. Feroze and C. H. Chung, *Mater. Res. Express*, 2017, **4**, 116309.

379 W. Du, Y. Bai, J. Xu, H. Zhao, L. Zhang, X. Li and J. Zhang, *J. Power Sources*, 2018, **402**, 281.

380 D. Tian, X. Lu, Y. Zhu, M. Li and C. Wang, *J. Power Sources*, 2019, **413**, 50.

381 D. Tian, N. Song, M. Zhong, X. Lu and C. Wang, *ACS Appl. Mater. Interfaces*, 2020, **12**, 1280.

382 D. Tian, S. Chen, W. Zhu, C. Wang and X. Lu, *Mater. Chem. Front.*, 2019, **3**, 1653.

383 J. Liu, F. Zhang, L. Hou, S. Li, Y. Gao, Z. Xin, Q. Li, S. Xie, N. Wang and Y. Zhao, *Sustainable Mater. Technol.*, 2020, **26**, e00214.

384 Q. Chen, Y. Liu, H. Deng, T. Lyu, J. Tan, W. Yang, H. Li and S. Ramakrishna, *Polym. Eng. Sci.*, 2020, **60**, 2887.

385 C. L. Fausey, I. Zucker, D. E. Lee, E. Shaulsky and J. B. Zimmerman, *ACS Appl. Mater. Interfaces*, 2020, **12**, 18446.

386 H. Sereshti, H. Gaikani and H. Rashidi, *J. Iran. Chem. Soc.*, 2018, **15**, 743.

387 G. Dognani, P. Hadi, H. Ma, F. C. Cabrera, A. E. Job, D. L. S. Agostini and B. S. Hsiao, *Chem. Eng. J.*, 2019, **372**, 341.

388 S. Li, X. Lu, X. Li, Y. Xue, C. Zhang, J. Lei and C. Wang, *J. Colloid Interface Sci.*, 2012, **378**, 30.

389 J. Qiu, F. Liu, S. Cheng, L. Zong, C. Zhu, C. Ling and A. Li, *ACS Sustainable Chem. Eng.*, 2018, **6**, 447.

390 Y. Lu, Y. Fang, X. Xiao, S. Qi and C. Huan, *Colloids Surf., A*, 2018, **553**, 210.

391 T. Krasian, W. Punyodom and P. Worajittiphon, *Chem. Eng. J.*, 2019, **369**, 563.

392 P. Shah, T. N. Narayanan, C. Li and S. Alwarappan, *Nanotechnology*, 2015, **26**, 315102.

393 Q. Tian, F. Jiang, R. Zou, Q. Liu, Z. Chen, M. Zhu, S. Yang, J. Wang, J. Wang and J. Hu, *ACS Nano*, 2011, **5**, 9761.

394 Y. Xiao, J. Peng, Q. Liu, L. Chen, K. Shi, R. Han, Q. Yang, L. Zhong, R. Zha, Y. Qu and Z. Qian, *Theranostics*, 2020, **10**, 1500.

395 B. Dhandayuthapani and A. C. Poulose, *Biofabrication*, 2012, **4**, 025008.

396 S. Wang, J. Qiu, W. Guo, X. Yu, J. Nie, J. Zhang and X. Zhang, *Adv. Biosyst.*, 2017, **1**, 1600042.

397 S. Wu, J. Wang, L. Jin, Y. Li and Z. Wang, *ACS Appl. Nano Mater.*, 2018, **1**, 337.

398 X. Wang, F. Lv, T. Li, Y. Han, Z. Yi, M. Liu, J. Chang and C. Wu, *ACS Nano*, 2017, **11**, 11337.